

博士論文

Study of the red giant variables in the Large and Small Magellanic Clouds

(大小マゼラン星雲の赤色巨星変光星の研究)

高山 正輝

平成 26 年

Abstract

Recent micro-lensing surveys (e.g. MACHO, OGLE, EROS) provide us, as a by-product, with long-baseline light curves of a huge number of red giant variables in the Large and Small Magellanic Clouds (LMC and SMC). One of the most important developments by those surveys over the past decades is the discovery of at least 8 period-luminosity relations (sequences A', A, B, C', C, D, E and F) of the red giant variables in the LMC and SMC. Different sequences imply different origins of the light variations. Mira/semi-regular variables and OGLE small amplitude red giants (OSARGs) are pulsating red giant branch stars (RGB stars) or asymptotic giant branch stars (AGB stars) falling on the sequences A', A, B, C', C and F, while sequence E can be interpreted by the eclipse/ellipsoidal binary origin. In the last ridge, the sequence D is the longest period among the period-luminosity relations. We have no plausible interpretation for the origin of the light variations associated with those periods. The pulsation periods on the sequence D are named the long secondary periods (LSPs). In this thesis, we examine the pulsation modes corresponding to the pulsation of RGB OSARGs in the LMC (Part I) and the variability associated with the periods falling on the sequence D in the SMC (Part II). Part of this thesis is published in [Takayama et al. \(2013\)](#) and [Takayama et al. \(2015\)](#).

In part I, we discuss the properties of pulsation in the RGB stars of OSARGs in the LMC. OSARGs show multi-periodic variations leading to their irregular light curves. Pulsation periods of RGB OSARGs fall on three narrow ridges (b_1 , b_2 and b_3) on the period-luminosity diagram. The pulsation modes interpreting those ridges have been a matter of debate for the past several years. By comparing pulsation periods and the period ratios of theoretical models with observations obtained with OGLE-III, we have found that the radial first, second and third overtone modes and the non-radial dipole ($l = 1$) p_4 and quadrupole ($l = 2$) p_2 modes reproduce those three ridges. The RGB stars of OSARGs are consistent with stars having initial (i.e. ZAMS) masses of $\sim 0.9 - 1.4 M_{\odot}$ and current luminosities of $\log L/L_{\odot} \sim 2.8 - 3.4$. With those stellar parameters, the period corresponding to the scaled optimal frequency ν_{\max} for solar-like oscillations increases with luminosity, and passes through roughly the ridge of b_2 on the period luminosity plane. This indicates that the stochastic excitation causes the pulsation in OSARGs.

In part II, we discuss the properties of LSPs in red giants and explore a possible explanation for the light variations. OGLE V and I data and long-term JHK_s light curves obtained with the SIRIUS camera mounted on the IRSF 1.4m telescope have become available for the more luminous red giant variables in the SMC. By combining them, we have selected 21 program stars including 7 oxygen-rich stars and 14 carbon stars which show prominent LSPs in the light curves. It is found that in the oxygen-rich stars the most broad band colours (e.g. $V - I$) get redder at the light declines in its LSP cycle, while the $J - K_s$ colour of those stars barely changes or even gets bluer when the star dims. The most plausible explanation for the cause of getting bluer in the $J - K_s$ colour would be an increase of H_2O vapour absorption induced by the development of a dense cool layer above the atmosphere. This scenario is consistent with the results of recent observations which suggest that a chromosphere develops during its LSPs cycle, which implies that the LSP

phenomenon is associated with mass ejection from the stellar atmosphere near the beginning of light decline. We have explored the possibility that photometric variations in OGLE V and I and the near-IR JHK_s can be interpreted by either dust absorption by ejected matter or dark spots on a rotating stellar surface. We have found, however, that both models can not reproduce the light and colours variations associated with LPSs. A simple combined dust absorption and dark spots model do not show any better improvement at explaining the observation than the dust and spotted star models individually. We conclude that some other mechanism is the cause of the light variations showing LSP.

Contents

1	INTRODUCTION	9
1.1	Pulsating stars	10
1.1.1	Mira/SRV stars	10
1.1.2	OSARGs	13
1.2	Sequence E stars	16
1.3	Sequence D stars	17
1.3.1	Pulsation models	17
1.3.2	Binary models	18
1.3.3	Dust formation	20
1.3.4	Rotating spot	21
1.3.5	Giant convective cell	22
I	Optical Gravitational Lensing Experiment Small Amplitude Red Giants	23
2	Observational properties of RGB OSARGs	23
3	Models	27
4	Comparison with observations	28
4.1	Mode identifications	28
4.2	Mass ranges	31
5	Discussion	38
5.1	Effects of metallicity and mixing-length	38
5.2	Connection to the solar-like oscillations in G/K giants	42
6	Summary	42

II	Long Secondary Period	47
7	The observational data	47
7.1	The near-IR data	47
7.2	The optical data	48
7.3	The combined near-IR and optical data	48
7.4	Separating the LSP variation from the primary period variation	51
8	Modeling the LSP magnitude and colour variations	51
8.1	The dust model	55
8.2	Comparison of the dust model with observations	56
8.2.1	The variation of I with $I - J$	56
8.2.2	The variation of I with $J - K_s$	59
8.2.3	The variation of I with $V - I$	63
8.2.4	Testing different dust grains	63
8.3	The dark spot model	66
8.4	Comparison of the spot model with observations	70
8.4.1	The variation of I with colours	70
8.4.2	The effect on spot models of the inclination of the rotation axis and the spot latitude	71
8.5	The combined dust model with dark spot	76
9	Summary	77
10	SUMMARY OF THIS THESIS	81
	Reference	85
A	Stellar pulsation	91
A.1	Radial pulsation	91

A.2 Non-radial pulsation	93
A.3 Period ratio	95
B MESA code	96
C Radiative transfer problem in a spherically symmetric dust shell	98
C.1 The equation of radiative transfer	98
C.2 Spherically symmetric dust shell	99
D Light from a spotted star	103

1. INTRODUCTION

Red giants are evolved stars having initial masses in the range of roughly $0.85\text{--}8M_{\odot}$. They are either red giant branch (RGB) stars or asymptotic giant branch (AGB) stars. An RGB star has a H burning shell surrounding the helium core and an outer extended convection envelope. In the stars having initial masses of $\leq 2.3M_{\odot}$, the helium core gets strongly electron degenerate due to high density against the temperature when stars climb up the red giant branch on the HR diagram. Then, the core is supported by the degeneration pressure. Note that the critical mass mentioned above varies with the chemical abundance (e.g., [Wagner 1974](#)). When the temperature near the centre of the helium core increases to $\sim 10^8$ K, the core helium ignition occurs, and the temperature in the helium burning region increases. Since the electron degeneracy pressure hardly depends on the temperature, the helium burning region do not expand immediately, causing little negative feedback. Hence the helium nuclear reaction gets explosive (so called core He flash). The flash occurs at the tip of the red giant branch (TRGB) on the HR diagram. When the temperature increases enough to lift the electron degeneracy, the core expands and hence the temperature decreases. Then, the He flash settles down and steady burning begins. For more massive red giant stars in the H shell burning phase, the temperature in the helium core increases with the gas density and reaches the ignition temperature of the helium burning before the helium core becomes strongly degenerate. Therefore, the massive red giant stars undergo a gentle helium ignition in contrast with the low mass red giant stars.

After the exhaustion of helium in the core, the C/O core contracts and the helium burning occurs in just above the C/O core, while the outer envelope expands. Then, the star enters into the AGB phase, in which energy is generated in the double burning shells consisting of outer H burning shell and inner He burning shell. Some red giants are carbon-rich stars, in which carbon is more abundant than oxygen in the atmosphere. A carbon-rich envelope is formed through thermal pulses in the AGB phase of a star whose initial mass lies between 0.8 and $4 M_{\odot}$ (e.g., [Bergeat et al. 2002](#)), although the mass range is still uncertain.

Many luminous red giant stars are also known as variable stars with periods longer than 1 day. They are classified as long period variables (LPVs). Recently, ground based long-term observations for micro-lensing events such as MACHO, OGLE and EROS have also detected numerous red giant LPVs in the Galactic bulge and the large and small magellanic clouds (LMC and SMC). The periods positively correlate with the stellar luminosities. At least 8 sequences are recognized in the period-luminosity plane, which are labeled A', A, B, C', C, D, E and F (e.g., [Wood et al. 1999](#); [Ita et al. 2004](#); [Soszyński et al. 2004](#); [Derekas et al. 2006](#); [Fraser et al. 2008](#); [Graczyk et al. 2011](#); [Soszyński & Wood 2013](#); [Soszyński, Wood & Udalski 2013](#)). Figure 1 shows the period luminosity relations for the LPVs in the LMC. It is generally thought that different period-luminosity relations correspond to different origins of the light variations (e.g., [Wood et al. 1999](#); [Soszyński, Wood & Udalski 2013](#)). Mira/semi-regular variables and Optical Gravitational Lensing Experiment (OGLE) Small Amplitude Red Giants (OSARGs) are pulsating RGB and AGB stars. They form the sequences A', A, B, C', C and F. On the other hand, the sequence E consists of the eclipse/ellipsoidal binaries

(Wood et al. 1999). The longest-period ridge, the sequence D, corresponds to the long secondary periods (LSPs) in red giants. We have no plausible explanation for the origin of the light variations associated with LSPs (e.g., Wood et al. 2004). The recent theoretical and observational studies on the red giants on those 8 sequences are reviewed in the next three sub sections below.

1.1. Pulsating stars

Stellar pulsation causes the light variations corresponding to the sequence A', A, B, C', C and F on the period luminosity plane (e.g., Soszyński, Wood & Udalski 2013). Wood et al. (1999) argued that the sequence C consists of Mira like stars, while all the other shorter period sequences belong to SRVs because of its irregular and small amplitude light curves. Ita et al. (2004) found the sequence C' corresponding to the overtone of the sequence C' Soszyński et al. (2004) found from OGLE data that the pulsating red giants in the LMC and SMC can be separated into two distinct groups, RGB & AGB pulsators. Below the luminosity of the red giant tip, RGB and AGB pulsators form closely separated sequences.

1.1.1. Mira/SRV stars

In general, the light curves of Mira type stars have large amplitudes in visible bands. The top two panels of each of the two columns of Figure 2 show light curves in *I* band for samples of Miras and SRVs obtained from the OGLE-III database for the LPVs in the LMC (Soszyński et al. 2009). The light curves are folded with the periods of the largest amplitude and shown through the phase of 0–2. The light curve shapes of some sequence C stars are regular or sometime sinusoidal, but others show irregular variabilities. Those irregularities indicate oscillations to be multi-periodic. From the OGLE-III observation, Soszyński et al. (2004) found that the sequence C stars in both the LMC and SMC have no periods belong to the sequence A. Instead, the periods corresponding to the second (or even the third) largest amplitude fall on the sequence B or C (or hopefully C'). They classified red giant variables having the periods falling on the sequence C into either Mira or SRV type. Although the distinctions in the stellar parameters between Mira and SRV are uncertain, Mira stars are sometimes separated from SRV stars according to whether the amplitude is larger than either 2.5 [mag] in the *V* band or 0.8 [mag] in the *I* band (e.g., Soszyński et al. 2009).

The cause of those multiple periods can be interpreted as different pulsation modes. In fact, from a comparison of theoretical model with observation, Ita et al. (2004) proposed that the sequence C correspond to the radial fundamental mode of AGB stars while the sequence C' is the first overtone mode. Note that though Soszyński, Wood & Udalski (2013) proposed that the sequence B corresponds to the radial second overtone, the discussion of the mode determination for the sequence B still continues (e.g., Mosser et al. 2013, who suggested that the 1st overtone corresponds to the sequence B). The pulsation amplitudes of Mira/SRV stars in the LMC tend to increase with

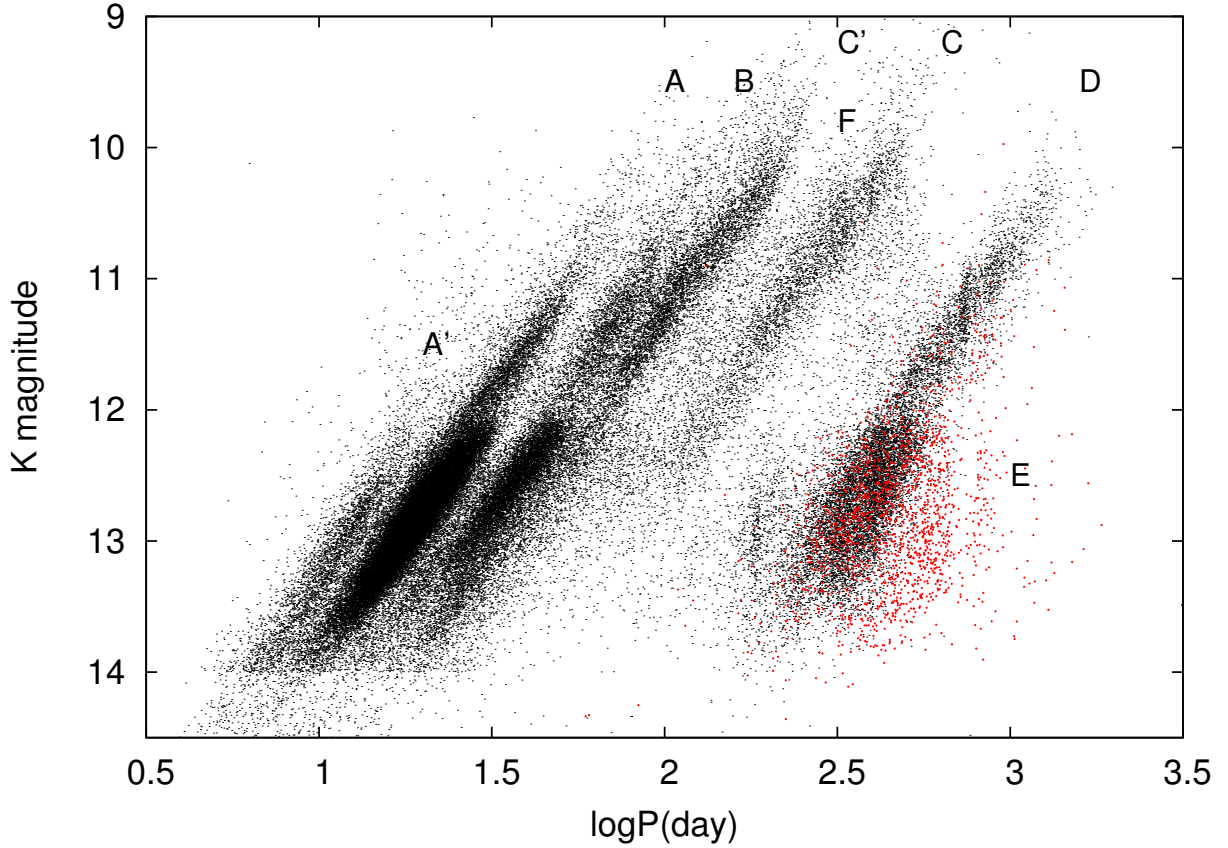


Fig. 1.— Period - K magnitude diagram for $\sim 90,000$ LPVs in the LMC listed at the OGLE-III catalog of variable stars (Soszyński et al. 2009). All the data plotted on this figure have been adopted from both OGLE-III and 2MASS observations. The periods are obtained from Soszyński’s catalog, while the K magnitudes are obtained from 2MASS database. Note that the red points correspond to the sequence E stars, for which the double of the period defined by Soszyński et al. (2009) (i.e. the orbital period) is plotted.

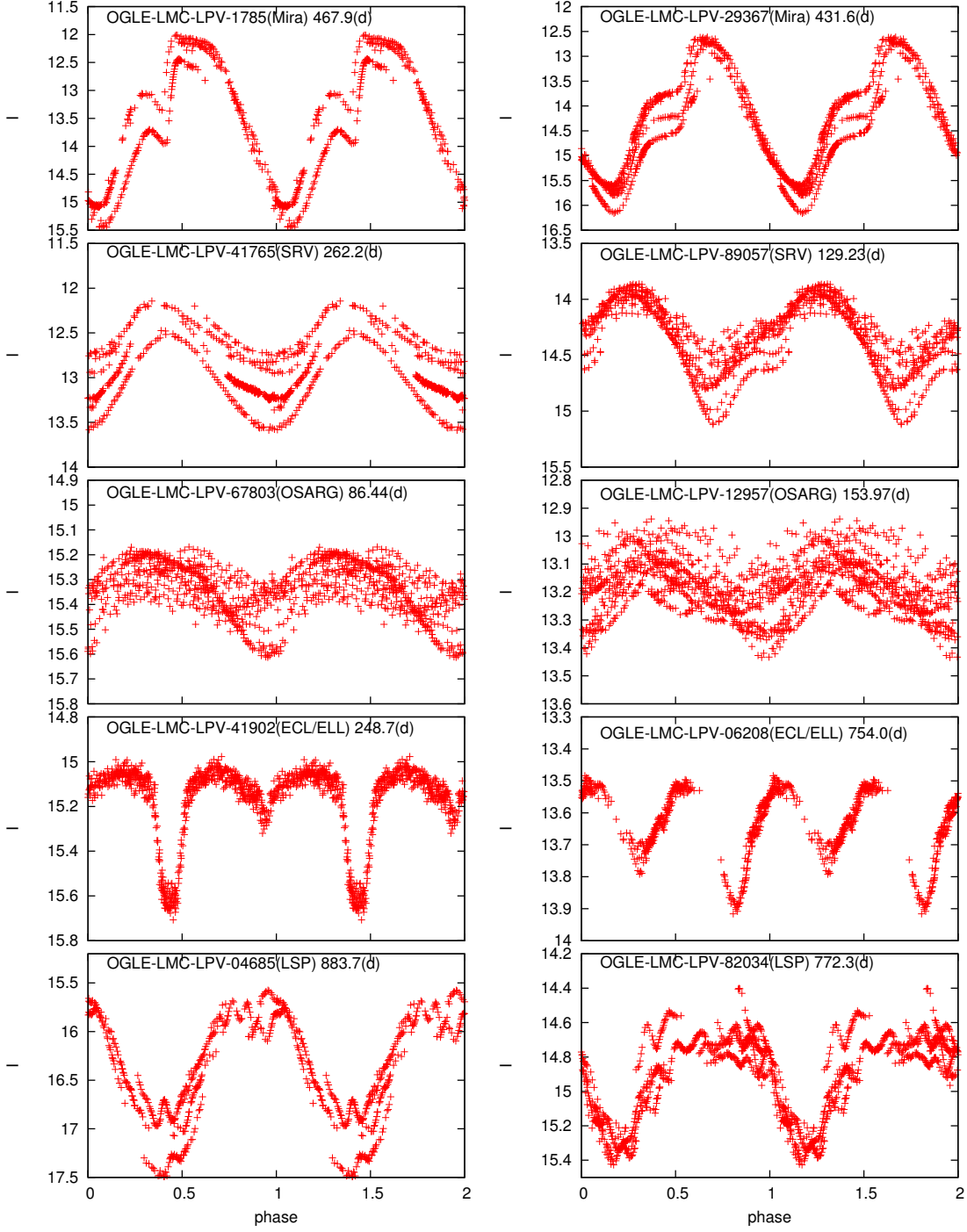


Fig. 2.— The observed *I* band light curves for various LPVs in the OGLE-III observation listed in the catalog of [Soszyński et al. \(2009\)](#). All the light curves are folded with the first periods, corresponding to the largest amplitude, indicated in the right top of each panel. Top three panels of each column are for Miras, SRVs, and OSARGs, respectively, while bottom two panels are for sequences E and D stars labeled ‘ECL/ELL’ and ‘LSP’, respectively. Note that the light curves for the two sequence E stars are folded with the orbital period.

pulsation periods, thus Miras tend to lie near the long-period edge of the sequence C while SRVs lie both the sequence C' and C (Soszyński, Wood & Udalski 2013).

The sequence F stars lie between the sequence C' and C (or partly fall on the sequence C) on the period-luminosity plane in the LMC (Soszyński & Wood 2013). Note that since the periods of the sequence F stars are similar to those of the sequences C' and C stars, the ridge corresponding to the sequence F is not clear in Figure 1. From the OGLE-III database Soszyński & Wood (2013) found that the oxygen-rich stars lying around the sequence C on the PL diagram could be separated into two distinct groups on the $W_{JK} - \log(\Delta I)$ plane, where W_{JK} is the reddening free Wesenheit index given by $W_{JK} = K_s - 0.686(J - K_s)$, while ΔI is the I band amplitude. Since the stars in the large amplitude group generally show clear periodicity and lie on the sequence C, these stars can be classified as either Mira or SRa class. On the other hand the small amplitude group consists of the sequence F stars. They generally exhibit irregular variabilities compared to the SRa stars. Therefore they should belong to the SRb class. On the $W_{JK} - \log(\Delta I)$ plane, some luminous sequence F stars lie around the main region of the sequence C stars; i.e. they have much larger amplitudes among the sequence F stars. Soszyński & Wood (2013) suggested that the luminous sequence F stars are possibly the progenitors of carbon stars on the sequence C.

The periods of the second largest amplitude of sequence F stars generally fall on the sequence B. From the theoretical modeling, the pulsations in the sequence F stars can be well explained by the radial fundamental mode. Thus there seems to be almost no difference in the pulsation properties between the two sequences C and F stars except for the classifications of Mira/SRa and SRb. On the other hand, about 33% of the sequence F stars show long secondary periods (LSPs) in the second or third largest amplitude period. In contrast, only 8% of the sequence C stars show LSP. The most of the LSPs of the sequence F stars fall on a broad ridge lying between the sequences C and D on the period luminosity plane. We do not know the origin of the light variations of the LSPs nor of the LSPs on the sequence D. Note that the fraction of the sequence F stars with LSPs is comparable with the fraction of the luminous SRV stars with LSPs whose primary period generally are on the sequences A and B (cf. Section 1.3 for more detail). We do not yet understand the relationship between the two LSPs.

1.1.2. OSARGs

The three short period sequences (A', A, and B) in the LMC and SMC are occupied by the OSARG variables (e.g., Soszyński et al. 2004; Soszyński, Wood & Udalski 2013). Those stars are the same as the stars Wray et al. (2004) found in the Galactic bulge using the OGLE-II variable star catalog. Sample light curves for two stars of OSARGs are shown in the third panels in the two columns of Figure 2. The most OSARG variables exhibit small amplitudes and irregular variabilities. From the result of the observation for the OSARGs in the Galactic bulge, Soszyński et al. (2013) found that the amplitudes of the pulsation in OSARG variables are much smaller than those of the Mira stars, and that the largest amplitude (~ 0.1 mag in the I band) for the OSARG

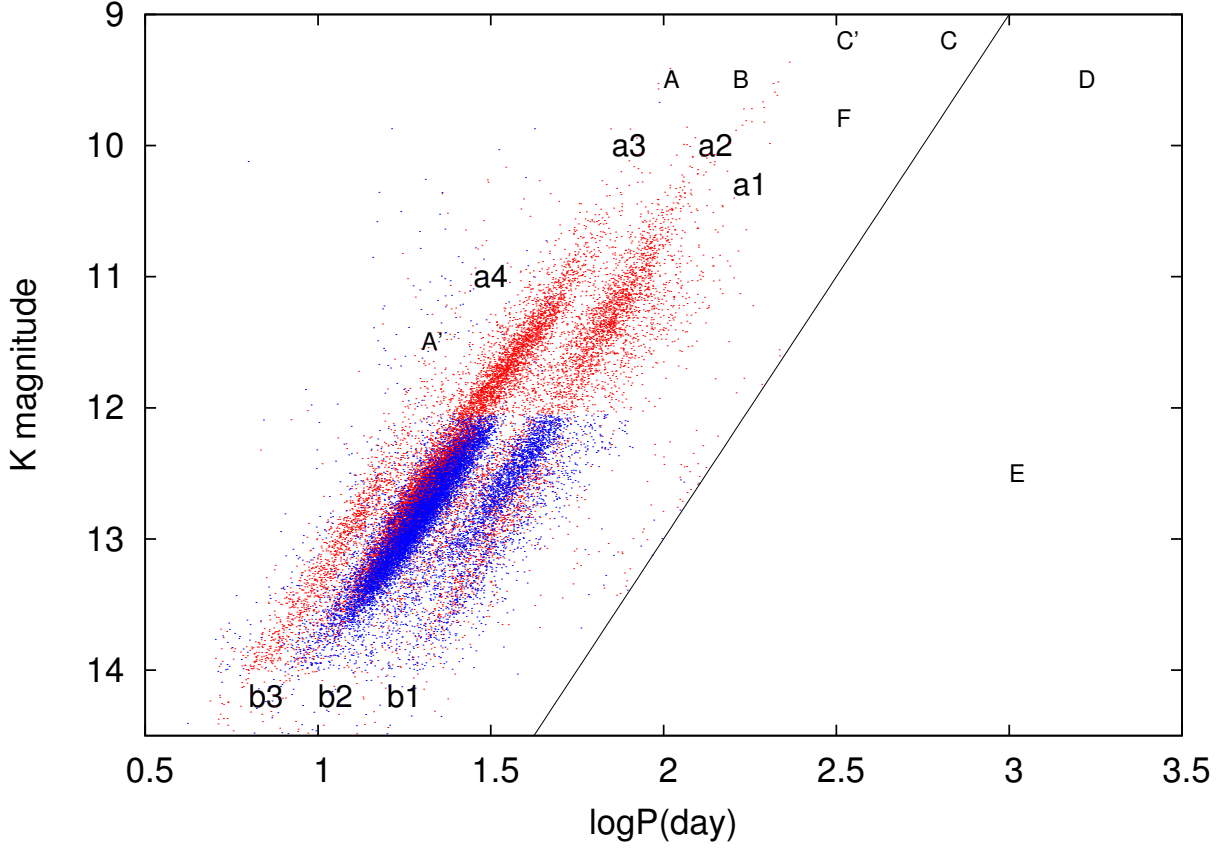


Fig. 3.— The same as Figure 1 but plotted with only OSARGs in the LMC. The labels A’-F show the positions of the period luminosity relations shown in Figure 1. The more luminous OSARGs within Soszyński’s catalog (Soszyński et al. 2009) than the luminosities corresponding to the solid black line ($K = -2.0 \log P + 21.0$) are selected as the program stars. The red points show the AGB stars of OSARG variables while the blue points are for the RGB stars of OSARGs. The locus of the tip of the red giant branch (TRGB) corresponds to the K_s of 12.05 [mag] (Soszyński et al. 2009).

variables is roughly comparable with the smallest amplitude for the SRV stars. The semi-periodic property indicates that OSARGs pulsate in multiple modes. Combining the OGLE-II and -III data in the LMC and SMC, [Soszyński et al. \(2004\)](#) found that the sequences A and B consist of 6 narrower ridges labeled ‘ a_1 – a_3 ’ and ‘ b_1 – b_3 ’. Moreover, they found an additional faint sequence, ‘ a_4 ’, which corresponds to the sequence A’ labeled by [Derekas et al. \(2006\)](#) for the sequence shorter than the sequence A. The sequences a_1 – a_4 are for AGB stars, while the sequences b_1 – b_3 are for RGB stars of OSARGs. Figure 3 shows the 7 narrow ridges of RGB and AGB stars of OSARGs on the period K magnitude plane. Note that the period of the sequences ‘ a ’ is slightly shorter than ‘ b ’ for a given luminosity. Pulsation periods are approximately given by $P \sim 1/\sqrt{GM/R^3}$, where M and R are the stellar mass and the stellar radius, respectively, while G is the gravitational constant. The period shift between the sequences ‘ a ’ and ‘ b ’ is, therefore, interpreted as that AGB stars are slightly smaller in size than RGB stars at a given luminosity ([Kiss & Bedding 2003](#); [Soszyński et al. 2004](#)).

As the red giants of OSARGs show irregular light curves with multiple periods corresponding to 4 (in the AGB stars) or 3 (in the RGB stars) PL relations, the period ratios are also useful for understanding the properties of pulsation (and hence the stellar parameters) in these stars. [Soszyński et al. \(2004\)](#) found period ratios specific to the OSARG variables in the LMC and SMC. The period ratio corresponding to a_2/a_1 (and b_2/b_1) is approximately equal to 0.69, while a_3/a_1 (b_3/b_1) and a_4/a_1 are ~ 0.50 and ~ 0.39 , respectively, (and hence a_3/a_2 (b_3/b_2) is about 0.73). Similar values of the period ratios have also been derived from the OSARGs in the Galactic bulge ([Wray et al. 2004](#)). These period ratios form approximately horizontal sequences on the period–period ratio plane (i.e. Petersen diagram). Since the values of a_2/a_1 (b_2/b_1), a_3/a_1 (b_3/b_1), and a_3/a_2 (b_3/b_2) are similar, those period ratios form a broad continuous sequences in the Petersen diagram.

Although the period ratios, $P_{\text{short}}/P_{\text{long}}$, of adjacent sequences on the PL plane are less than about 0.8, [Soszyński et al. \(2004\)](#) found two sequences with period ratios around 0.9 and 0.95 on the Petersen diagram. The period ratios close to 1 can be interpreted as that both periods belong to the same ridge on the period luminosity plane. This indicates the existence of more microstructures within the ridge. In fact, [Soszyński et al. \(2004\)](#) and [Soszyński et al. \(2007\)](#) found the evidence for two additional sequences within the ridges of both a_2 (b_2) and a_3 (b_3). Although we can recognize the possibility of the existence of the microstructures, they are hardly visible on the period luminosity plane. [Soszyński et al. \(2004\)](#) and [Soszyński et al. \(2007\)](#) argued that these splits in the PL ridges may indicate the presence of non-radial oscillations.

As mentioned in Section 1.1.1, the periods corresponding to the radial fundamental and the 1st overtone modes in the red giants are in good agreement with the periods along the sequence C and C’, respectively. Many authors have suggested that higher radial overtone modes would correspond to the pulsations in the short period sequences (A’, A, and B) (e.g., [Wood et al. 1999](#); [Ita et al. 2004](#); [Soszyński, Wood & Udalski 2013](#)). In fact, according to the theoretical models for AGB stars calculated by [Wood & Sebo \(1996\)](#), the periods of the radial 2nd and 3rd overtone

modes are roughly in agreement with the sequence B on the period– K magnitude plane (Ita et al. 2004). From theoretical models, Xiong & Deng (2007) found that the longest two ridges ($a_1(b_1)$ and $a_2(b_2)$) correspond to the radial 1st overtone mode and 2nd overtone mode, respectively. In addition, they found that $a_3(b_3)$ seemed to consist of the mixture of the 3rd and 4th overtone modes, and that periods on the sequence a_4 agree with those of the 5th overtone mode. Dziembowski & Soszyński (2010) suggested other mode identities for OSARG variables. They used isochrones and concluded that the sequences b_2 and b_3 correspond to the radial 1st overtone and 2nd overtone modes, respectively. Their mode determinations are also consistent with the result of observations by *Kepler* (Mosser et al. 2013). In spite of this consistency, the intervals between the 1st overtone and 2nd overtone modes in frequency did not reproduce the interval between the sequences b_2 and b_3 . In the first part of this thesis, we will determine the pulsation modes in RGB stars of OSARGs.

1.2. Sequence E stars

In an eclipsing binary with a red giant star, the light minima occur when a companion star is either behind the red giant star or its opposite side (i.e. in front of the red giant star). Thus alternating deep and shallow minima and sometime even flat parts between two adjoining minima can be seen in the light curve. In addition, rotation of a tidally distorted red giant star in a close binary system, which might be tidally synchronized with the orbital period, causes ellipsoidal variability; the light variation is caused by the change of the apparent size of the ellipsoidal star. The light curve shapes are similar to sinusoidal waves. For the eclipsing and ellipsoidal variables, the orbital periods should be equal to the time intervals between two deep (or shallow) minima in the light curves. In the case of circular orbits, especially, the time intervals of alternating deep and shallow minima should be equal to half the length of the orbital period.

The stars on the sequence E are red giant variables showing clear periodic variability with alternating deep and shallow minima. Moreover the light curves of some sequence E stars show approximately sinusoidal shapes. The sequence E lies between the sequences C and D on the period luminosity plane, where the periods derived as the time interval between two adjoining minima in the light curves (e.g., Wood et al. 1999; Soszyński et al. 2004b; Derekas et al. 2006; Nicholls, Wood & Cioni 2010; Nicholls & Wood 2012). The light curves of two stars on the sequence E are shown in the fourth panel of each column of Figure 2. The light curves for the two stars are folded with the intervals equal to double of the periods derived from the light variations (i.e. equal to the orbital periods). The broad ridge formed by the sequence E stars on the period luminosity plane is commonly interpreted as being due to the variety of the orbital periods (hence the separations and the mass ratios between the red giant and the companion). Soszyński et al. (2004b) and Derekas et al. (2006) examined the properties of the sequence E stars with the OGLE and MACHO database, respectively. Adopting orbital periods, which means to shift the position of the sequence E in period by a factor of 2, they found that the sequence E is connected continuously to the sequence D.

1.3. Sequence D stars

The last sequence, the sequence D, is the longest period sequence in period luminosity relations for luminous red giant variables. The periods on the sequence D extend from about 400 d to 1500 d, which are 3~4 times longer than the periods of the sequence C for the same luminosity. The sequence D stars also show light variations associated with shorter pulsation periods which correspond to the sequence B or some to the sequence A (e.g., [Wood et al. 1999](#); [Soszyński et al. 2004](#)). The shorter pulsation period is called the primary period, while the longer period corresponding to the sequence D is known as a long secondary period (LSP). Note that long ‘secondary’ period does not always mean the LSP to have the second largest amplitude in the light curves. The bottom two panels in [Figure 2](#) show examples of the light curves showing distinct LSP and short primary period.

Red giant variables with LSPs have been found within the LMC, SMC and our Galaxy. In fact, LSP modulation has been found in approximately 25–50% of LPVs observed in OGLE and MACHO observations (e.g., [Wood et al. 1999](#); [Fraser et al. 2008](#); [Nicholls et al. 2009](#)). Many researchers have studied the variations associated with LSPs from not only observational but also theoretical aspects. However we have still not found a possible explanation for the origin of LSPs phenomenon. We discuss some proposed hypotheses.

1.3.1. Pulsation models

Radial pulsations, which have been found in many red giant variables like Miras, can easily come to one’s mind as the origin of LSP phenomenon. However, radial pulsation of red giants can not be the cause of the variability of the LSPs. One of the reasons is that the radial fundamental mode in a luminous red giant star, which corresponds to the longest period in radial pulsation, corresponds to the longer period sequence of Mira stars; i.e. the sequence C. Pulsation period P is approximately given by

$$P \propto \frac{1}{\sqrt{\frac{M}{R^3}}}, \quad (1.1)$$

where M and R are the stellar mass and the radius, respectively. LSPs on the sequence D are approximately 4 times longer than the periods corresponding to the sequence C at the same luminosity. If the pulsation in the fundamental mode of red giants were the cause of the light variations associated with LSPs, those red giant stars should have radius approximately 2.5 times larger than a normal SRV star at given luminosity. However the LSP stars observed in MACHO observation have stellar radii of 100–200 R_{\odot} . The median value is $\sim 135R_{\odot}$ ([Nicholls et al. 2009](#)), which is much smaller than the radius of a longer period Mira type variable ($\gtrsim 300R_{\odot}$, e.g., [Mondal et al. 2005](#))).

In addition, radial velocities of LSP stars seem to contradict the assumption of radial pulsation for the LSP phenomenon. The typical value of the full velocity amplitudes of LSPs is approximately

3.5km/s for the LSPs stars in the LMC (Nicholls et al. 2009). Assuming radial pulsation (i.e. the radial velocity variations change stellar radius), Nicholls et al. (2009) found that a typical amplitude in radius derived from integrating radial velocities is $40.02R_{\odot}$ for the LSP stars in the LMC. The median value of the radii is $\sim 135.4R_{\odot}$, which is estimated from the effective temperatures derived from the photometric colour. These results lead to $\sim 30\%$ of radius change during its LSP cycle. Stellar radius play an important role for the determinations of the pulsation periods for a star. If stellar radius changes in such a large fraction during its LSP cycle, the shorter pulsation period (i.e. the primary period) of the star should modulate (e.g., Section 1.1). However, no definite modulations in the primary periods have been found (Wood et al. 2004). The result contradicts the assumption of radial pulsation for the LSP.

Hinkle et al. (2002) found no evidence of rapid expansion of a LSP star caused by shock waves, which are observed in some large amplitude Mira type stars. Although a rapid expansion and slow contraction is expected for a large amplitude pulsation, the velocity curves of their program stars show rapid contraction and slow expansion instead. Thus we can conclude that normal-mode radial pulsation is not the cause of the radial velocity variation associated with LSPs.

The non-radial g^+ mode pulsation is a potential explanation for LSPs. With theoretical models for red giant stars, Wood et al. (2004) found that g_2 – g_3 modes, radial order of 2–3, with degree $l=2$ –3 can represent periods in the range of observed LSPs. However the g^+ mode pulsation should be evanescent in the deep convective zone. The radiative layer on the thick convective envelope in red giant stars, which could drive amplitudes of g^+ modes, is too thin. Only very small amplitude variations due to g^+ mode are expected (Wood et al. 2004; Nicholls et al. 2009). These results for radial and non-radial pulsations suggest that pulsations would not cause LSPs.

1.3.2. Binary models

Variability related with binary system has been thought one of the most possible explanations for the length of LSPs because the LSPs are much longer than the period of the radial fundamental mode for AGB stars. Recent studies have shown a similarity between the sequences D and E on the period luminosity plane. In the red giant variables of MACHO data for the LMC, Derekas et al. (2006) found that the sequence D overlaps with the sequence E near $K \sim 13$ [mag] if the sequence E stars are plotted with the orbital periods, i.e. twice the length of the periods derived from the interval between alternating light minima. Similar results have been found by Soszyński et al. (2004b) and Soszyński (2007) who investigated with OGLE database. However Derekas et al. (2006) and Soszyński (2007) independently found that these are significantly different properties between the sequences D and E stars; the former consists of the LSP stars and the latter is a member of close binary system. MACHO observation for the red giant variables with LSPs and without LSPs indicates that the amplitude ratios between MACHO red and blue bands of the LSP stars tend to be similar to those of the pulsating red giants rather than those of the sequence E stars, which shows approximately equal amplitudes for the two bands (Derekas et al. 2006). On

the other hand, [Soszyński \(2007\)](#) found that only 5% of known LSP stars show eclipse or ellipsoidal variability similar to the sequence E stars. He also found modulations in phase and magnitude at minima in the light curves. This suggests that the variability of LSPs show a lack of periodic regularity, which is one of the most important property in the eclipse/ellipsoidal variability.

The measurement of the radial velocities in the LSP stars also suggest difference between the LSP stars and the sequence E stars. From the observations with the VLT for stars in the LMC, [Nicholls, Wood & Cioni \(2010\)](#) found that almost all the sequence E stars have full radial velocity amplitudes of 15–55 km/s, and the mean value is 43.3 km/s. The LSP stars, however, have full velocity amplitude of approximately 3.5 km/s ([Nicholls et al. 2009](#)). Note that the Galactic LSP stars have similar velocity amplitudes ([Hinkle et al. 2002](#)). In order for binary modes to be viable, orbital velocity ~ 3.5 km/s is required for the LSP period range; 400–1500 d. Assuming a circular orbit of an orbital period of P for a binary system with a red giant star and a less massive companion star, the orbital velocity v of the red giant is given from the Kepler’s law by

$$v = \left(\frac{2\pi G m^3}{P(M + m)^2} \right)^{\frac{1}{3}}, \quad (1.2)$$

where M and m are the masses of the red giant and the companion star, respectively, while G is the gravitational constant. This equation indicates that for a given orbital period, smaller velocity corresponds to smaller companion mass, m . If the LSP stars are binaries and the red giants have masses similar to the sequence E stars, $M \sim 1.25M_{\odot}$ ([Nicholls, Wood & Cioni 2010](#)), the companion mass should be as small as ~ 0.07 – $0.12M_{\odot}$ to obtain periods of 400–1500 d from the typical velocity amplitude 3.5 km/s of the LSPs. The result is consistent with the result of [Nicholls et al. \(2009\)](#), who obtained the companion mass of $0.09M_{\odot}$. By more detailed computations, [Hinkle et al. \(2002\)](#) obtained the companion mass of approximately $0.1M_{\odot}$ under the assumption of the masses of $\sim 1M_{\odot}$ for the red giants. [Hinkle et al. \(2002\)](#) also found that the eccentricities are of ~ 0.2 – 0.5 . [Nicholls et al. \(2009\)](#) derived a median value of 0.3 for the eccentricities for their sample of LSP stars. If binary systems consist of a near solar mass red giant and $\sim 0.1M_{\odot}$ companion star (i.e. brown dwarf or low mass red dwarf), they should have separations of ~ 1 – 2 AU ([Wood et al. 2004](#); [Nicholls et al. 2009](#)). However, much less number of brown dwarf companions to solar mass stars with separation less than 5 AU have been found in a number of the stellar/stellar binary systems. It is so called ‘Brown dwarf desert’ (e.g., [Jumper & Fisher 2013](#)). Therefore, it is unlikely that these binary systems with parameters mentioned above can reproduce the fraction of the red giants with LSPs to the pulsating red giants (25–50%). The same conclusion was derived from an argument about the evolution of close binary systems by [Wood et al. \(2004\)](#). They suggested that a low-mass companion (e.g. brown dwarf) to a solar-mass red giant in close binary with a highly eccentric orbit would merge into the central star within approximately 1000 yr due to orbital angular momentum loss. Since the lifetime of SRV stars is $\sim 2 \times 10^5$ yr, only a small fraction of 0.5% is expected to have LSP among SRV stars.

In the binary models, the asymmetry in the observed velocity curves indicates the orbits to be highly eccentric. The periastron angle determines whether the phase at the maximum velocity

lies in the first or second halves in the velocity curves folded with the orbital period. For a sample of local LSP stars, [Hinkle et al. \(2002\)](#) found that the periastron angles of five of the six program stars fall in the range of 240° – 319° . The periastron angles lying between 180° and 360° indicate that the radial velocities increase rapidly and decrease slowly, agreeing the velocity curves of two out of the three LSP stars studied by [Wood et al. \(2004\)](#). However, The lack of randomness in the periastron angles indicates that the eccentric binary models are unlikely for the cause of the radial velocity variations observed in the LSP stars.

If an AGB star is in a semi-detached binary system filling its Roche lobe, the matter from the AGB star could accrete on the companion star. [Wood et al. \(1999\)](#) found that the light curves associated with LSPs generally show fast decline and slow rise. They proposed a possibility that the eclipse of the red giant star by the comet like companion star, which has accreted dusty clouds and a dusty tail, could explain such asymmetry in the light curves. [Soszyński & Udalski \(2014\)](#) have developed this model. They assumed binary systems consisting of a synchronously rotating ellipsoidal red giant and a comet like companion on a circular orbit. Their simple model produce an asymmetry similar to that found in the light and velocity curves in the LSP stars. Soszyński & Udalski’s model could represent not only the shape of the light curves but also the variety of the amplitudes observed in the LSP stars by assuming different inclinations of the binary model. However, their model could not explain the observed phase shift between the light and velocity curves. The theoretical model suggests that the velocity minimum are behind the light minimum by ~ 0.1 in phase. The observed light and velocity of LSP stars generally show opposite phase shifts. The result implies that the companion and the dense dust cloud should be located separately on the orbit. Therefore, comet like companion model does not seem consistent with the property of LSPs.

1.3.3. Dust formation

Another possible explanation for the light variations with LSP is a periodic dust formation in circumstellar space around a red giant, which [Wood et al. \(1999\)](#) first proposed. This hypothesis based on theoretical models for AGB stars by [Winters et al. \(1994\)](#) and [Höfner et al. \(1995\)](#). It is already known that R Coronae Borealis (RCrB) and RV Tauri stars occasionally eject dust clouds. RCrB stars eject clumpy dust clouds to random directions in irregular intervals, which dim the star by up to 8 [mag], although the mechanism for puffing a matter is still unknown (e.g., [Clayton 1996](#); [Clayton et al. 2013](#)). RV Tauri stars are post AGB stars. Among the RV Tauri stars, RVb type stars are in binaries and show LSP variabilities. The LSPs in RV Tauri stars are approximately equal to the orbital period (e.g., [Van Winckel et al. 1999, 2009](#)). The generally accepted explanation for the origin of the LSPs in RV Tauri stars is the orbital motion of a circumstellar dust disk (or somewhat dust arc) along the orbit of the companion. The circumstellar dust is considered to be ejected from the primary when it is in the AGB phase. Both RCrB stars and RV Tauri stars have an infrared colour excess due to emission from the circumstellar dust around the central star.

The near-infrared observation of 2MASS and the recent mid-infrared observation with Spitzer Space Telescope suggest that the red giant stars with LSPs tend to have a mid-infrared excess (Wood & Nicholls 2009), indicating the presence of circumstellar dust. On near- to mid-infrared color-color and color-magnitude diagrams, some red-giant LSP stars are located close to the region where RV Tauri and RCrB stars occupy, separated from the similar red giants without LSPs. These results imply that the LSP stars undergo an ejection of matter from cycle to cycle. Thus, the variation associated with LSPs might be due to the periodic dust formation in the expanding mass shells, which may be patchy on the analogy of RT Tauri and RCrB stars. The result of the observation for the polarization in red giant variables with LSPs also supports the existence of circumstellar cloud dust clouds (Wood et al. 2004).

1.3.4. Rotating spot

Other possible explanation for the LSP phenomenon is a rotating red giant star with dark spots. Some authors proposed the existence of star spots on AGB stars due to the presence of strong magnetic fields (e.g., Soker & Clayton 1999). Wood et al. (2004) found variations in the strength of H α absorption line with its LSP cycles. This indicates the existence of chromosphere possibly generated by the magnetic activities related to a magnetic dynamo in a rotating red giant star. However, they found that if a critically rotating main sequence $1M_{\odot}$ star evolves to an AGB star with a radius of $170R_{\odot}$, the rotation period should be approximately 3340 days, which is much longer than the maximum LSP around 1500 days.

The evidence of stellar rotation can appear in the line broadening in the spectrum. Using Fourier power of the spectral energy distribution (SED) around the frequency of absorption line, Olivier & Wood (2003) estimated rotation velocities of several LSP variables. They found that the potential maximum limit for the equatorial rotation velocities in the red giant stars with LSPs is 3km/s. The result leads to the rotation period of 2868 days for a red giant star with the radius of $170R_{\odot}$. Note that the equatorial rotation velocity corresponding to a rotation period of ~ 1500 days for the same stellar radius mentioned above is ~ 5.7 km/s. They concluded that rotating spot models for the LSPs are inconsistent with the rotation velocities.

One would expect variations in magnitudes and colours due to the presence of dark spots in a rotating stellar surface. For a given spot size, difference in temperatures between the normal area and the dark area in the stellar surface determines the magnitudes of the light decline. On the other hand, since the energy flux from the dark area decreases with decreasing spot temperature, a larger temperature difference decreases the contribution of the energy flux from the dark area to the total flux. This induces a smaller change in colours through its rotation cycle. The magnitude and colour variations associated with LSPs were shown by Wood et al. (2004) with the MACHO observation. Assuming a stellar surface emitting a blackbody spectrum, however, Wood and his colleague found that a dark spot could not reproduce both the amplitude and colour variations of the LSPs. This conclusion will be re-examined in the second part of this thesis by using a model

atmospheres, and considering limb darkening.

1.3.5. *Giant convective cell*

Giant convective cell model proposed by [Stothers \(2010\)](#) is a new scenario for the explanation of the LSP phenomenon. According to standard mixing length theory, one assumes that the turbulent eddies move upward or downward in a convective zone to carry thermal energy outward in stellar interior. Assuming large convective cells being comparable to stellar radius in size, [Stothers \(2010\)](#) found that the theoretical overturning times of such convective cells in M type red giant stars were roughly consistent with a typical timescale of the LSPs (~ 700 d). According to his giant convective cell model, a giant convective cell travels a distance equal to double the stellar radius ($2R$) during its a cycle of LSP (P). Thus the $2R/P$ should be comparable to the mean velocity of the convective motion of the cell in stellar interior. He obtained $2R/P = 2.3\text{km/s}$ for a typical sequence D star. This computed value is consistent with observed radial velocity amplitudes for the sequence D stars (e.g., [Hinkle et al. 2002](#); [Nicholls et al. 2009](#)). From this result, he suggested that giant convective cell turnover under the stellar surface would be a possible explanation for the cause of the observed radial velocity changes during its LSP cycle.

The magnitude and color variations due to the appearance of a giant convective cell in the stellar surface should be similar to the case of the rotating dark spots because it should lead to only change of the temperature of the surface area where such cells appear. In the second part of this thesis, we will explore the possibility of the giant convective cell model by examining variations in magnitude and colours for a rotating red giant star with a dark spot as large as a hemisphere of a star.

In part I, we discuss the properties of pulsation in the RGB stars of OSARGs in the LMC. Part of this work has been published in [Takayama et al. \(2013\)](#).

In part II, we discuss the new properties of the LSPs derived from the recent long-term observations in the optical and near-IR bands. we consider two theoretical models, the dust absorption in the ejected matter from the stellar surface and dark spots on a rotating stellar surface. We examine whether either of the models can explain the broadband light variations from the optical to near-IR region of LSPs in red giants. Part of this work has been published in [Takayama et al. \(2015\)](#).

Part I

Optical Gravitational Lensing Experiment Small Amplitude Red Giants

We discuss the properties of pulsations in the Optical Gravitational Lensing Experiment Small Amplitude Red Giants (OSARGs) in the Large Magellanic Cloud (LMC). We consider stars below the red giant tip in this paper. They are multiperiodic and form three sequences in the period–luminosity plane. Comparing the periods and period ratios with our theoretical models, we have found that these sequences correspond to radial first to third overtones, and non-radial dipole p_4 and quadrupole p_2 modes. The red giant branch stars of OSARGs consist of stars have initial masses of $\sim 0.9 - 1.4 M_\odot$ which corresponds to a luminosity range of $\log L/L_\odot \simeq 2.8 - 3.4$. With these parameters, the scaled optimal frequency ν_{\max} for solar-like oscillations goes through roughly the middle of the three sequences in the period–luminosity plane, suggesting that the stochastic excitation is likely the cause of the pulsations in OSARGs.

2. Observational properties of RGB OSARGs

We use periods of RGB OSARGs in the LMC given in the OGLE-III catalog (Soszyński et al. 2009), in which up to three periods are listed for each star. In the PL plane, OSARGs are known to form several sequences. We adopt the nomenclature of the sequences and the way of selecting RGB OSARGs introduced by Soszyński et al. (2004); the sequences of RGB OSARGs are named b_1 , b_2 , and b_3 .

Figure 4 shows a Petersen (period vs period-ratio) diagram for all the RGB OSARGs (about 45 500) in the OGLE-III catalogue. In this diagram (and in similar ones shown below), the ordinate indicates the ratio of the shorter to the longer period of a period pair, P_S/P_L , and the abscissa indicates the logarithmic value of the longer period, $\log P_L$. Because each star has three periods, each star appears three times in this diagram. In this figure we see a big dense group in the lower-right corner. The group is formed by the stars associated with the long-period sequence D; i.e. stars having LSPs. The origin of their long periodicity is not clear yet, but majority of them seem to be irrelevant (or unrelated) to stellar pulsation (e.g. Nicholls et al. 2009; Soszyński 2007; Wood et al. 2004).

In this paper, we do not discuss LSPs. To exclude the stars having LSPs from the sample, we have drawn a horizontal line at $P_S/P_L = 0.4$, and a vertical line at $\log P_L = 2.1$ in Figure 4, and we have selected stars located only in the upper-left quadrant in this figure. After excluding stars with LSPs, we have a set of about 8 500 RGB OSARGs in the LMC.

The selected stars are plotted in the PL plane in Figure 5, where the ordinate adopts the

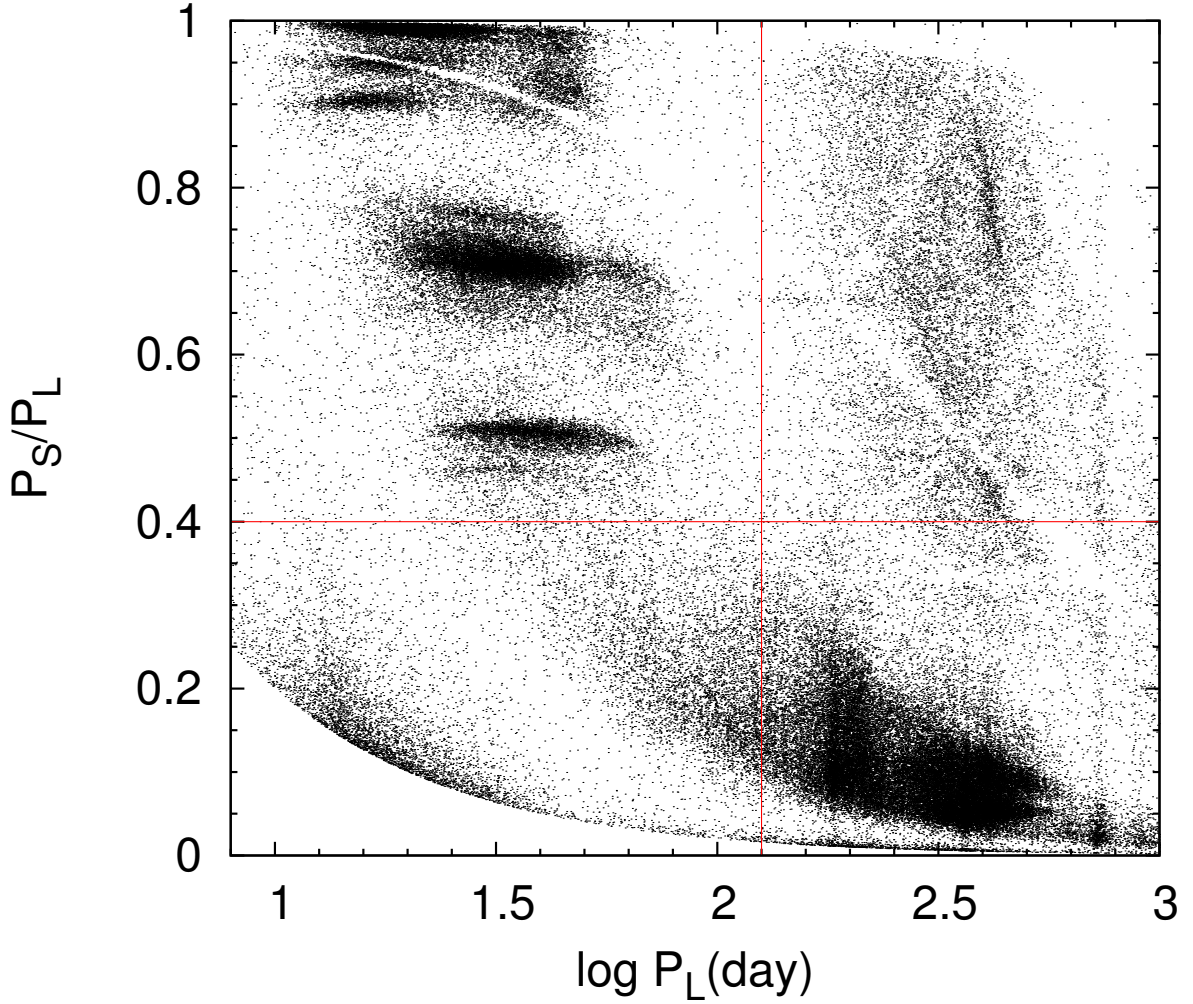


Fig. 4.— All the periods of RGB OSARGs in the catalogue of OGLE-III OSARGs by [Soszyński et al. \(2009\)](#) are plotted in the period vs period-ratio plane (Petersen diagram). The ordinate indicates the ratio of the shorter (P_S) to the longer period (P_L) for each period pair, and the abscissa the logarithmic value of the longer period. Vertical and horizontal lines are used to exclude stars having periods belong to the sequence D (or LSPs).

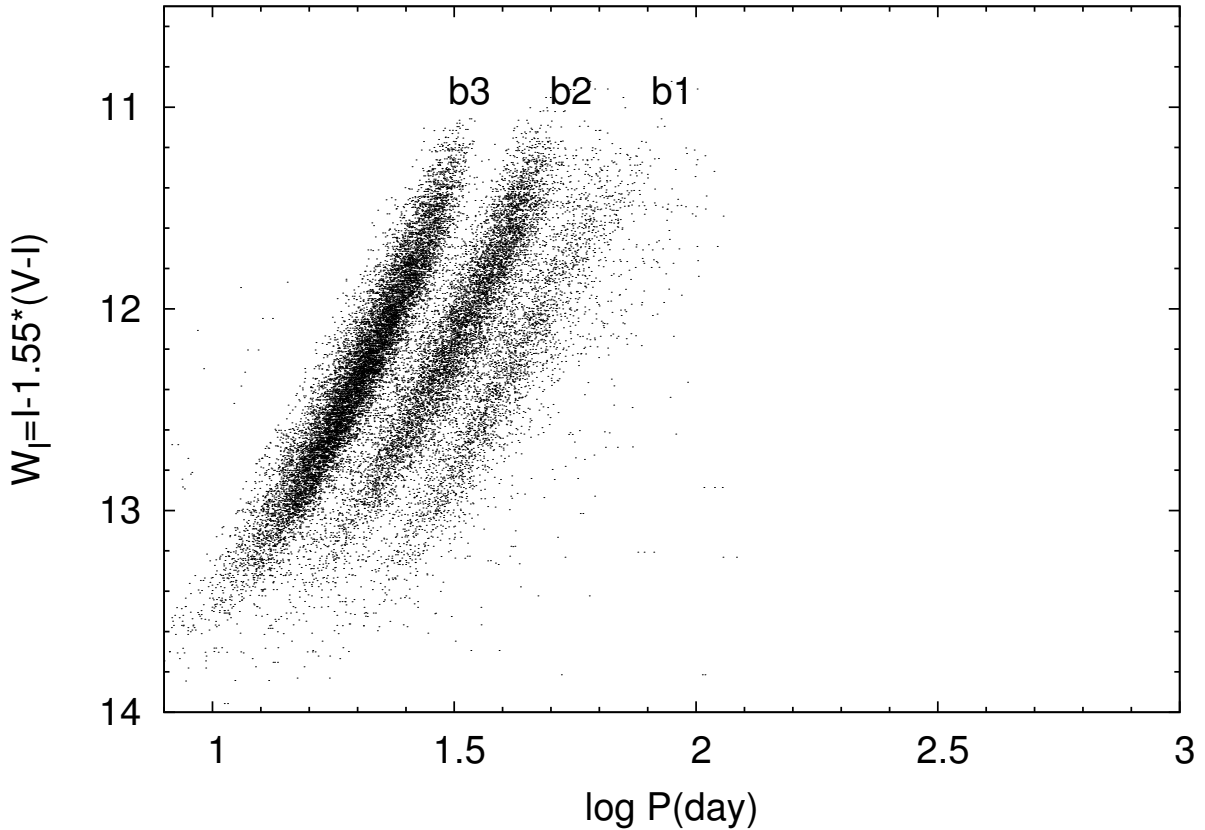


Fig. 5.— Period- W_I diagram for our selected sample of RGB OSARGs (stars having LSPs are removed), where W_I is the reddening-free Wesenheit index defined by equation (2.3). Three ridges are named b_1 , b_2 , and b_3 (from longer to shorter periods) following the nomenclature introduced by Soszyński et al. (2004).

reddening-free Wesenheit index

$$W_I = I - 1.55(V - I) \quad (2.3)$$

with I and V mean magnitudes. In this PL diagram we see three obvious sequences (or ridges). They are b_1 , b_2 , and b_3 sequences from longer to shorter periods, adopting the nomenclature defined by Soszyński et al. (2004). We note that the sequence D is clearly removed from our sample. For the LMC, $W_I \approx 11$ mag corresponds to the giant tip at $\log L/L_\odot \approx 3.4$, while $W_I \approx 14$ mag corresponds to $\log L/L_\odot \approx 2.8$.

Figure 6 shows the Petersen diagram for our selected stars. This figure is the same as the top-left quadrant of Figure 4. We note that despite a significant reduction in the number of stars by excluding LSPs, the property of the distribution in the Petersen diagram is unchanged. The structure of the distribution is more clearly seen in Figure 6. We see two major ridges in Figure 6 at $P_S/P_L \approx 0.5$ and ≈ 0.7 ; the former corresponds to the period ratios between b_3 and b_1 , and the

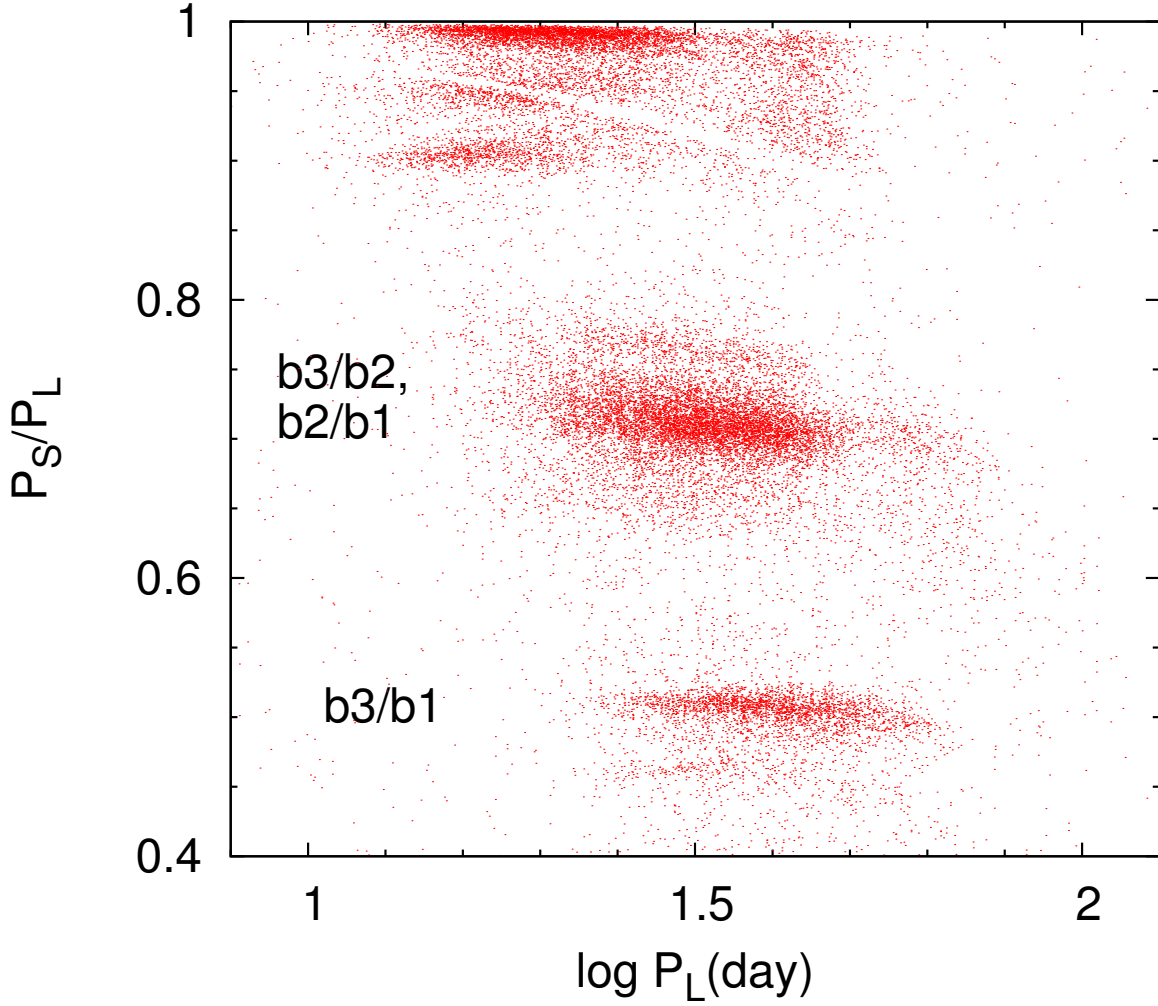


Fig. 6.— Period/Period-ratio (Petersen) diagram for our sample of RGB OSARGs (red dots), from which LSPs (sequence D) are removed. This diagram corresponds to the top-left quadrant of Figure 4. Period-ratios of about 0.5 are produced by the ratios of b_3/b_1 , while ratios of about 0.7 can be attributed to b_2/b_1 and b_3/b_2 . The ridges above ~ 0.9 indicates the presence of non-radial pulsations.

latter is formed by the ratios b_2/b_1 and b_3/b_2 . The additional ridges at $P_S/P_L \approx 0.90$ and ≈ 0.95 are attributed to the presence of sub-ridges in the PL plane along b_2 and b_3 as discussed by [Soszyński et al. \(2007\)](#). The less densely populated ridges in Figure 6 at $P_S/P_L \approx 0.45$ and ≈ 0.75 might be associated with the sub-ridges of b_2 and b_3 . These sub-ridges strongly suggest the presence of non-radial pulsations in OSARGs.

We note that the Petersen diagram (Figure 6) has an advantage over the PL diagram such as Figure 5 in comparing theoretical results with observation to determine pulsation modes. Obviously the PL diagram is affected by errors in luminosities and stellar radii, while only the accuracy in periods for each star matters in the Petersen diagram. Therefore, we use Petersen diagrams to determine pulsation modes for the PL sequences, b_1 – b_3 .

3. Models

In order to identify pulsation modes for each of the corresponding OSARG(RGB) PL relations, we have calculated linear non-adiabatic radial and non-radial pulsation periods for envelope models along evolutionary tracks. The evolutionary models were calculated by using the MESA stellar evolution code ([Paxton et al. 2011](#), see Appendix B for the brief introduction) for initial masses of 0.9, 1.0, 1.1, 1.2, 1.3, 1.4 and $1.6M_\odot$, in which wind mass-loss is included by adopting Reimers’ formula ([Reimers 1975](#))

$$\dot{M} = -4 \times 10^{-13} \eta \frac{(L/L_\odot)(R/R_\odot)}{(M/M_\odot)} M_\odot \text{ yr}^{-1} \quad (3.4)$$

with $\eta = 0.4$. For our canonical models, we have adopted a chemical composition of $(X, Z) = (0.71, 0.01)$ and a mixing-length of 1.5 pressure scaleheight. (We discuss the effects of changing these parameters later in this paper.) Opacity tables of OPAL ([Iglesias & Rogers 1996](#)) with low-temperature extension by [Alexander & Ferguson \(1994\)](#) were used.

Envelope models for radial and non-radial pulsation analyses were calculated at selected evolutionary stages of each evolutionary track. We set the surface boundary at $\tau=0.001$ for the envelope calculations with τ being the optical depth associated with the Rosseland-mean opacity. [Fox & Wood \(1982\)](#) discussed the uncertainties in the pulsation properties caused by various assumptions around the outer boundary of AGB models. To check the influence of the particular place of the outer boundary, we have calculated models imposing the outer boundary condition at $\tau=0.01$. We have found that the difference in periods is less than a few percent, and that the period ratios are hardly different. For radial pulsations we set the bottom of an envelope arbitrarily at $r/R \sim 1/100$. For non-radial pulsations we set the inner boundary just below the convective envelope, suppressing possible coupling with high-order core g modes. This is justified because only p modes completely trapped in the convective envelope can be excited to observable amplitudes (e.g., [Dupret et al. 2009](#)).

Linear non-adiabatic analyses for radial and non-radial pulsations were performed using the

codes described in [Saio, Winget, & Robinson \(1983\)](#) and [Saio & Cox \(1980\)](#), respectively (see Appendix A for the brief introductions). In both cases convection-pulsation coupling is disregarded by neglecting the perturbation of the divergence of the convective flux. Convective turnover time in the convective envelope of a typical model for RGB OSARGs varies from much longer (deep interior) to shorter (in the outer layers) than low-order pulsation periods. This indicates that we should not trust the stability results of our analyses. For this reason we used only periods from these codes disregarding the stability results. We compared our periods and period ratios with fig. 3 of [Xiong & Deng \(2007\)](#), in which the effect of convection-pulsation interaction is included, and found our results to be consistent with their values. This confirms that the convection-pulsation coupling hardly affects periods, and justifies the use of our theoretical periods. This is understandable because the non-adiabaticity is not very strong in the RGB models and the non-adiabatic periods are very close to the adiabatic ones. Finally, the fact that the convective turnover time is comparable to the pulsation periods in some layers in the envelope is favorable for the pulsations to be stochastically excited by turbulent convection.

4. Comparison with observations

4.1. Mode identifications

The period of a pulsation mode is approximately proportional to $1/\sqrt{\bar{\rho}}$ with $\bar{\rho}$ being the mean density (e.g., [Cox 1980](#)), which depends on the stellar mass and radius. Generally, the dependence of the periods ratios on these two parameters is rather weak. In addition, Figure 6 indicates the period ratios depend only weakly on period. For that reason, the period ratios are useful for determining pulsation modes, while pulsation periods are used to determine the appropriate luminosity (or mass) ranges.

First, we determine which radial modes are excited in the RGB OSARGs. Figures 7 and 8 compare observed period ratios with theoretical ones formed by the radial fundamental (F), 1st (1O), 2nd (2O), and 3rd (3O) overtone periods along a part of the evolutionary track ($2.7 \leq \log L/L_{\odot} \leq 3.35$) of an initial mass of $1.1M_{\odot}$. The luminosity range roughly corresponds to that of RGB OSARGs. Figure 7 shows the ratios involving fundamental mode (denoted as ‘F’). Obviously none of the period ratios involving the fundamental mode agrees with any major ridges around 0.5 or 0.7. This indicates that the fundamental mode is not responsible for any of the PL sequences, b_1 , b_2 , and b_3 . For this reason, we do not consider the radial fundamental mode any further.

Figure 8 shows that the ratio of the third overtone to the first overtone (3O/1O) is close to 0.5 in the middle of the luminosity range agreeing with the b_3/b_1 ratio. In addition, the period ratios of 2O/1O and 3O/2O are around 0.7 in the middle of the luminosity range, although they do not go through the central part of the ridge. From these comparisons, we conclude that the radial first, second, and third overtones correspond to, respectively, the b_1 , b_2 , and b_3 sequences of the RGB OSARGs. We note that [Dziembowski & Soszyński \(2010\)](#) was unable to explain the PL

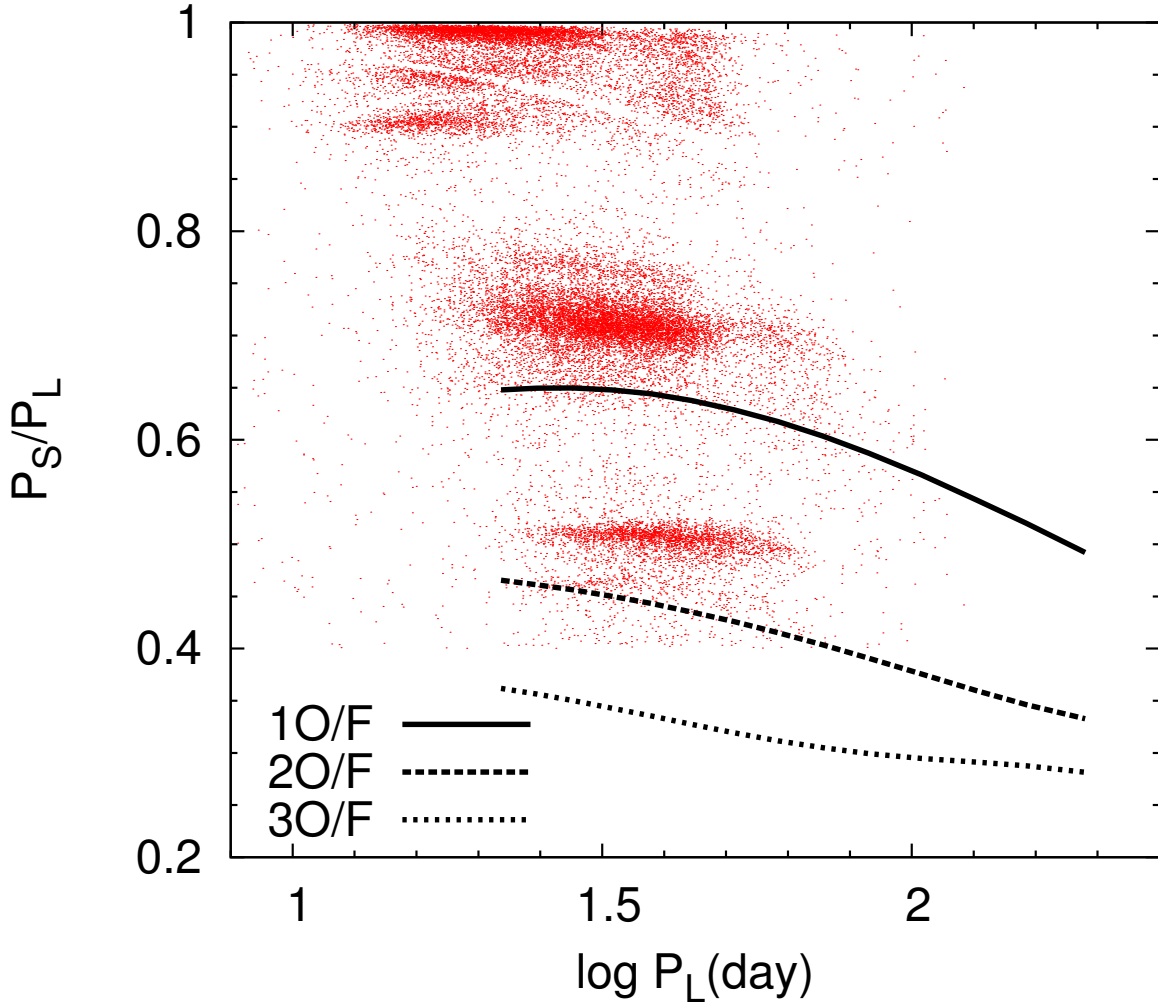


Fig. 7.— Period ratios of the first (1O), second (2O) and third overtone (3O) modes to the radial fundamental mode (F) for our $1.1M_\odot$ models are compared to the observed ratios of OSARGs in the LMC (red dots). The solid line shows the first overtone to fundamental period ratio (1O/F), while the dashed line is for the 2O/F ratio and the dotted line is for the 3O/F ratio. These lines do not fit with any of the ridges in the distribution of OSARG period ratio, indicating that fundamental mode are not excited in the RGB OSARGs.

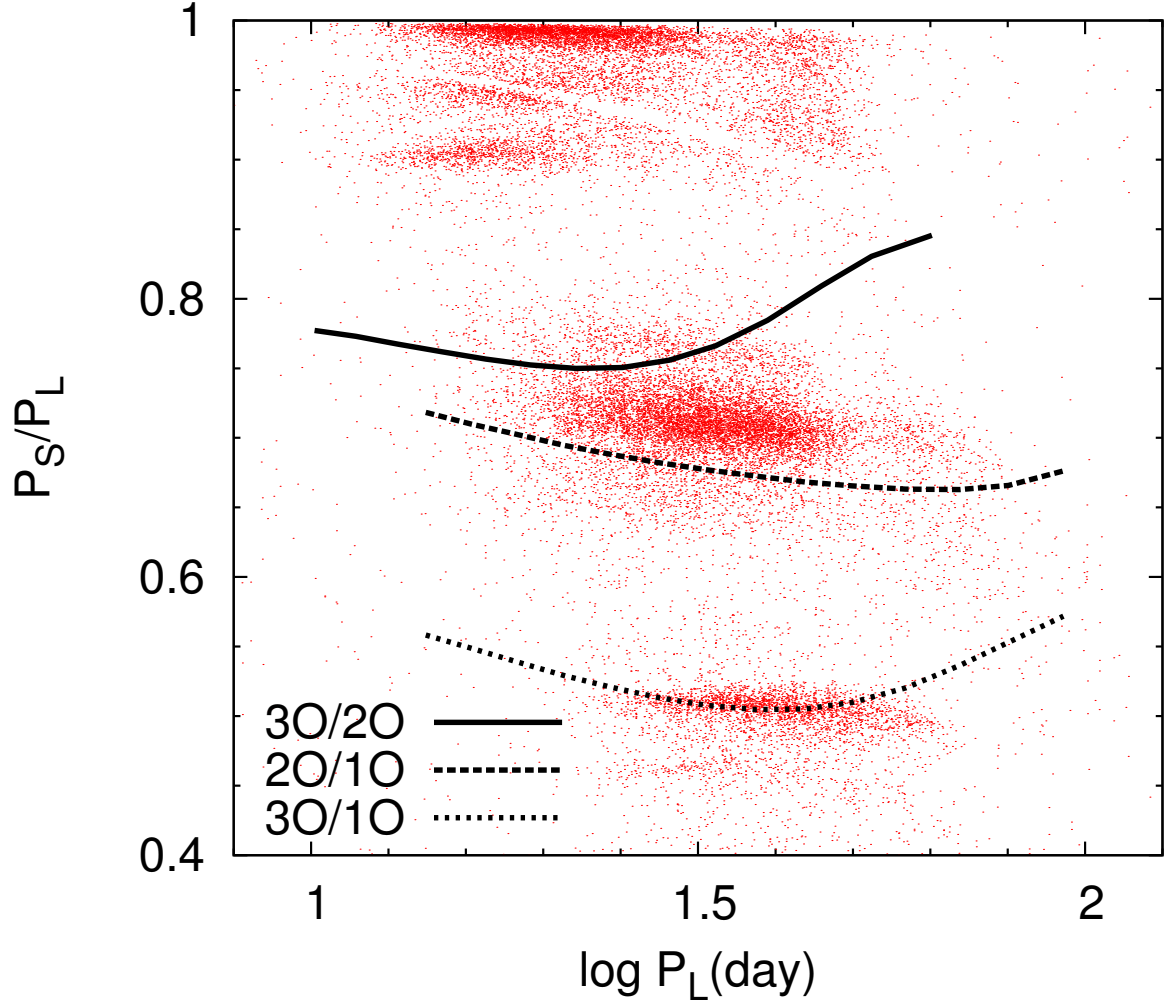


Fig. 8.— The same as 7 but for period ratios without fundamental mode. The solid, dashed and dotted lines show the ratios between radial overtones as indicated. The 3O/2O and 2O/1O ratios go through close to the ridge around 0.7, while the 3O/1O ratio goes through the ridge at 0.5.

sequences b_2 and b_3 by assigning the first overtone (1O) to b_2 and the second overtone (2O) to b_3 . Our identifications differ by one order; i.e., 2O to b_2 and 3O to b_3 .

Figure 8 indicates that the theoretical relations of $1.1M_\odot$ models cannot explain the period ratios for the whole period range of the RGB OSARGs. They agree with the observed ratios only in a period range of $1.5 \lesssim \log P(1O) \lesssim 1.7$ which corresponds to a luminosity range of $3.0 \lesssim \log L/L_\odot \lesssim 3.15$. This means that we have to apply models having different initial masses for different luminosity (hence period) ranges. In other words, the running of the PL relations must be explained by not the stellar evolution of a single mass star, but the evolution of stars with a range of initial masses. We will discuss different mass models in the next subsection.

Here, we consider period ratios involving non-radial pulsations in our $1.1M_\odot$ models in the luminosity range $3.0 \lesssim \log L/L_\odot \lesssim 3.15$. Figures 9 and 10 show period ratios between dipole ($l = 1$) and radial modes, and quadrupole ($l = 2$) and radial modes, respectively, where solid lines, lines with triangles, lines with filled circles correspond to the ratios with 1O, 2O, 3O, respectively. Non-radial modes considered are p_1, \dots, p_4 for both $l = 1$ and 2.

Figure 9 indicates that among the dipole modes, only p_4 is consistent with all the observed ridges in the Petersen diagram. This mode explains the $P_S/P_L \approx 0.45$ sub-ridge by paring with 1O (b_1), the ≈ 0.7 major ridge by paring with 2O (b_2), and $\approx 0.9 - 0.95$ by paring with 3O (b_3). Therefore, we can identity the dipole ($l = 1$) p_4 mode as a sub-ridge of b_3 .

Figure 10 indicates that for the quadrupole ($l = 2$) modes, p_2 mode yields period ratios consistent with the observed ones; ratios with 1O and 3O correspond to the central ridge at ≈ 0.7 and the ratio with 2O corresponds to the ridge at ≈ 0.95 . This means that quadrupole p_2 mode corresponds to a sub-ridge of b_2 . This figure might also indicate the possible presence of $p_1(l = 2)$ as a sub-ridge of b_1 . More data are needed to confirm its presence.

In summary, we have identified 1O for b_1 , 2O and $p_2(l = 2)$ for b_2 , and 3O and $p_4(l = 1)$ for b_3 . Soszyński et al. (2007) argued that each of the sequences b_2 and b_3 has two sub-ridges in addition to a main ridge, while our mode identifications explain only one sub- and main ridge pair. Second sub-ridges, if real, might correspond to higher degree ($l \geq 3$) modes. Also, the ratios with the second sub-ridge within each of sequences b_2 and b_3 might be consistent with the period ratios around 0.98 (e.g., Figure 10) which we cannot explain with our mode identifications. It is interesting that the main part of the ridge at $P_S/P_L \approx 0.7$ is reproduced by the ratios involving non-radial pulsations. This might indicate that main relations of b_2 and b_3 sequences are formed by non-radial pulsations; $p_2(l = 2)$ and $p_4(l = 1)$, respectively, rather than radial modes.

4.2. Mass ranges

In the previous subsection we found that radial 1O, 2O, and 3O, and non-radial $p_4(l = 1)$ and $p_2(l = 2)$ modes are consistent with the observed period ratios in the RGB OSARGs, but

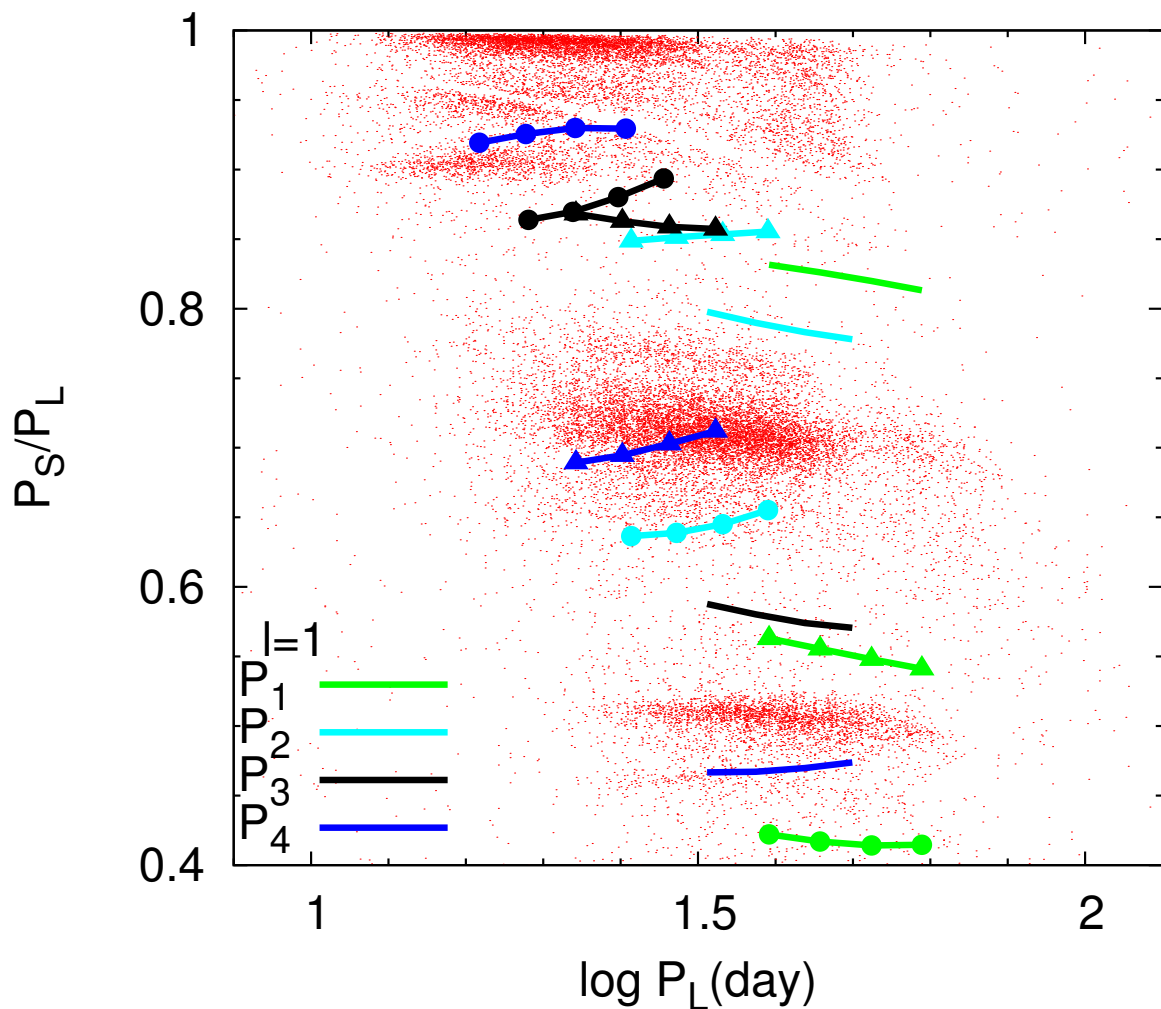


Fig. 9.— The same as 7 but for period ratios of non-radial dipole ($l = 1$) p modes, p_1 – p_4 to radial modes of $1.1M_\odot$ models. Lines (color coded as indicated) without symbols, with triangles, and with circles indicate period ratios to radial first (1O), second (2O), and third overtones (3O), respectively.

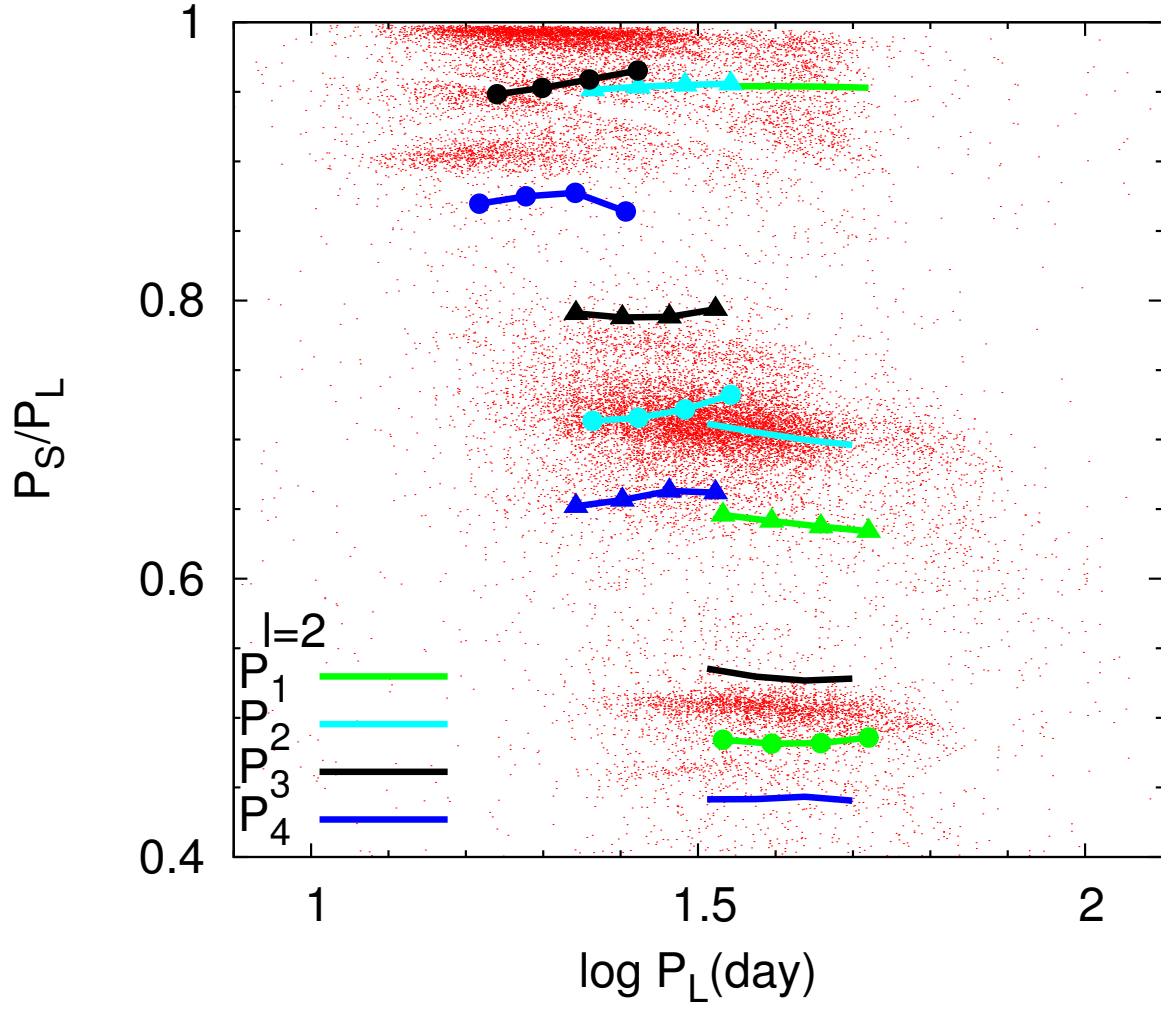


Fig. 10.— The same as Fig. 9 but for non-radial quadrupole ($l = 2$) p modes, p_1 – p_4 .

the evolutionary sequence of a single initial mass cannot explain the whole range of luminosities (and hence periods) observed. We have to consider a mass distribution along the ridges in the PL relations. [Soszyński et al. \(2007\)](#) and [Dziembowski & Soszyński \(2010\)](#) used isochrones of several ages for the relations between mass and luminosity. Here, we take a more general procedure to obtain the relation between mass and luminosity, using the observed PL relations, in particular sequence b_3 .

In order to compare with theoretical relations we have converted the period–magnitude relations shown in Figure 5 to PL relations in the following way: K and J magnitudes of each star are obtained from 2MASS photometry data, bolometric corrections for the K magnitudes

$$BC_K = 0.72 + 2.65(J - K) - 0.67(J - K)^2 \quad (4.5)$$

([Bessell & Wood 1984](#)) are applied, and the LMC distance modulus, 18.54 [mag] ([Tabur et al. 2010](#)) is adopted.

For each initial mass we adopt the luminosity range such that the theoretical PL relation lies within the ‘band’ of sequence b_3 as shown by solid lines in Figure 11. The boundary of sequence b_3 has been determined as follows. First we chose stars bounded by $1.3 \log P + 1.28 \leq \log L/L_\odot \leq 1.3 \log P + 1.51$ and $2.7 \leq \log L/L_\odot \leq 3.4$ (dashed red lines in Figure 11) as tentative members of b_3 . Then we calculated cumulative numbers as a function of period in each luminosity bin and normalized it to unity at the longest period considered. We name this as the normalized cumulative fraction $\Phi_L(P)$ (an example is shown in the bottom panel of Figure 11). We regard the width of the sequence b_3 at a given luminosity is bounded by periods where $\Phi_L(P) = 0.05$ and 0.95 (dotted lines in the bottom of Figure 11). We determine such boundaries for each luminosity bin and taking means with adjacent luminosity bins to obtain a smooth curve, as shown by the black solid line in the top panel of Figure 11.

Using thus obtained boundary for the sequence b_3 , we have determined the luminosity range for each mass. An example is shown in the top panel of Figure 11. The two blue lines show period to luminosity relations for radial 3O and non-radial $p_4(l = 1)$ modes of $1.1M_\odot$ evolutionary models. We adopt the appropriate luminosity range for the mass such that the both lines are within the boundary of b_3 ; the part is indicated by solid lines.

Similarly, we have determined luminosity ranges for models with initial masses of 0.9, 1.0, 1.2, 1.3 and $1.4M_\odot$. Figure 14 compares thus obtained theoretical PL relations (top panel) and period to period-ratio relations (bottom panel) with observations. This figure demonstrates that our models reproduce the characteristic distributions of RGB OSARGs in the PL and Petersen diagrams quite well. Our models for the RGB OSARGs consist of the three radial overtones and the two non-radial $p_4(l = 1)$, and $p_2(l = 2)$ modes in the evolutionary models having masses between 0.9 and $1.4M_\odot$: each mass contributes only in the corresponding appropriate luminosity range. The model parameters at the low and high ends within the luminosity range, and at the central of the range are listed in Table 1. Figure 12 shows where the luminosity ranges listed in Table 1 lie in the Hertzsprung–Russell (HR) diagram. We note that the model effective temperatures corresponding

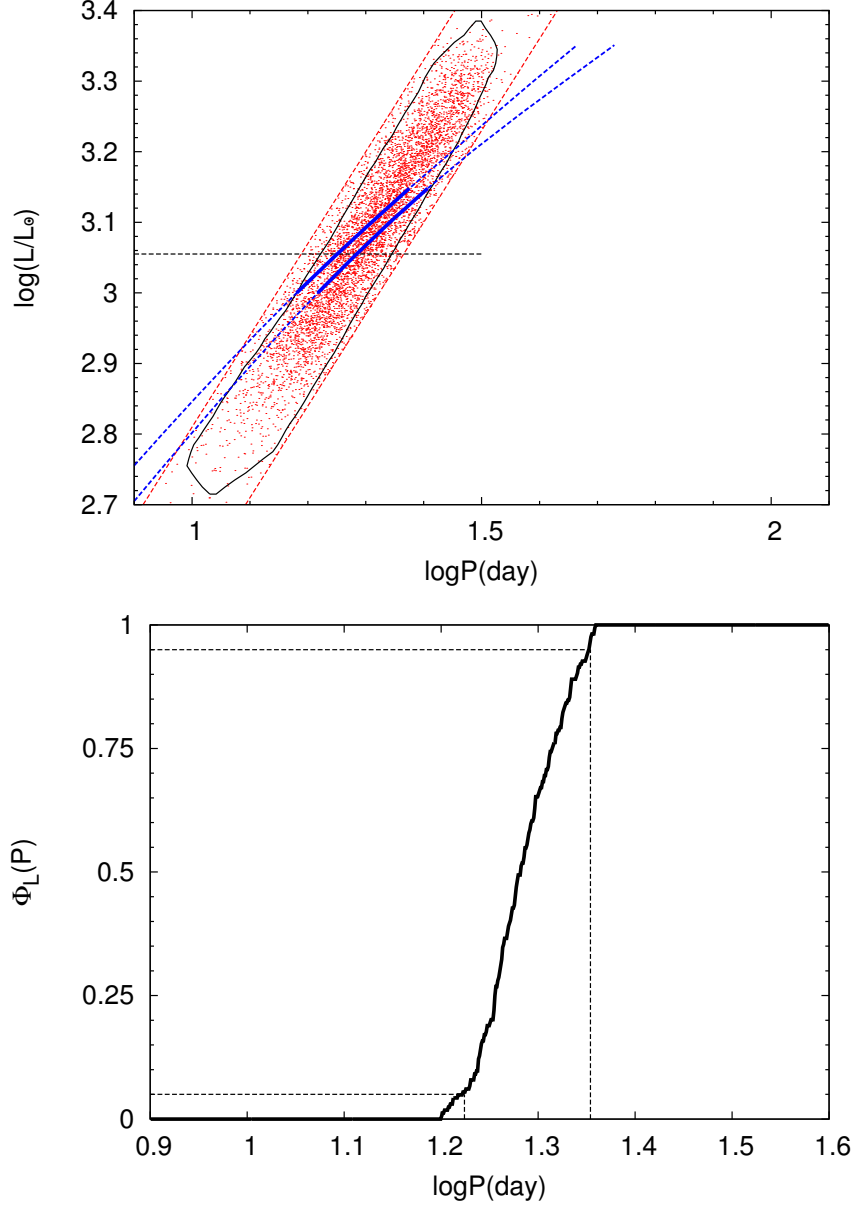


Fig. 11.— The top panel shows period to luminosity relation obtained from only stars around sequence b3 (red points; see text for how these stars are chosen). The black solid line is the quantitative boundary of the sequence b3 defined using the cumulative distribution function, an example of which is shown in the bottom panel. Dashed (and partially solid) blue lines are relations for the radial 3O and non-radial $p_4(l=1)$ modes of $1.1M_\odot$. The luminosity range adopted for the mass is shown by the part of solid lines. The bottom panel shows a cumulative number of stars in a luminosity bin at $\log L/L_\odot = 3.06$. It is normalized to unity at the longest period and is named as $\Phi_L(P)$. We have determined boundary of the sequence b3 by assuming that stars lay in the period range where $0.05 \leq \Phi_L(P) \leq 0.95$; i.e. the range bounded by dotted lines for the luminosity.

to the luminosity range derived from a comparison of the model with the observation fall within narrow limits and an approximately vertical strip appears on the HR diagram by the different masses. Some other non-radial modes may be involved because clumps in the period ratios and ridges in the PL plane are broad. We note that the need of different masses for different luminosity ranges comes from the fact that the PL relation of a single mass has a inclination slightly different from the observed one.

Table 1: Mass and luminosity ranges for the RGB star models

Initial mass (M_{\odot})	M_{\min} (M_{\odot})	$\log \frac{L_{\min}}{L_{\odot}}$	$\log T_{\text{eff},\min}$ (K)	M_{mid} (M_{\odot})	$\log \frac{L_{\text{mid}}}{L_{\odot}}$	$\log T_{\text{eff},\text{mid}}$ (K)	ν_{max} (d)	M_{max} (M_{\odot})	$\log \frac{L_{\text{max}}}{L_{\odot}}$	$\log T_{\text{eff},\text{max}}$ (K)
0.90	0.85	2.75	3.55	0.84	2.85	3.54	19.71	0.82	2.95	3.52
1.00	0.94	2.86	3.54	0.93	2.96	3.53	23.87	0.91	3.06	3.52
1.10	1.03	3.00	3.53	1.02	3.07	3.52	29.89	1.00	3.15	3.51
1.20	1.12	3.10	3.53	1.11	3.17	3.52	35.72	1.09	3.24	3.51
1.30	1.22	3.18	3.53	1.20	3.24	3.52	39.52	1.19	3.30	3.51
1.40	1.31	3.25	3.52	1.30	3.30	3.52	42.53	1.29	3.35	3.51

Note, the subscripts ‘min’ and ‘max’ correspond to the parameters at the low and high luminosity edges of a luminosity range for an initial mass while ‘mid’ indicates the parameters at the center of the luminosity range. ν_{max} is a scaled optimal frequency at L_{mid} defined as Equation 4.7.

Figure 13 shows the relation between the central value of the luminosity range and mass which can be expressed as an empirical formula

$$\log L/L_{\odot} = 0.91(M/M_{\odot}) + 2.05 \quad (4.6)$$

obtained by a least square fitting. We note that the mass-luminosity relation given in this equation corresponds to ages ranging from about 12.7 Gyr ($0.9M_{\odot}$) to 2.6 Gyr ($1.4M_{\odot}$); indicating massive stars are younger than less massive ones. This means that our mass-luminosity relation is significantly different from isochrone relations.

Dziembowski & Soszyński (2010) argued that pulsations in OSARGs should be excited stochastically by turbulent convection because the run of the scaled optimal frequency ν_{\max} is consistent with the frequencies of sequences b_2 and b_3 , where ν_{\max} is defined as

$$\nu_{\max} = \frac{L_{\odot}}{L} \frac{M}{M_{\odot}} \left(\frac{T_{\text{eff}}}{T_{\text{eff}\odot}} \right)^{3.5} \times 3050 \mu\text{Hz}. \quad (4.7)$$

Amplitude is maximum at the frequency ν_{\max} in solar-like oscillations excited stochastically by turbulent convection. The relation was first obtained by Kjeldsen & Bedding (1995), scaling the frequency at maximum power of the solar oscillations. We plot in Figure 14 (top panel; black dotted line) the run of $1/\nu_{\max}$, the optimal period for the stochastic excitation, calculated using equation (4.6) and corresponding effective temperature at each luminosity. Also plotted for comparison (cyan dotted line) is the run of $1/\nu_{\max}$ calculated by using the evolutionary track of the $1.1M_{\odot}$ model with $(Z, \alpha) = (0.004, 1.5)$. For both of the cases, $1/\nu_{\max}$ goes through roughly middle of the PL relations of OSARGs. This suggests, in agreement with Dziembowski & Soszyński (2010), that pulsations in OSARGs are stochastically excited by turbulent convection, and hence kin to the solar-like oscillations measured in many less luminous red-giants by CoRoT and Kepler (e.g., De Ridder et al. 2009; Bedding et al. 2010). The similarity is also discussed in e.g., Soszyński et al. (2007); Tabur et al. (2010).

5. Discussion

5.1. Effects of metallicity and mixing-length

In our analyses discussed in the previous sections we have adopted a set of parameters $(Z, \alpha) = (0.01, 1.5)$, where Z is the heavy element abundance and α is the ratio of mixing-length to pressure scale height. We examine here the effect of different choices of (Z, α) . Figure 15 compares the period/period-ratio relations of radial modes (3O/1O, 2O/1O, and 3O/2O) for the standard set $(Z, \alpha) = (0.01, 1.5)$ with the $(Z, \alpha) = (0.004, 1.5)$ and $(0.01, 1.8)$ cases for $1.1M_{\odot}$ models in the luminosity range $2.7 \leq \log L/L_{\odot} \leq 3.35$. This figure shows that changing metallicity or mixing length hardly changes period ratios, although periods themselves shifts considerably. (Similar results were obtained for different masses in a range of $0.9 \leq M/M_{\odot} \leq 1.4$.)

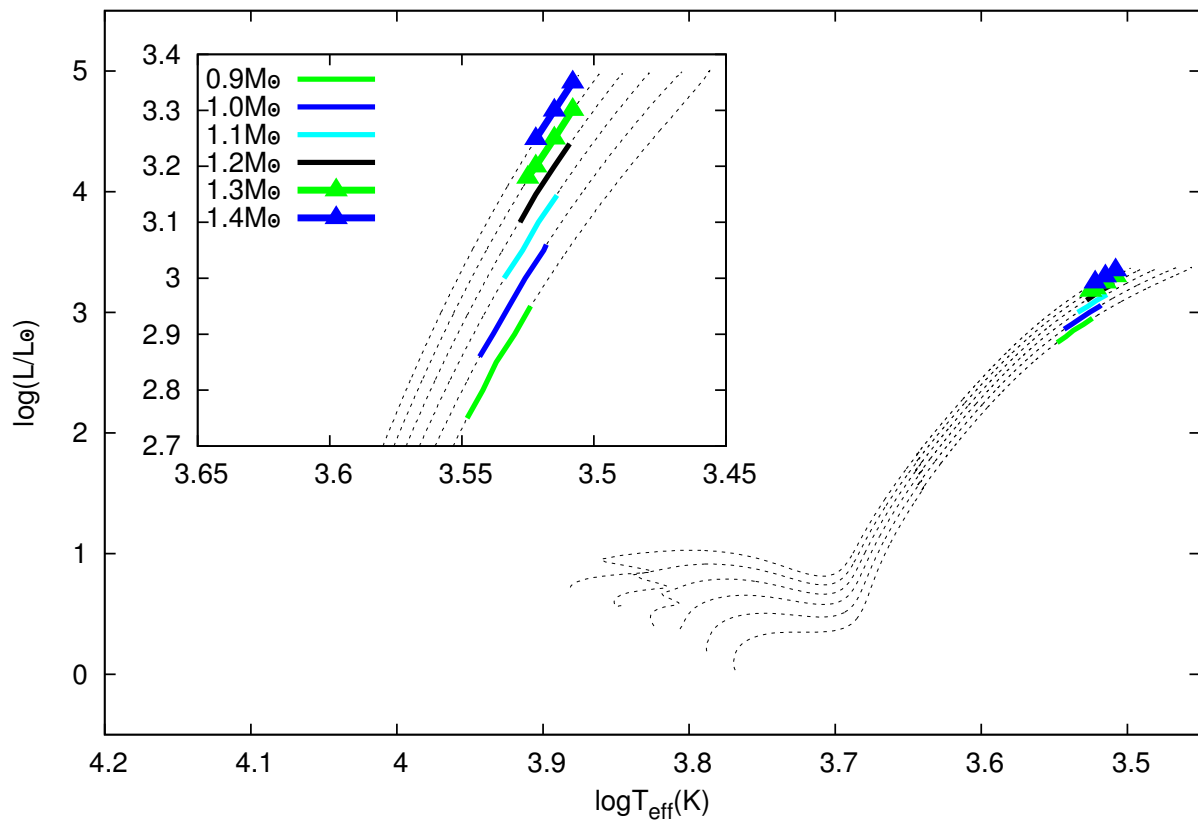


Fig. 12.— The positions for the luminosity ranges listed in Table 1 on the HR diagram. The colored thick lines correspond to the models for the indicated initial masses in the top left on the diagram. The black dashed lines show the evolutionary tracks for the models below the tip of the red giant branch.

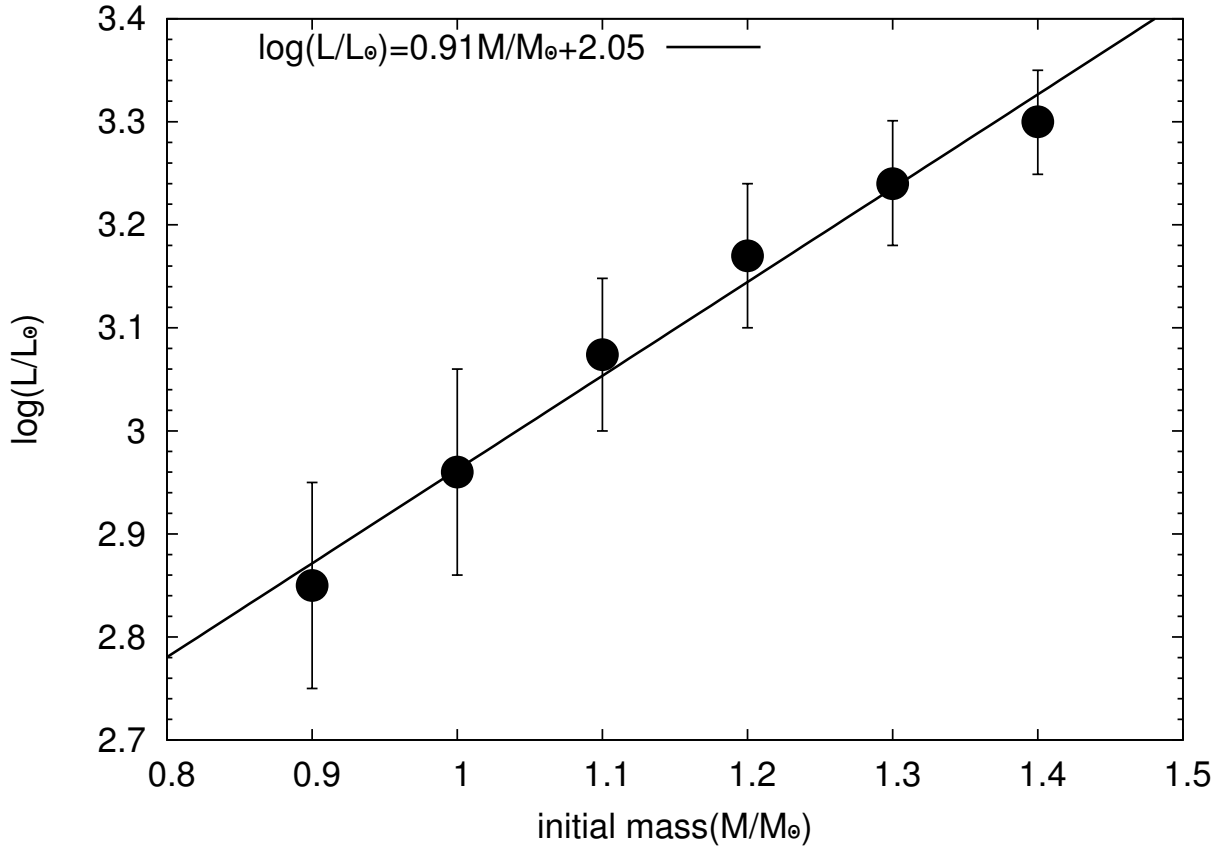


Fig. 13.— The relation between the central value of the luminosity range and mass. The bar corresponds to the luminosity range in a initial mass listed in Table 1.

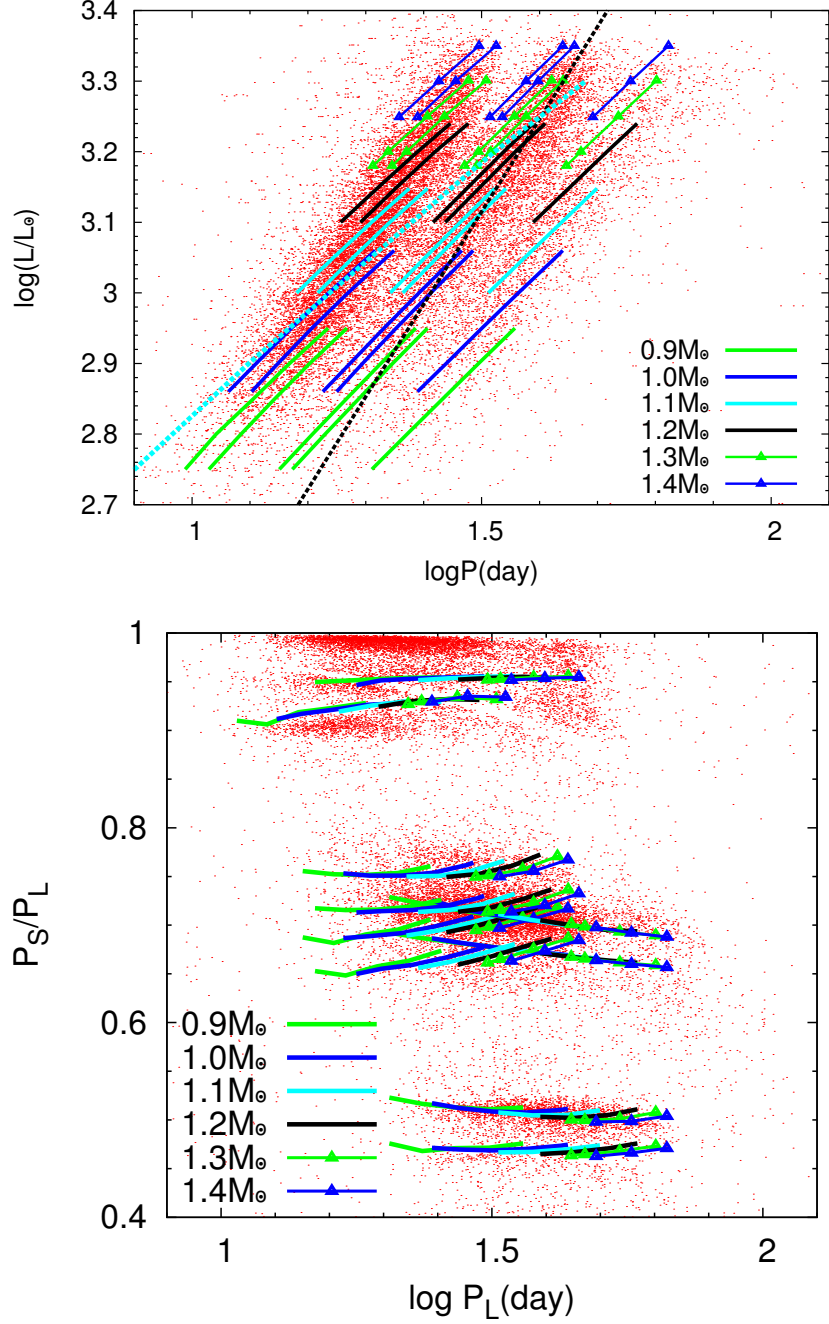


Fig. 14.— Our best models are compared in the PL plane (top panel) and in the period vs period-ratio plane (bottom panel) with RGB OSARGs in the LMC. Our theoretical relations include radial first to third overtones and the dipole $p_4(l=1)$ mode and the quadrupole $p_2(l=2)$ mode in models with masses in the range $0.9 \leq M/M_\odot \leq 1.4$. The luminosity range of each mass is determined by fitting with the observed b3 sequence as illustrated in Figure 11. Black dotted line in the top panel shows the scaled relation $1/\nu_{\text{max}}$ given by equation (4.7) using the mass to mean luminosity relation given in equation (4.6) and the corresponding effective temperature. Cyan dotted line shows $1/\nu_{\text{max}}$ computed using the evolutionary track of the 1.1 M_\odot model with $(Z, \alpha)=(0.004, 1.5)$.

The period shifts are caused by changes in radius; lower Z or higher α makes the radius smaller (and hence the period shorter) at a given luminosity due to more efficient energy transport. To have the same period we have to adopt a slightly smaller mass compared to our standard case. Although appropriate mass ranges might shift slightly, our mode identifications for the PL sequences b_1 to b_3 are not affected by changing metallicity or mixing-length.

5.2. Connection to the solar-like oscillations in G/K giants

Another fact supporting the stochastic excitation of OSARG pulsations may be found in the period– M_K diagram shown by Tabur et al. (2010) which shows the sequence of solar-like oscillations in G/K giants extends toward the place where OSARGs are located. The left-hand panel of Figure 16 is a similar diagram, which shows the relation between luminosity and the period at the maximum amplitude ($1/\nu_{\max}$) for red giants in the Galactic open clusters NGC 6791 and NGC 6819 obtained by Basu et al. (2011) from Kepler data. The difference between NGC 6791 (squares) and NGC 6819 (triangles) comes from a difference in the range of stellar masses; stars in the latter cluster systematically more massive ($\sim 1.6\text{--}2.0M_{\odot}$) than those in the former cluster ($\sim 1.0\text{--}1.5M_{\odot}$) according to the seismic mass determinations by Basu et al. (2011). Also plotted are PL relations of our sample RGB OSARGs (red dots).

The right-hand panel of Figure 16 shows $\nu_{\max}/\Delta\nu$ of the solar-like oscillations in the cluster giants, where $\Delta\nu$ means the large separation. The value of $\nu_{\max}/\Delta\nu$ is roughly equal to the number of radial nodes in the maximally excited mode. The vertical dashed line indicate the number of radial node (3) for the radial third overtone mode which we fit to the sequence b_3 of OSARGs. The radial order of the modes excited in the solar-like oscillations decreases with increasing luminosity, which is consistent with the fact that only low-order modes are excited in the OSARGs.

These diagrams indicate that the properties of OSARGs can be understood as the high luminosity (and hence long period) extension of the solar-like oscillations in G/K giants; in other words OSARGs are likely excited stochastically by turbulent convection.

6. Summary

We studied PL relations and period ratios of RGB OSARGs in the LMC, and found that these relations can be explained by radial first to third overtones and non-radial $p_4(l=1)$ and $p_2(l=2)$ modes in evolving red giant models having masses between about 0.9 and $1.4M_{\odot}$ for our standard parameters of $(Z, \alpha) = (0.01, 1.5)$. Although different choices for the parameters would shift the mass ranges, mode identifications are not affected because the period ratios hardly depend on these parameters. The sequence b_1 is fitted by radial 1O, b_2 by radial 2O and non-radial $p_2(l=2)$, and b_3 by radial 3O and non-radial $p_4(l=1)$ modes. The reason why only the two non-radial modes are observed is not clear.

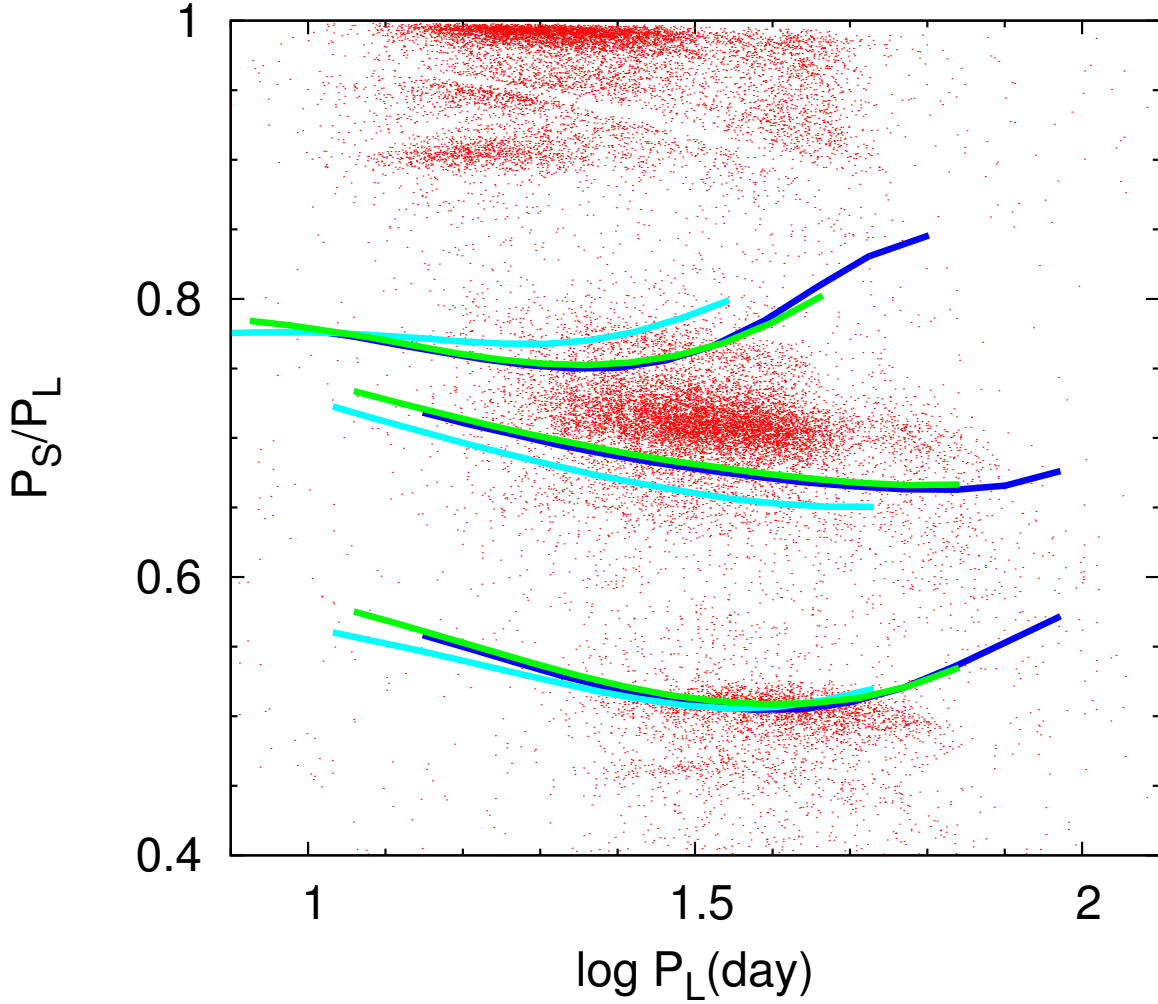


Fig. 15.— The same as Figure 8 but including models with (Z, α) different from our standard values. Blue lines are for the standard models (i.e., the same as in Figure 8), cyan lines are for models with a low metallicity ($Z = 0.004$), and green lines for models with a longer mixing length ($\alpha = 1.8$).

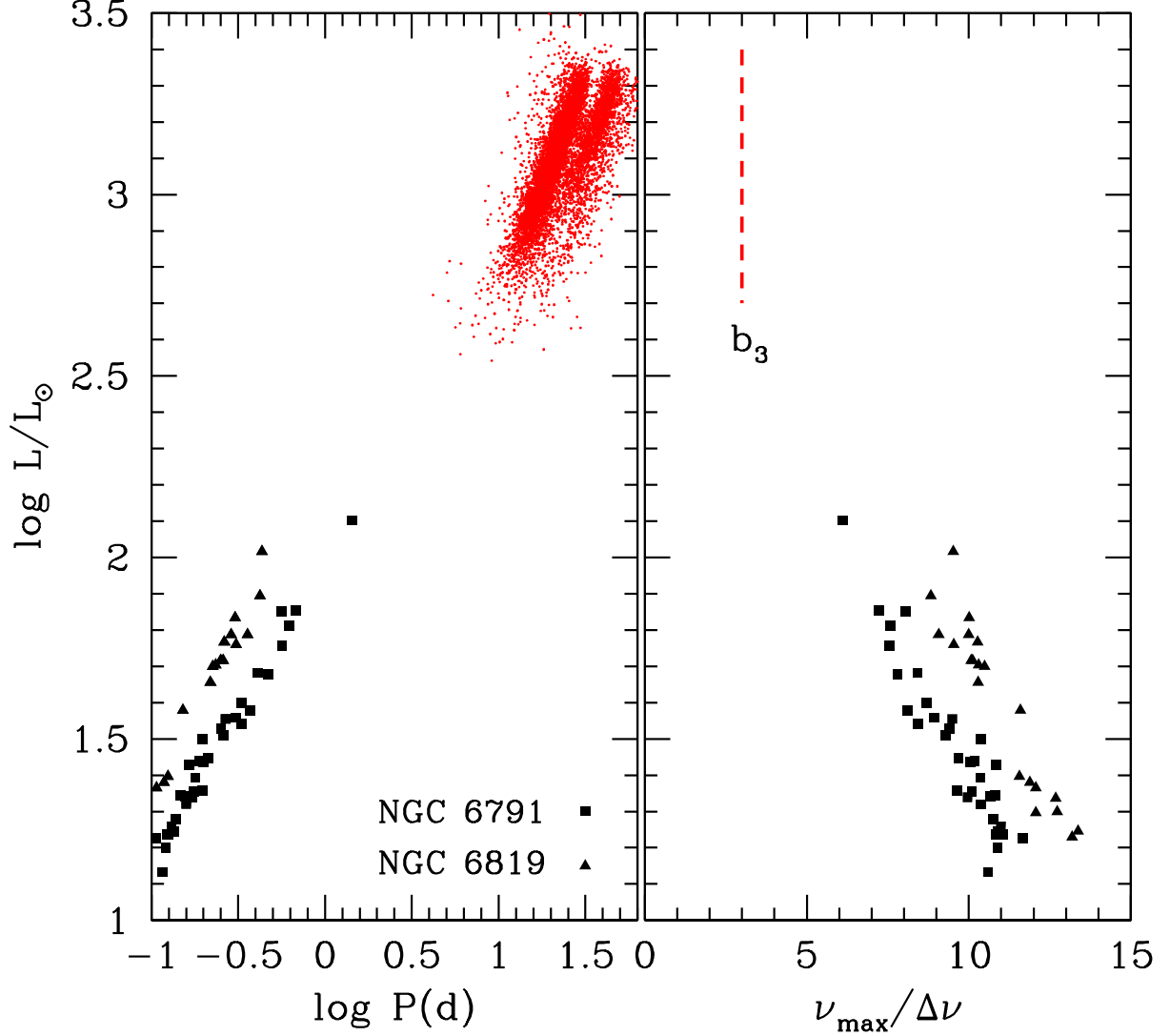


Fig. 16.— Pulsation properties of OSARGs compared with solar-like oscillations of open cluster giants in NGC 6791 and NGC 6819 obtained by [Basu et al. \(2011\)](#) from *Kepler* data. Left-hand panel shows luminosity versus period ($1/\nu_{\max}$) of maximally excited mode in the solar-like oscillations of the cluster giants, and PL relations of OSARGs in the LMC (red dots), where only the primary period for each OSARG is plotted. Right-hand panel shows luminosity versus $\nu_{\max}/\Delta\nu$ which gives the approximate number of radial nodes for the maximally excited mode in the cluster giants. The vertical dashed line indicates the number radial nodes of radial 3O mode which we fit to the sequence b_3 .

The scaled ν_{max} of solar-like oscillations evaluated with our model parameters goes through roughly the middle of the three ridges populated by RGB OSARGs in the PL plane. In addition, the PL relations look like a high-luminosity extension of the solar-like oscillations recently detected by the *Kepler* satellite in G/K giants of the open clusters NGC 6791 and NGC 6819. These facts strongly suggest that pulsations in OSARGs are stochastically excited by turbulent convections.

Part II

Long Secondary Period

Long-term *JHK* light curves have recently become available for large numbers of the more luminous stars in the SMC. We have used these *JHK* light curves, along with OGLE *V* and *I* light curves, to examine the variability of a sample of luminous red giants in the SMC which show prominent long secondary periods (LSPs). The origin of the LSPs is currently unknown. In oxygen-rich stars, we found that while most broad band colours (e.g. $V - I$) get redder when an oxygen-rich star dims during its LSP cycle, the $J - K$ colour barely changes and sometimes becomes bluer. We interpret the $J - K$ colour changes as being due to increasing water vapour absorption during declining light caused by the development of a layer of dense cool gas above the photosphere. This result and previous observations which indicate the development of a chromosphere between minimum to maximum light suggest that the LSP phenomenon is associated with the ejection of matter from the stellar photosphere near the beginning of light decline. We explore the possibility that broadband light variations from the optical to the near-IR regions can be explained by either dust absorption by ejected matter or large spots on a rotating stellar surface. However, neither model is capable of explaining the observed light variations in a variety of colour–magnitude diagrams. We conclude that some other mechanism is responsible for the light variations associated with LSPs in red giants.

7. The observational data

7.1. The near-IR data

A long-term multiband near-IR photometric survey for variable stars in the Large and Small Magellanic Clouds has been carried out at the South African Astronomical Observatory at Sutherland (Ita et al., in preparation). The SIRIUS camera attached to the IRSF 1.4 m telescope was used for this survey and more than 10yr of observations in the near-IR bands $J(1.25\mu\text{m})$, $H(1.63\mu\text{m})$ and $K_s(2.14\mu\text{m})$ band were obtained. In this work, we select the SMC stars from the SIRIUS data base. Variable and non-variable stars in an area of 1 deg^2 in the central part of the SMC have been observed about 99–126 times in the period 2001–2012 and a total of 340147, 301841 and 215463 sources were identified in J , H and K_s , respectively. We note that the photometric detection range of the SIRIUS camera is about 8–18 magnitudes in the K_s band. A total of 12008 variable sources of all kinds were detected of which 4533 were detected in all three wavebands (data release ver 130501; Ita et al., in preparation).

7.2. The optical data

We obtained the V - and I - band time series of SMC red giants from the OGLE project (Soszyński et al. 2011). Typically, about 1000 observing points were obtained in the I band by OGLE-II+III while a much smaller number of about 50–70 points were obtained in the V band.

Soszyński et al. (2011) divided the LPVs into LSP and non-LSP stars according to their positions in the period–luminosity relations for variable red giants. We found nearly 700 LSP stars in the area of the IRSF infrared survey. In order to determine if an LSP star is oxygen-rich or carbon-rich, we initially adopted the classification method introduced by Soszyński et al. (2011). The stars we examined in detail had their oxygen-rich or carbon-rich status checked against optical spectral classifications in the literature.

7.3. The combined near-IR and optical data

By combining the SIRIUS data with the OGLE data, we obtained 298 oxygen-rich LSP stars and 88 carbon-rich LSP stars in the region monitored by the SIRIUS camera. For all sample stars, a small number of apparent bad data points were removed from each time series. Then, by using a first-order Fourier fit to the I -band time series, we obtained the period and amplitude corresponding to the largest amplitude mode of the light curves. In all cases, the obtained periods and amplitudes were almost identical to those in the OGLE-III catalogue (Soszyński et al. 2011). Using the period from the fit to the I light curve, a fit was also made to the K_s light curve in order to derive its amplitude.

Since our aim is to look for and to model colour and magnitude changes, we need the observed changes to be significantly larger than the noise in the data. The limiting factor in this study is noise in the near-IR data. We concentrate on the brightest stars with $K_s < 13$ and for them the useful lower limit for clearly apparent K_s -band variation is about 0.04 mag. Similarly, we set a useful lower limit for the I -band variation of about 0.2 mag. Figure 17 shows the full amplitude of the observed LSP stars in the I and K_s bands. This figure shows the selected stars, which having full amplitudes larger than 0.04 mag in K_s and 0.2 mag in I . This selection gave us a sample of 7 oxygen-rich stars and 14 carbon stars for analysis. The spectral types of our sample stars obtained from the OGLE photometry agree with the classifications in the SIMBAD astronomical data base where the spectral types were obtained from spectroscopic determinations. The properties of these stars at maximum light are listed in Table 2. Figure 18 represents the I -band light curves for a sample of 21 LSP stars observed by OGLE-III. The light curves are folded with the period corresponding to the largest amplitude mode. A sample of 21 LSP stars show short period variations possibly corresponding to pulsation of the stars. The periods corresponding to the largest amplitude mode of 298 oxygen-rich LSP stars and 88 carbon-rich LSP stars including a sample of 7 oxygen-rich stars and 14 carbon stars are plotted with the K_s magnitudes in Figure 19. Most of those periods lie in a distinct PL sequence corresponding to the sequence D. This indicates that the period we

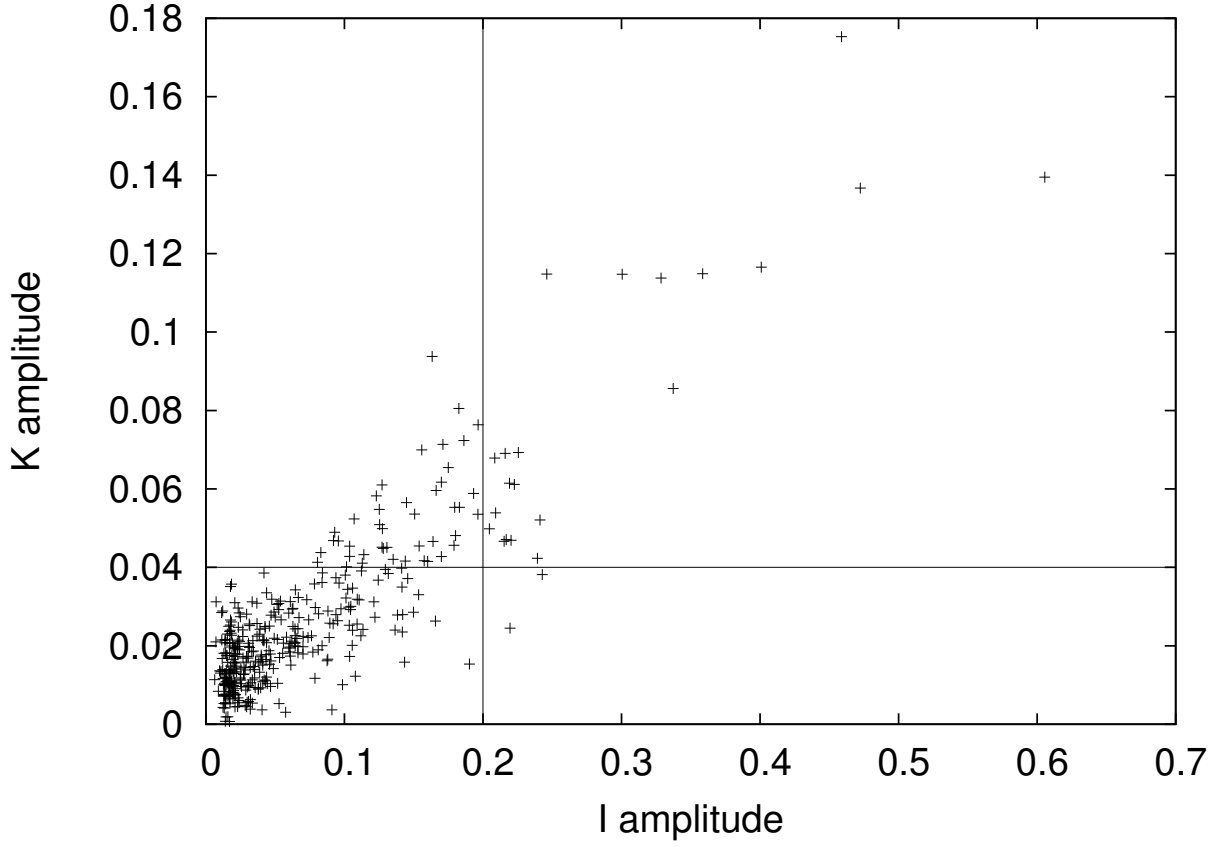


Fig. 17.— The relation between the I - and K_s - band full amplitude of 298 oxygen-rich stars and 88 carbon stars. The stars selected for detailed study have I amplitude greater than 0.2 mag and K_s amplitude greater than 0.04 mag.

obtained likely correspond to LSP. Note; the K_s magnitude used for Figure 19 is equal to the mean magnitude over the light curves, not corresponding to the magnitude at the maximum light.

Table 2: Basic parameters of the program stars at maximum light

Name	RA	Dec	V (mag)	I (mag)	J (mag)	H (mag)	K_s (mag)	L (L_\odot)	T_{BB} (K)	T_{eff} (K)	P_{LSP} (d)	Sp. type
OGLE-SMC-LPV-07852	12.402540	-72.97075	16.60	14.34	12.91	12.05	11.73	4617	2803	3434	645	O
OGLE-SMC-LPV-09856	13.186620	-72.95178	16.49	14.37	12.96	12.10	11.86	4408	2928	3558	615	O
OGLE-SMC-LPV-10774	13.530120	-72.47989	–	14.98	13.73	12.81	12.57	2170	2844	3474	396	O
OGLE-SMC-LPV-12332	14.166840	-73.07389	–	14.26	12.95	12.08	11.82	4455	2887	3517	632	O
OGLE-SMC-LPV-14045	14.987085	-72.94936	17.50	15.13	13.72	12.79	12.57	2197	2865	3495	390	O
OGLE-SMC-LPV-14715	15.332205	-72.86369	–	14.27	12.92	12.03	11.75	4544	2815	3445	601	O
OGLE-SMC-LPV-14781	15.361920	-72.85678	16.48	14.62	13.30	12.44	12.23	3245	2991	3620	469	O
OGLE-SMC-LPV-08199	12.555540	-73.18697	17.75	14.90	13.29	12.27	11.64	3745	2203	2792	767	C
OGLE-SMC-LPV-08280	12.583995	-72.80533	16.36	13.78	12.33	11.36	10.93	7922	2490	3106	1008	C
OGLE-SMC-LPV-09341	12.990495	-73.20256	–	13.92	12.48	11.63	11.26	6419	2734	3362	1081	C
OGLE-SMC-LPV-10109	13.281915	-73.12992	16.08	13.84	12.52	11.60	11.20	6411	2592	3215	964	C
OGLE-SMC-LPV-12653	14.317380	-72.80128	–	14.83	13.10	12.03	11.44	4465	2200	2789	1356	C
OGLE-SMC-LPV-13340	14.654580	-72.44625	16.28	14.12	12.59	11.66	11.28	6003	2606	3230	1014	C
OGLE-SMC-LPV-13557	14.755710	-72.46908	16.31	13.91	12.45	11.54	11.13	6876	2592	3215	1032	C
OGLE-SMC-LPV-13748	14.847210	-73.04900	–	14.69	13.09	12.11	11.67	3977	2468	3082	925	C
OGLE-SMC-LPV-13802	14.871165	-72.65750	17.08	14.19	12.69	11.71	11.16	6085	2334	2936	1011	C
OGLE-SMC-LPV-13945	14.946045	-72.71094	–	14.06	12.63	11.73	11.29	5872	2560	3180	927	C
OGLE-SMC-LPV-14084	15.004245	-72.89839	16.30	14.27	12.74	11.83	11.53	5042	2759	3388	799	C
OGLE-SMC-LPV-14159	15.048705	-72.66822	–	14.42	12.96	12.04	11.57	4406	2495	3112	913	C
OGLE-SMC-LPV-14829	15.382875	-73.09919	15.69	13.70	12.37	11.54	11.21	6950	2839	3469	780	C
OGLE-SMC-LPV-14912	15.434040	-73.29506	–	14.49	12.92	11.91	11.31	5135	2244	2837	722	C

Notes. T_{BB} is the blackbody temperature derived from $J - K_s$ while T_{eff} is the effective temperature derived from $J - K_s$ using the formula in [Bessell, Wood, & Evans \(1983\)](#). Luminosities L were derived by applying a bolometric correction to K_s (see Section 8.1).

7.4. Separating the LSP variation from the primary period variation

Light curves of all LSP stars show variations with the period corresponding to sequence D and also variations with the primary period, which mainly corresponds to sequence B. Therefore, in order to study the LSP variation only, we need to separate each light curve into the components due to variation with the LSP and variation with the primary period. The separation method we used is now described.

At first, we adopted a reference time t_0 and then delimited the light curve into time intervals equal to the size of the LSP (P), with t_0 as the start of an interval. Then we fitted the observed data points in each interval independently using a second-order Fourier series F_0 with the period equal to that of the LSP,

$$F_0(t) = A_0 + \sum_{i=1}^2 a_i \sin\left(2\pi i \frac{t-t_0}{P}\right) + b_0 \cos\left(2\pi i \frac{t-t_0}{P}\right).$$

The fit was performed on independent intervals of length P rather than the full light-curve interval because the light curves of LSP stars vary substantially from cycle to cycle of the LSP. Furthermore, in order to minimize the dependence of the final fit on the adopted value of t_0 , the fit was made using four values for t_0 , τ_0 , τ_1 , τ_2 and τ_3 , with each of these values increasing by $\frac{1}{4}P$, giving fits $F_0(t)$, $F_1(t)$, $F_2(t)$ and $F_3(t)$, respectively. In this study, τ_0 corresponds to JD2450000. A requirement for a fit to be made was that there be at least six points in each of the first and second halves of the fit interval. If such points were not available, no fit was made. The final adopted fit $F(t)$ at the observed times is given by

$$F(t) = \frac{1}{4} \sum_{j=0}^3 F_j(t).$$

When there were fewer than four fits, the average was taken over the number of fits available. An example of the final light-curve fits for each band in a representative star is shown in Figure 20.

As one can see from Figure 20, observation times of the OGLE I band usually differed from those of the OGLE V band and the SIRIUS J , H and K_s bands, the latter being taken simultaneously. The I -band observations are always the most frequent. In our analysis, we will examine colours relative to the I -band magnitude. In order to derive the colours and I -band magnitudes at simultaneous dates, the I -band fits to the LSP variations were used. Magnitudes and colours were derived from the fits at observation times of the V band and the K_s band. As noted above, fits are not available at all times in a given band.

8. Modeling the LSP magnitude and colour variations

We will now create models for the magnitude variations in various bands associated with LSPs in order to see if the assumed models are consistent with the observations. The two models we examine are obscuration by dust and the variation of spots on a star.

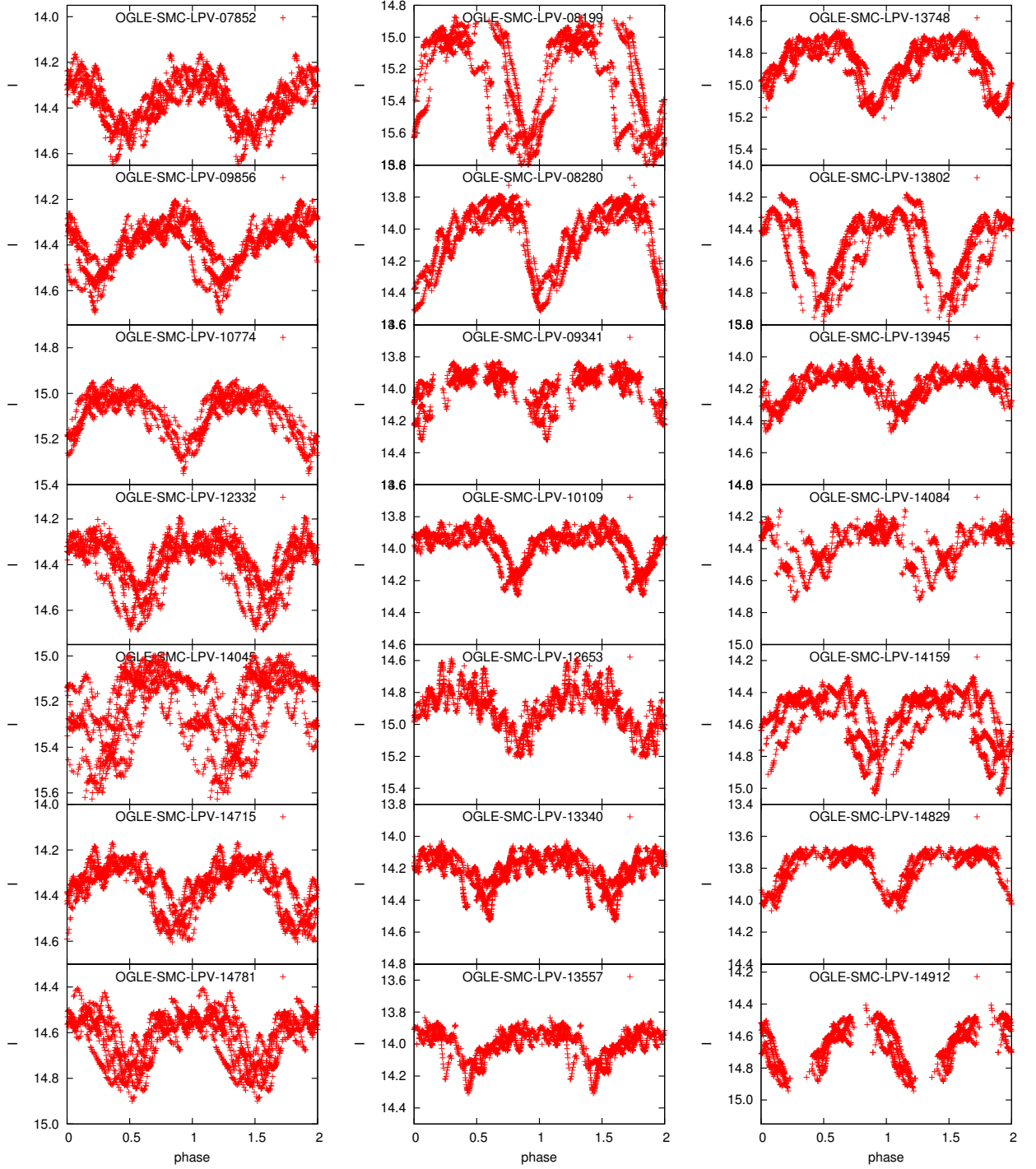


Fig. 18.— Light curves in I band for a sample of 21 LSP stars. The 7 panels of the left column correspond to the oxygen-rich stars and the 14 panels of the middle and right columns are for the carbon stars. All the light curves are folded with the LSPs shown in Table 2.

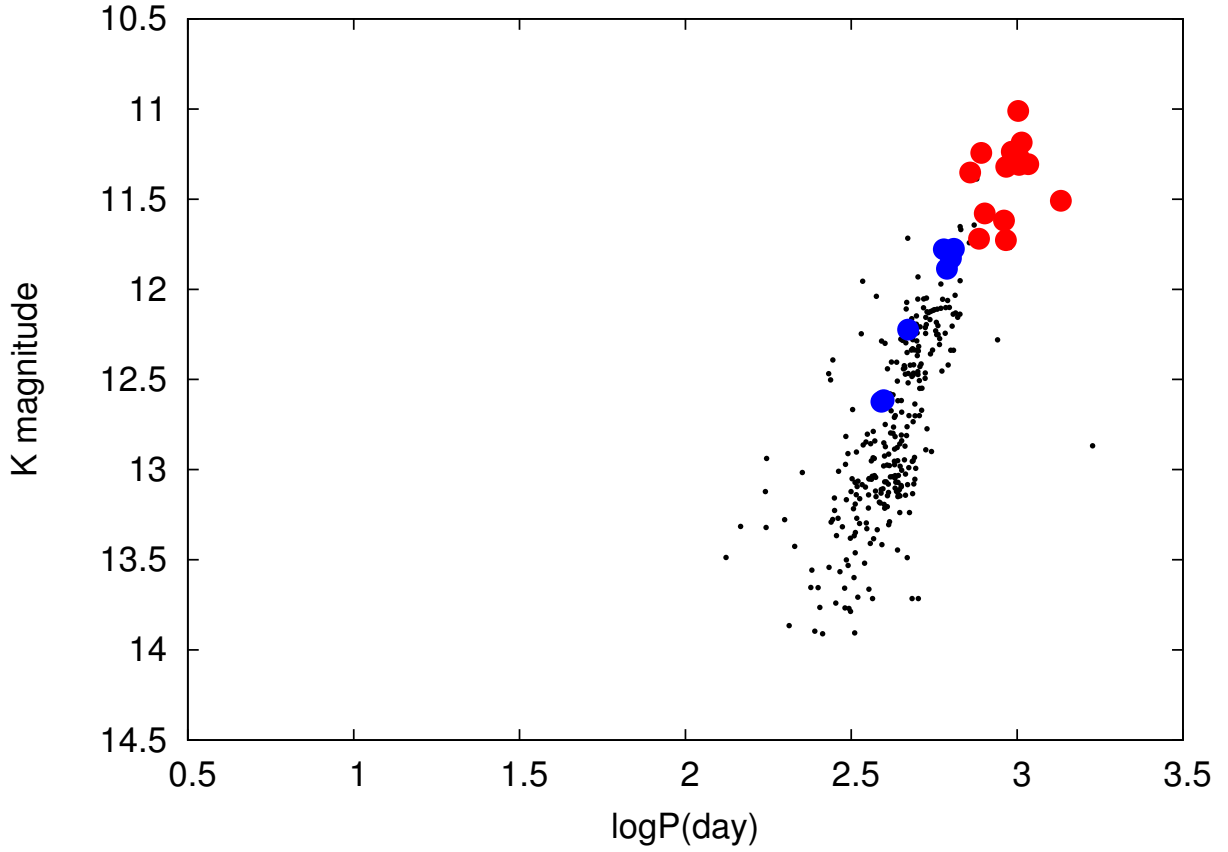


Fig. 19.— Period- K_s magnitude diagram for the LSP stars in the SMC. The black dots show 298 oxygen-rich LSP stars and 88 carbon-rich LSP stars while the blue and red filled circles are for a sample of 7 oxygen-rich stars and 14 carbon star, respectively.

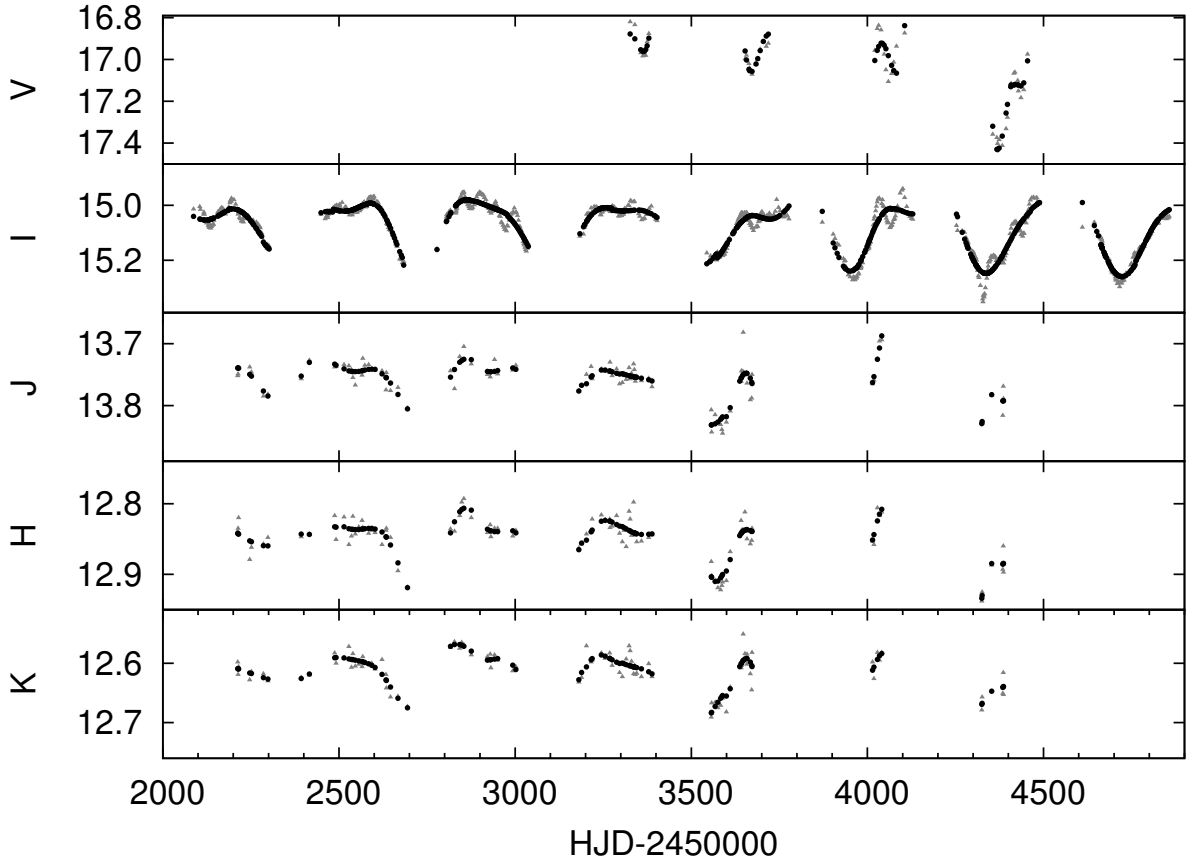


Fig. 20.— The complete light curves of OGLE-SMC-LPV-10774 ($P=396$ d) in the bands $V I J H K$. The raw data points are shown as small filled grey triangles while the fit values are shown as large filled black circles.

8.1. The dust model

One possible explanation of the LSP phenomenon is episodic circumstellar dust absorption. Here we assume that the central star ejects mass for several hundred days in each LSP cycle, leading to the formation of thin spherical mass shells. Dust grains which form in the ejected matter will be carried along with the expanding mass shells leading to dimming of the light from the central star. We assume that the dust shells are ejected spherically although this is not an essential aspect of the dust model for the optical and near-IR bands which we are examining since thermal emission in these bands is not strong.

The amount of dimming of a star due to circumstellar dust depends on the optical depth through the dust. For a spherical dust shell with an outer radius R_{out} (corresponding to the start of a mass ejection episode), an inner radius R_{in} (corresponding to the end of a mass ejection episode, or the dust formation radius in a newly-forming inner shell), a constant expansion velocity v and a mass ejection rate \dot{M} , the optical depth τ_λ through the shell is given by (e.g. [Groenewegen & de Jong 1993](#))

$$\tau_\lambda \propto \frac{\dot{M}\Psi Q_\lambda/a}{v\rho_g} \left(\frac{1}{R_{\text{in}}} - \frac{1}{R_{\text{out}}} \right), \quad (8.8)$$

where Ψ is the dust-to-gas mass ratio, Q_λ is the absorption efficiency of the grain at wavelength λ , a is the grain radius and ρ_g is the grain density.

We have used the DUSTY code ([Ivezić et al. 1999](#), see Appendix C for the brief introduction) to examine the effect of a spherical dust shell on the broad-band colours of LSP stars. DUSTY computes the spectral energy distribution (SED) of a dust-enshrouded LSP star for one given configuration of the dust shell. From Equation 8.8, we can see that the innermost dust shell plays the most important role for dust extinction when multiple dust shells of similar origin exist. In our model we only consider the innermost dust shell.

The first input parameter for DUSTY which we consider is the dust shell thickness. AGB stars are well-known mass-losing stars in which the terminal velocity of the mass flow is $\sim 10\text{--}20 \text{ km s}^{-1}$ ([Decin et al. 2007](#); [De Beck et al. 2010](#); [Lombaert et al. 2013](#)). On the other hand, R Coronae Borealis (RCB) stars are similarly luminous evolved stars which eject mass semi periodically in random directions ([Clayton 1996](#)). The large-amplitude variability of these stars is due to dust absorption by those ejected dust clouds which lie in the line of sight to the star. Observationally, the ejection velocity of the clouds is $\sim 200\text{--}250 \text{ km s}^{-1}$ ([Feast 1975](#); [Clayton 1996](#); [Feast 1990](#)). In view of these velocity estimates, and since we do not know what causes dust shell ejections in LSP stars, we considered two values for the wind velocity v of 15 and 220 km s^{-1} , and the velocity is assumed to be constant with radius. We assume that dust is ejected for a time interval equal to half the length of the LSP so the shell thickness is $vP/2$, where P is the length of the LSP. Our models are thus made with two values for the shell thickness.

The second input parameter we require for DUSTY is the temperature T_{in} at the inner edge of the dust shell. We assume T_{in} is the dust condensation temperature. The dust condensation

temperature is commonly assumed to lie in the range of 800–1500 K (e.g. [van Loon et al. 2005](#); [Cassarà et al. 2013](#)) and in our models we consider T_{in} values of 800 and 1500 K. We note that T_{in} determines the inner radius of the dust shell.

The third input parameter for DUSTY is the grain type. The assumed chemical composition of the grains is different for models of oxygen-rich stars and carbon stars. [van Loon et al. \(2005\)](#) used DUSTY to empirically determine possible grain types for oxygen-rich and carbon AGB stars in the LMC by requiring an acceptable fit to the SED of the observed stars. We use the grain chemical composition that they adopted. For carbon stars, we use dust grains of 50% amorphous carbon from [Hanner \(1988\)](#), 40% graphite from [Draine & Lee \(1984\)](#) and 10 % SiC from [Pègouriè \(1988\)](#) and for oxygen-rich stars, we use the astronomical silicates of [Draine & Lee \(1984\)](#).

The stellar luminosity L and the effective temperature T_{eff} of our LSP stars are also required as input to DUSTY. These were computed from the J and K_s magnitudes at maximum light, when circumstellar extinction is minimum. The T_{eff} values for the observed stars were estimated from the J - K_s colour at maximum light using the formula given in [Bessell, Wood, & Evans \(1983\)](#). We also used J - K_s to calculate a blackbody temperature T_{BB} for the central star at maximum. Luminosities were computed using a bolometric correction BC_K to the K_s magnitude. For oxygen-rich stars, we adopted the formula $\text{BC}_K = 0.60 + 2.56(J - K) - 0.67(J - K)^2$ given by [Kerschbaum et al. \(2010\)](#) and for carbon stars we adopt the formula $\text{BC}_K = 1.70 + 1.35(J - K) - 0.30(J - K)^2$ given by [Bessell & Wood \(1984\)](#). To estimate the absolute bolometric magnitude, we used the distance modulus of 18.93 to the SMC given by [Keller & Wood \(2006\)](#). The derived values for L , T_{BB} and T_{eff} are listed in Table 2. When using DUSTY, we assumed that the central star emits a blackbody spectrum of temperature T_{BB} . We are only interested in *changes* in magnitudes and colours, rather than the absolute values of the colours and magnitudes, and the blackbody assumption will have only an insignificant effect on these changes.

The final input parameter to DUSTY is the optical depth τ_V in the V band. The output from DUSTY is the SED of the central star extinguished by a shell of visible optical depth τ_V . Unless there is significant emission from the dust shell in each band under consideration, for a given value of τ_V the extinction of the central star in each band is essentially independent of the details of the shell radius or thickness.

8.2. Comparison of the dust model with observations

8.2.1. The variation of I with $I - J$

In general, the I light curves are the best sampled of the light curves in the different filters, the J , H and K_s light curves are the next best sampled and the V light curves are mostly only sparsely sampled. Thus when comparing observations against models in magnitude–colour plots, we use I as the magnitude and a colour involving I and another magnitude. The other magnitude

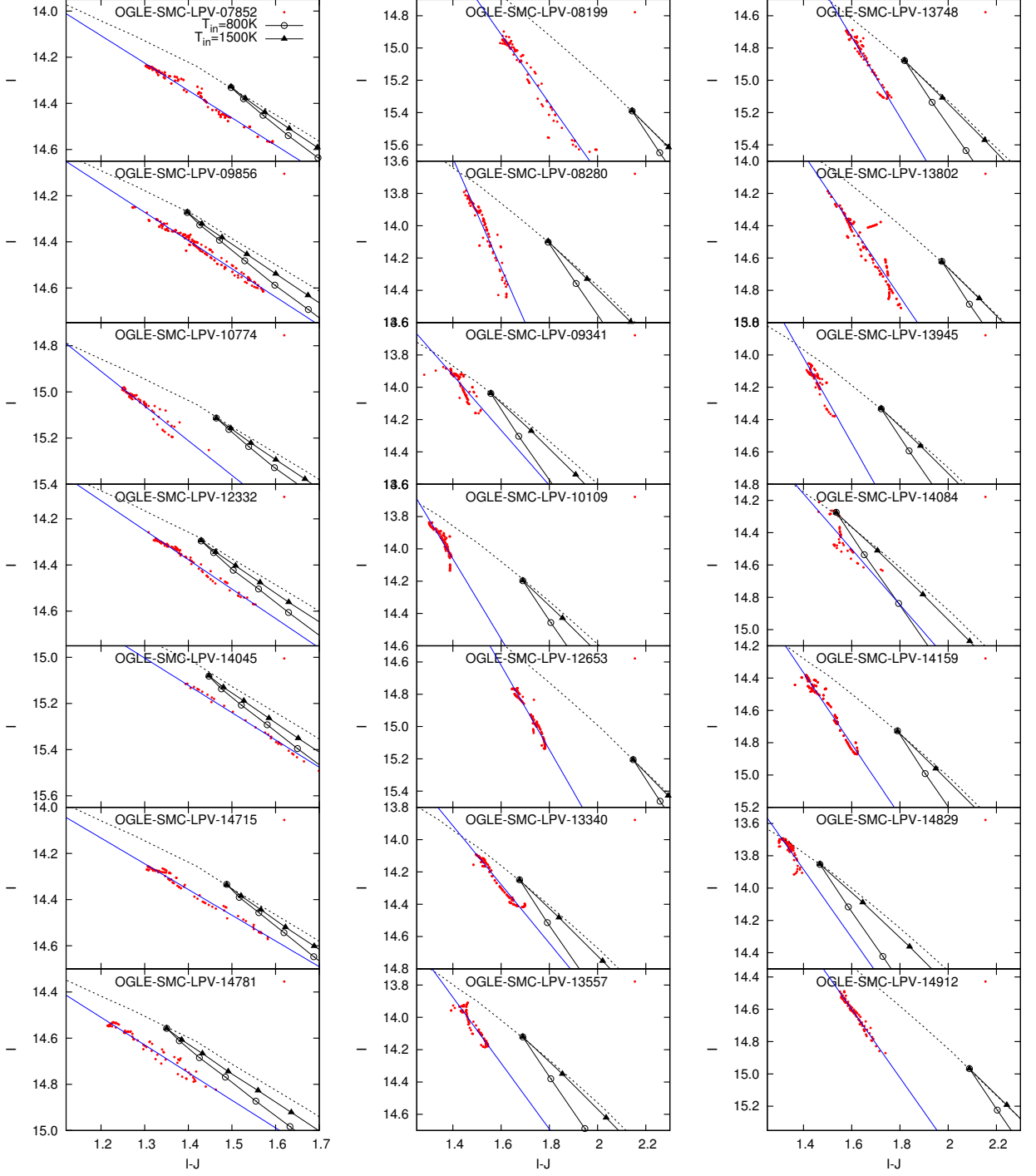


Fig. 21.— Comparisons of observations with models of expansion velocity 15 km s^{-1} . The 7 panels of the left-hand column represent the I and $I - J$ variations for the oxygen-rich stars and the 14 panels of the middle and right-hand columns are for the carbon stars (see text). The black continuous lines with open circles show the magnitude and colour variations for models with an inner dust shell temperature of 800 K while the triangles are for models with an inner dust shell temperature of 1500 K. The top end of each curve corresponds to shell optical depth $\tau_V = 0$ and the points are spaced at intervals of 0.5 in $\tau_V = 0$. The black dotted lines show the locus of un-extincted blackbodies of different temperatures and the constant luminosity given in Table 2 for each star. Note that the scale of the vertical axis is the same for all oxygen-rich stars and for all carbon stars.

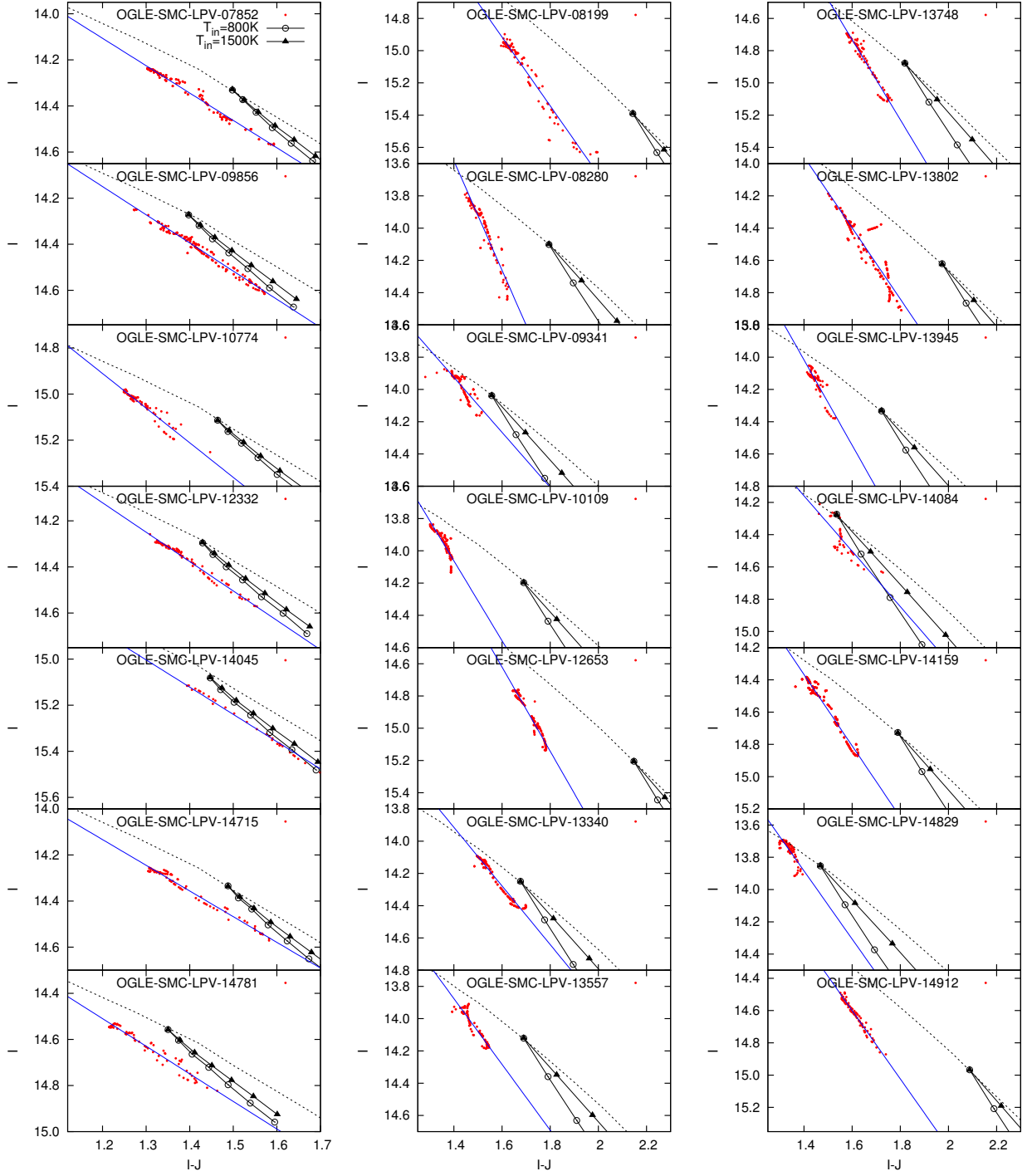


Fig. 22.— The same as Figure 21 but for models with an expansion velocity of 220 km s^{-1} .

should be one of J , H or K_s because of the higher frequency of observation compared to V . Ideally, $I - K_s$ would be best because of the large wavelength range spanned by this colour, but as we will show below, the K_s band in O-rich stars is contaminated by variable H_2O absorption, as is the H band, so we use $I - J$ as the colour in our first comparison of observations and models.

In Figures 21 and 22 we show the I magnitude plotted against the $I - J$ colour for the observed samples of oxygen-rich and carbon stars. The red points show the LSP variations obtained from Fourier fits to the observed light curves. The blue lines show least-squares fits to these points (the line is omitted if the relative error in the slope is more than 0.2). Figure 21 displays models with a shell expansion velocity of 15 km s^{-1} (thin shell) while Figure 22 displays models with a shell expansion velocity of 220 km s^{-1} (thick shell). Note that it is not the absolute values of points in the diagrams that is important, it is the slope of the line representing the variation of I with $I - J$ that matters. If the LSP variations are caused by variable amounts of circumstellar dust alone, then the slope will depend almost entirely on the dust properties and not on the spectrum of the central star. The central star, which in these models we assume to emit as a blackbody with the L and T_{BB} given in Table 2, determines the position of the model in Figures 21 and 22 when there is no circumstellar extinction.

First, we make some comments on the models. In both Figures 21 and 22, the two model lines differ slightly due to re-emission from the dust shell at J and to a lesser extent I . Comparing Figure 21 with Figure 22, corresponding to models with different dust shell thickness, we see that there is a slightly faster increase in $I - J$ with I for the thinner shell of Figure 21, especially for the hotter inner dust shell temperature of 1500 K . The reason for this is that for the thinner dust shell there is more emission at J . Also, for a given optical depth τ_V to the centre of the disk of the observed star, the total extinction averaged over the stellar disk is slightly greater for the thinner shell in Figure 21 than for the thicker shell in Figure 22 (the lines in Figure 21 are longer than in Figure 22). This is because the extinction near the limb of the disk is smaller relative to the extinction at the centre of the disk for a thicker shell.

The observed variation of I with $I - J$ associated with the LSP (red points) is generally consistent with the slope of one of the model lines in Figures 21 or 22. This indicates that the variation of I and J due to an LSP could be explained by variable dust absorption alone.

8.2.2. The variation of I with $J - K_s$

Figures 23 and 24 show the variation of I with $J - K_s$. As one can easily see, the observational variations due to the LSPs are inconsistent with the model variations in all cases. Most importantly, for the O-rich stars, the observed $J - K_s$ colour tends to get *bluer as the star gets fainter in I* . There is no way that such variations can be the result of variable amounts of dust extinction only.

The most probable explanation for the variation of $J - K_s$ in O-rich LSP stars is strong H_2O absorption in K_s band. Significant broad H_2O band absorption is found between about 1.4 and

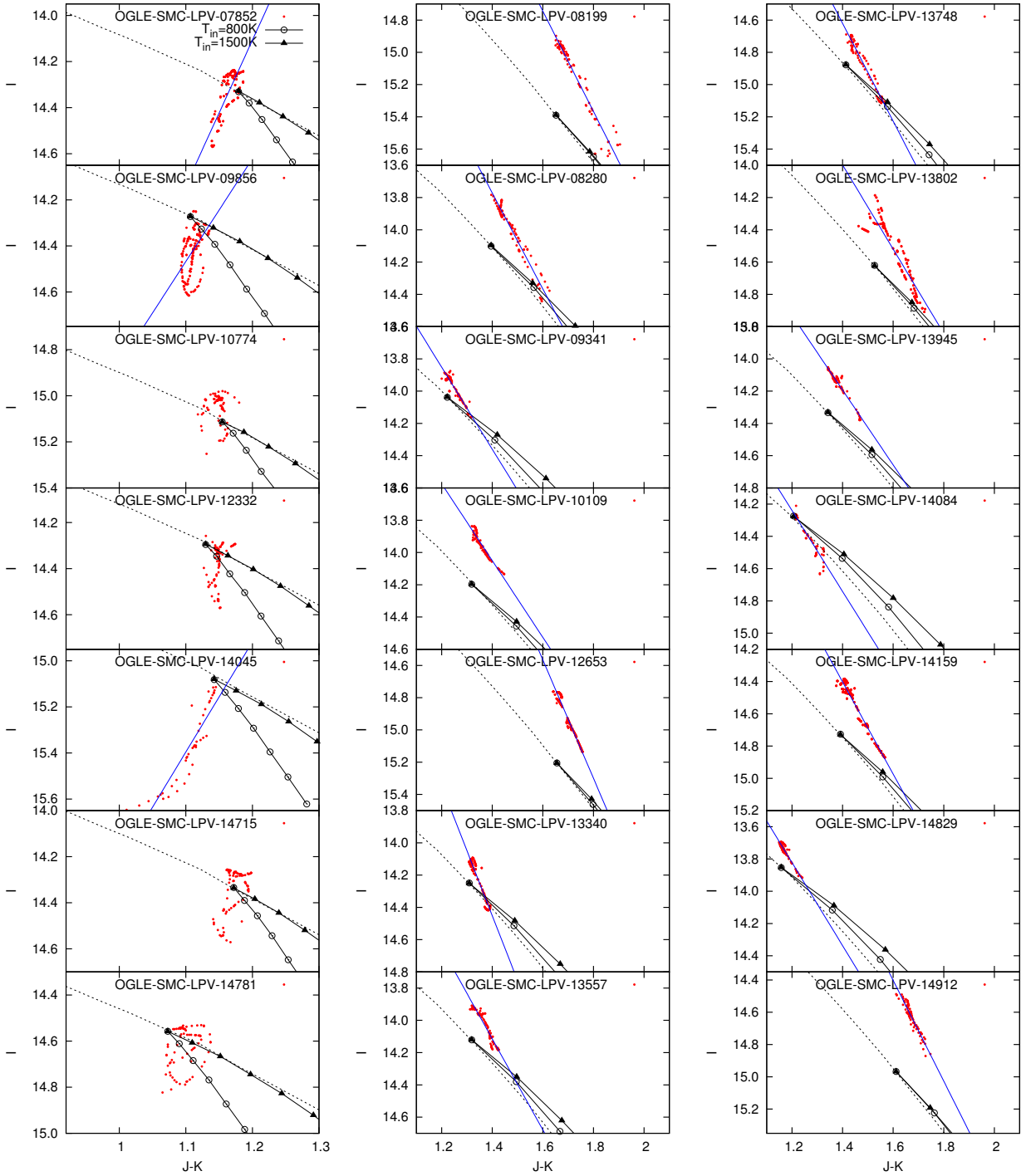


Fig. 23.— The same as Figure 21 but using the $J - K_s$ colour rather than $I - J$.

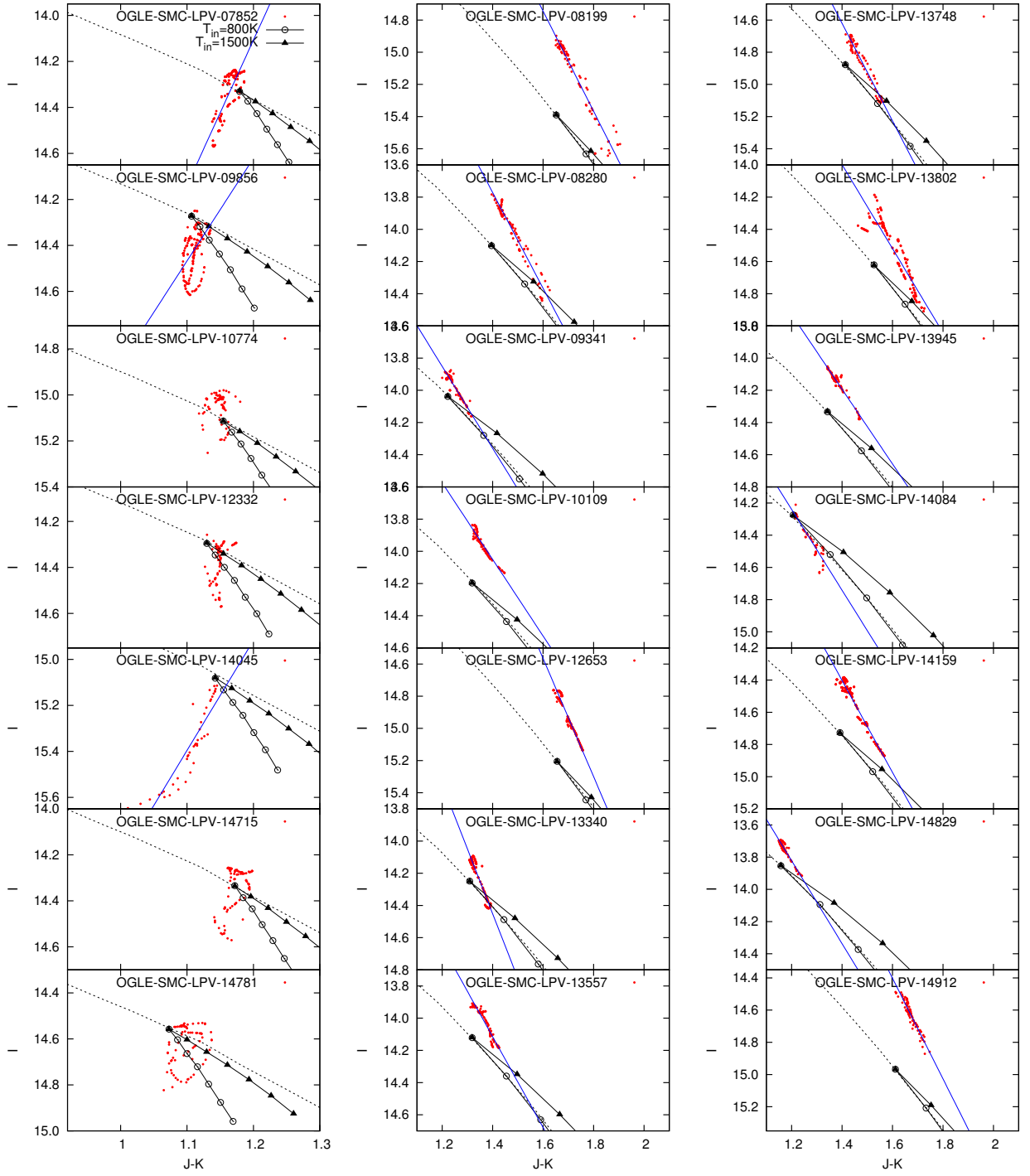


Fig. 24.— The same as Figure 22 but using the $J - K_s$ colour rather than $I - J$.

$1.9\mu\text{m}$ on the edges of the H and K_s filter bandpasses. In non-variable stars, this absorption is seen from about M6 III to later spectral type in M giants (e.g. [Tsuji 2000](#); [Rayner et al. 2009](#)). Strong water absorption in the H and K_s bands is also commonly seen in large amplitude pulsating red giants (Mira variables; e.g. [Johnson & Méndez 1970](#)). The reason for this absorption is the existence of a relatively dense shell with a temperature of about 1800 K elevated above the photosphere by shock waves associated with the pulsation ([Ireland, Scholz, & Wood 2011](#)). Using the models atmosphere results of [Houdashelt et al. \(2000\)](#), we find that the $V - I$ colours of the stars we are examining here yield $T_{\text{eff}} \sim 3400\text{--}3600\text{ K}$, corresponding to spectral types M3–M5. Due to these relatively early M spectral types, the results noted above mean that strong water absorption in the K_s band cannot occur in a hydrostatic atmosphere. The elevation of a shell of mass above the photosphere is required to produce strong water absorption, as in the case of Mira variables. We suggest that this shell elevation, which may also lead to dust formation, occurs at the beginning of the luminosity declines associated with the LSPs, leading to the formation of increasing H_2O absorption in the K_s band and blueing of the $J - K_s$ colour.

This result is a second piece of observational evidence for the existence of a disturbance above the photosphere caused by the LSP. [Wood et al. \(2004\)](#) found variable $\text{H}\alpha$ absorption in stars with LSPs which they attribute to a chromosphere of variable strength, with the strongest $\text{H}\alpha$ absorption near maximum light. Combined with the results above for the H_2O absorption layer, we have a picture whereby matter is ejected above the photosphere beginning near the luminosity decline of the LSP forming a relatively dense shell of temperature $\sim 1800\text{ K}$. As the LSP cycle progresses, this shell appears to be slowly heated by non-thermal processes to $\sim 8000\text{ K}$ giving rise to a chromosphere which is then displaced by the next ejected shell containing H_2O .

Turning to the carbon stars, we see that they do get redder as they get fainter in I but in all cases they clearly do not redden as much as predicted by the models. To bring the observed variation in $J - K_s$ with decline in I into agreement with the models, while keeping the variation of $I - J$ with I in agreement with the models, would require a strange dust opacity with a large bump in the K_s band. We do not know of any dust composition that could produce such a bump (see Section 8.2.4 for a discussion of the effect of different grain opacities).

We note that ejected clouds covering only part of the stellar surface rather than the complete surface as for spherical shells cannot explain the observed variation in $J - K_s$ with declining I . For all but very large optical depths, the $J - K_s$ colour in a cloud model increases slightly faster with decline in I than for a spherical shell model, whereas the observations require a slower increase in $J - K_s$ colour. Also, given that the variation of the observed $I - J$ colour with decline in I agrees with the spherical shell models, a cloud model will not agree with the observations (the $V - I$ colour in the cloud model increases more slowly with decline in I than in the spherical shell model).

In summary, our conclusion from examining the variations of LSP stars in the $(I, J - K_s)$ plane is that, for both O-rich and C-rich stars, a model involving only variable dust extinction is not viable as an explanation for LSP behaviour.

8.2.3. The variation of I with $V - I$

Although the V observations are not as frequent as observations in other bands, we show the variation of I with $V - I$ for completeness in Figures 25 and 26. For both the V and I bands, re-emission of light absorbed by the shell is weak so the model lines corresponding to the two inner shell temperatures of 800 and 1500 K are close together in both figures.

For most O-rich stars, the observed $V - I$ tend to increase slightly more rapidly with declining I than in the models. For most C-rich stars, the observed and model variations have consistent slopes although for OGLE-SMC-LPV-13557 and OGLE-SMC-LPV-13945 the slopes are different. Overall, the agreement between the observations and dust model predictions is not good in the $(I, V - I)$ plane but the results are not definitive.

8.2.4. Testing different dust grains

Different dust grains have different absorption and scattering coefficients. Thus we tried changing the dust grain composition to see if this would give agreement between the light variations in the dust shell model and the observed light variations, especially in the I and $J - K_s$ plane for the carbon stars. We examined four dust grain types available in DUSTY (see Table 3) for oxygen-rich stars and for carbon stars, including the grain types we used in Section 8.1. The thin dust shell model with an expansion velocity of 15 km s^{-1} was adopted.

Figure 27 shows comparisons of observed variations in the I and $J - K_s$ diagram with dust shell models for the different grain types. The model slopes for oxygen-rich stars can be changed appreciably by different dust grains but none of the models reproduce the observed slopes. In particular, none of the models can explain the observation that the $J - K_s$ colour get bluer as the star gets fainter in I . Turning to the carbon stars in Figure 27, we see that changing the grain type in the models changes the slope of the variations but again none of the adopted grain types can consistently reproduce the observed slope.

The relations between the colors and I magnitude variations for the program stars have been derived from least square fits (cf. blue lines in Figures 21, 23, and 25). Figures 28 and 29 show comparisons of the mean values of the fitted observed line slopes in the $(I, V - I)$, $(I, I - J)$, and $(I, J - K_s)$ diagrams with dust shell models for the different dust grain types for the oxygen-rich stars and the carbon stars, respectively. The black dots with bars indicate the mean values of the observed line slopes for the stars with a relative error in the slope of less than 0.2 and its standard deviation. The colored dots and bars in each panel of Figures 28 and 29 show the mean values of the model slopes and its standard deviations for the different dust temperatures. The slope of the model curve on the color-magnitude diagram slightly varies with the colour (see e.g. Figure 21). To determine the model slope, we calculate the slope of the straight line which connect two points corresponding to the optical depths τ_V of 0 and $\tau_{V,\text{max}}$ on the color-magnitude diagram. We choose

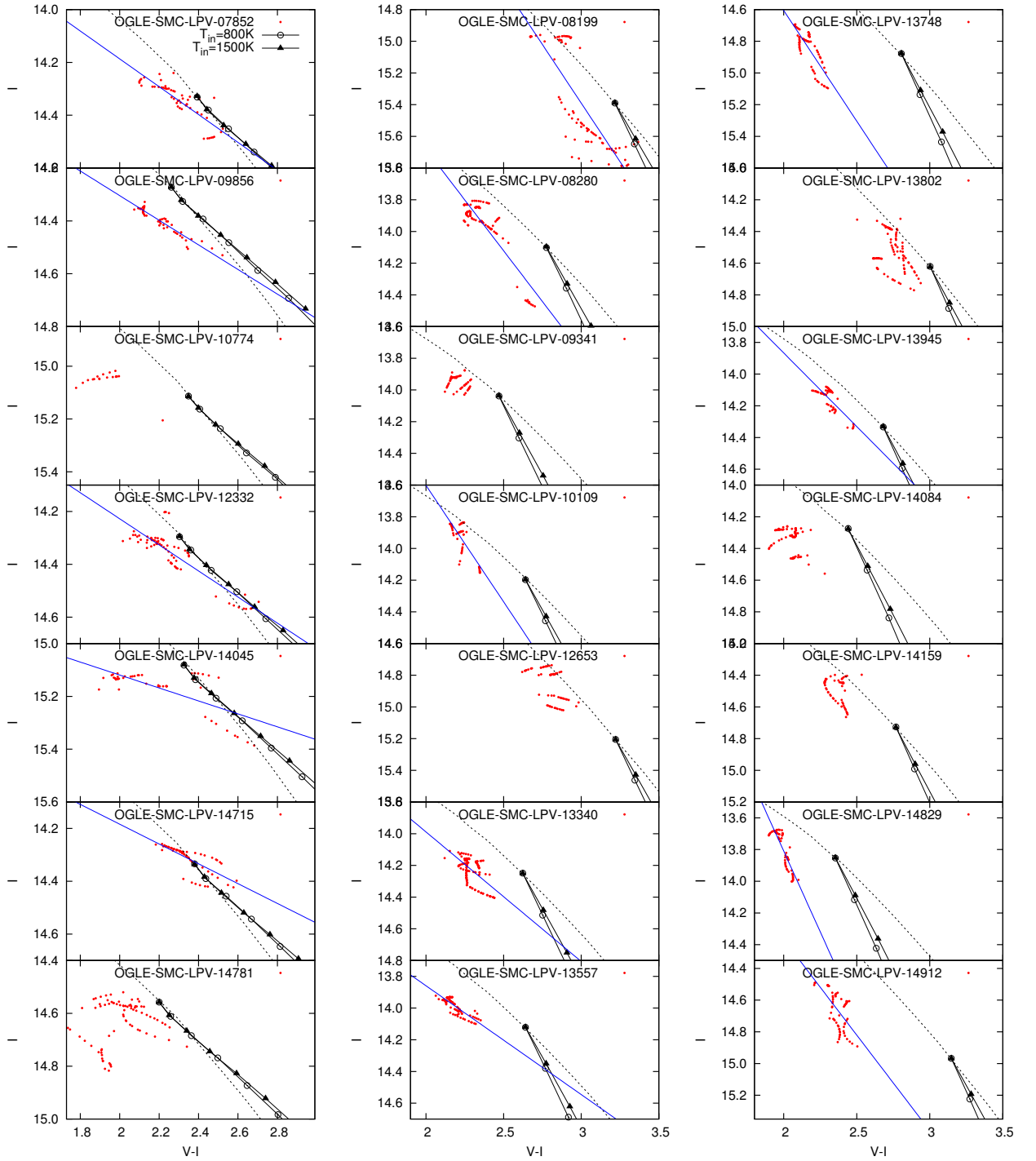


Fig. 25.— The same as Figure 21 but using the $V - I$ colour rather than $I - J$.

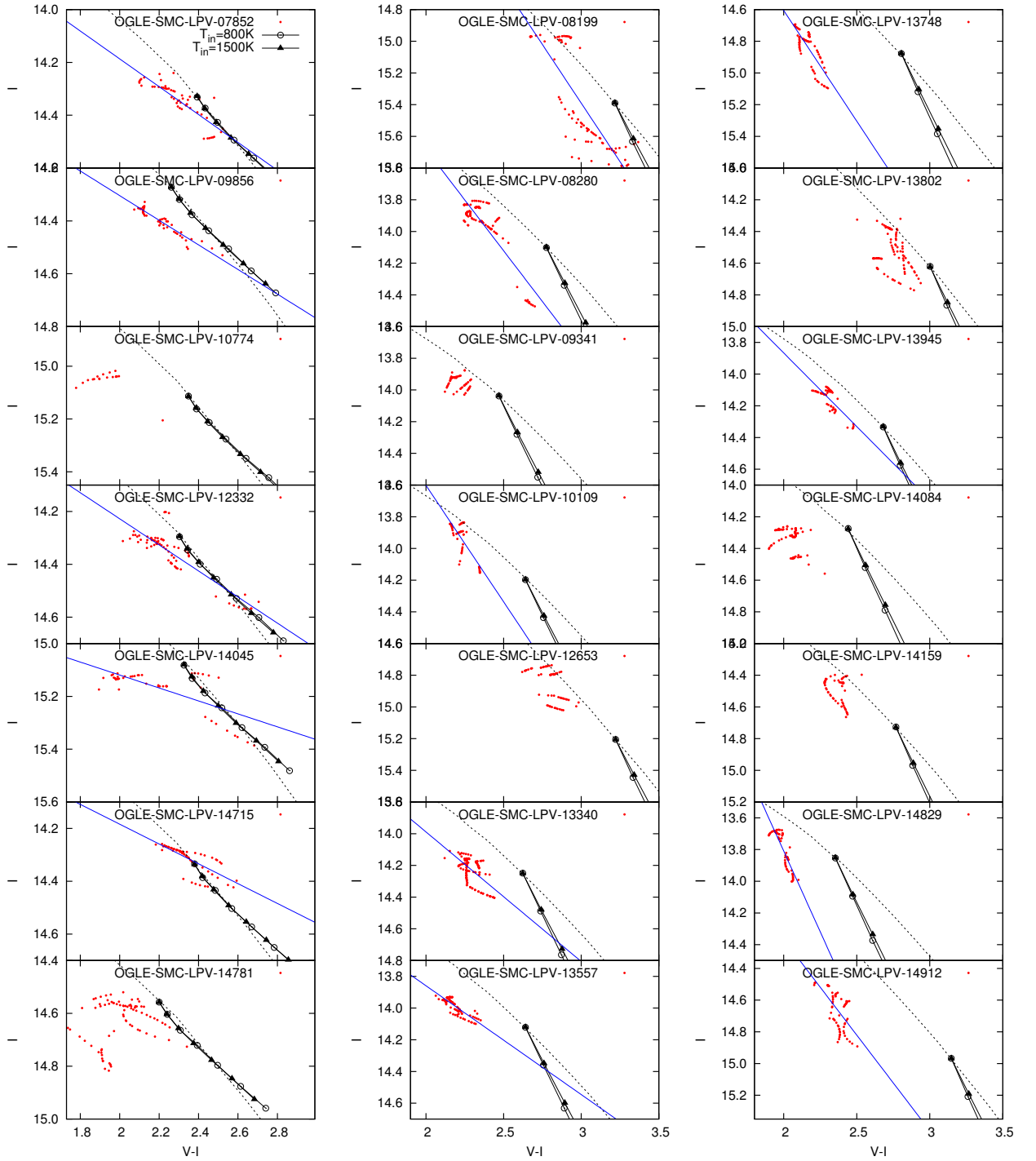


Fig. 26.— The same as Figure 22 but using the $V-I$ colour rather than $I-J$.

$\tau_{V,\max}=2$ and $\tau_{V,\max}=0.5$ for the oxygen-rich stars and the carbon stars, respectively, to reproduce the mean value of the observed I amplitudes, which is ~ 0.23 [mag] for the oxygen-rich stars, and which is ~ 0.32 [mag] for the carbon stars.

In Figure 28, the models 0, 1, and 3 agree with the observation in the $V - I$ and $J - K_s$ colours. However, as mentioned above, none of the models can reproduce the observation in the $J - K_s$ colour. We can see very small standard deviations in the model slopes. Thus the variety of the parameters we used for the models could not explain the cause of the disagreement between model and observation. Turning to the carbon stars in Figure 29, we can see larger differences of the model slopes by the different grain types. However none of the program grain types can not explain the observation. These results strengthen the finding of Section 8.2.2 that dust shell models cannot by themselves explain the broad-band light and colour variations in LSP stars.

8.3. The dark spot model

Another possible explanation of the LSP phenomenon is a dark spot on a rotating AGB star. Soszyński & Udalski (2014) noted that the observed light curves of LSP stars are similar to those of the known spotted stars. Moreover, the V to I amplitude ratios of LSP stars and known spotted stars are similar and they are different from the ratios seen in the ellipsoidal binaries of sequence E which lie near the LSP stars in period–luminosity plane. Here we test a simple rotating dark spot model for LSP stars using the latest version of the Wilson–Devinney code (Wilson & Devinney 1971, see Appendix D for the brief introduction) which has the ability to simulate the light curve of a spotted star in a binary system. Since our aim is to examine the light and colour variations due to the appearance of a dark spot on a red giant, our binary systems consist of a rotating red giant star with a circular isothermal spot and a very faint orbiting companion which cannot be seen. Hence, we obtain the light and colour variations due to only the dark spot on the rotating red giant. For the red giant star, we assume a mass of $\sim 1.0M_{\odot}$ and a radius of $\sim 170R_{\odot}$, which gives a surface gravity $\log g$ [cgs] of -0.02 . A metallicity, $\log[\text{Fe}/\text{H}] = -1.0$ and a gravity-darkening coefficient, $g_1=0.32$ (Lucy 1967) are used. For the calculation of oxygen-rich stars, we use the model stellar atmospheres of van Hamme & Wilson (2003) while for carbon stars, a blackbody is used. We note that the model atmospheres do not take into account the effect of the absorption due to H_2O molecules.

The amplitudes of the light variations due to the presence of spots are determined by the spot sizes and the temperature differences between the spots and the normal stellar surface. The temperatures of spots on AGB stars are not known well. For the spot temperature, we follow the work of Soker & Clayton (1999). They initially adopted the solar value of $\frac{2}{3}$ for the ratio of spot to normal photospheric temperature. For an assumed photospheric temperature of 3000 K, the spot temperature would then be 2000 K. Soker & Clayton (1999) then considered a range of spot temperatures from 1600 K (cool spot,) and 2500 K (warm spot) corresponding to a ratio of spot to normal photospheric temperature of 0.533 and 0.833, respectively. To cover a range of spot

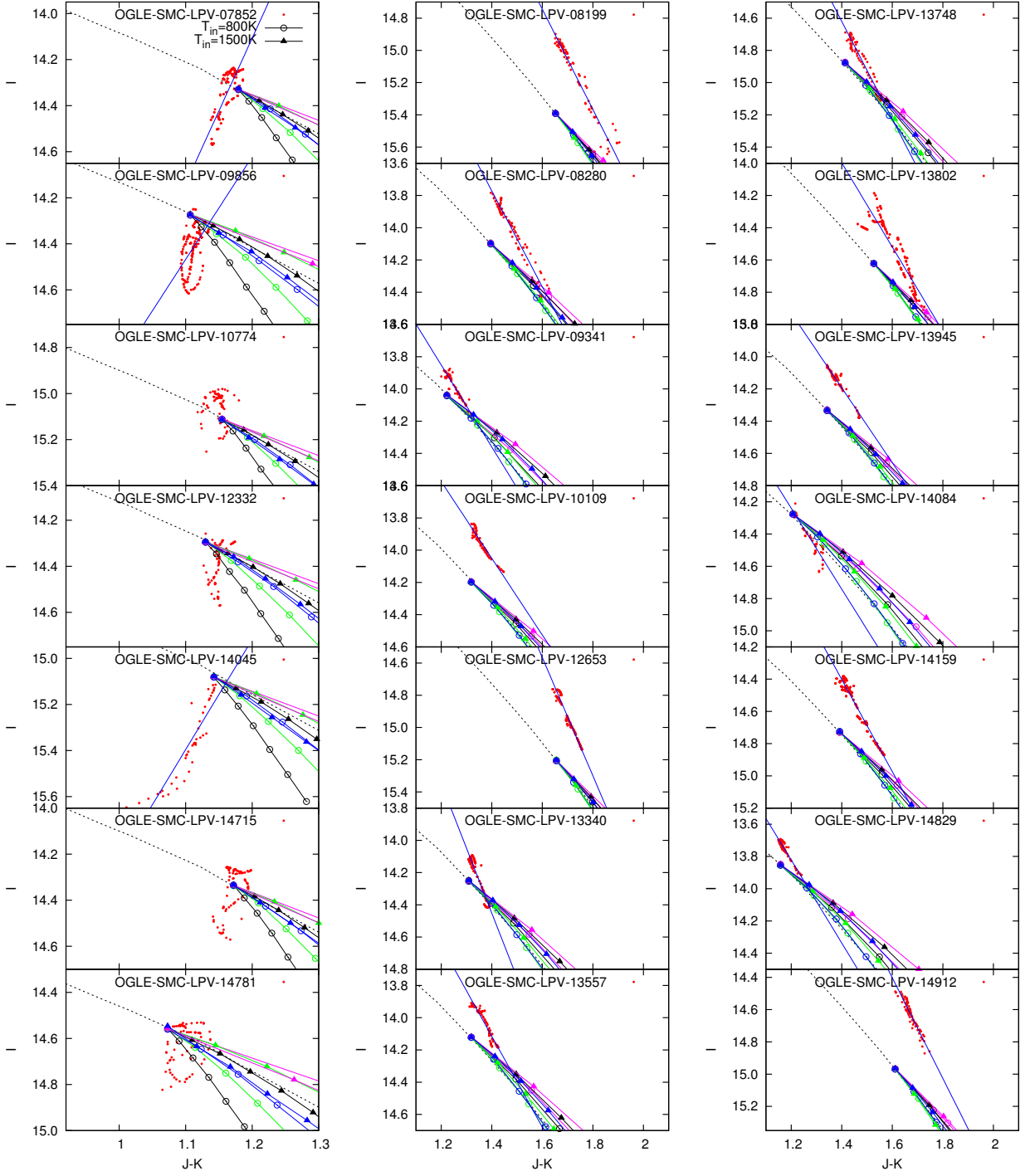


Fig. 27.— The same as Figure 23 but including different dust compositions. For both oxygen-rich and carbon stars, the black solid lines with open circles and filled triangles correspond to the original dust compositions (model 0 in Table 3), while the green, magenta and blue colours correspond to models 1, 2 and 3, respectively.

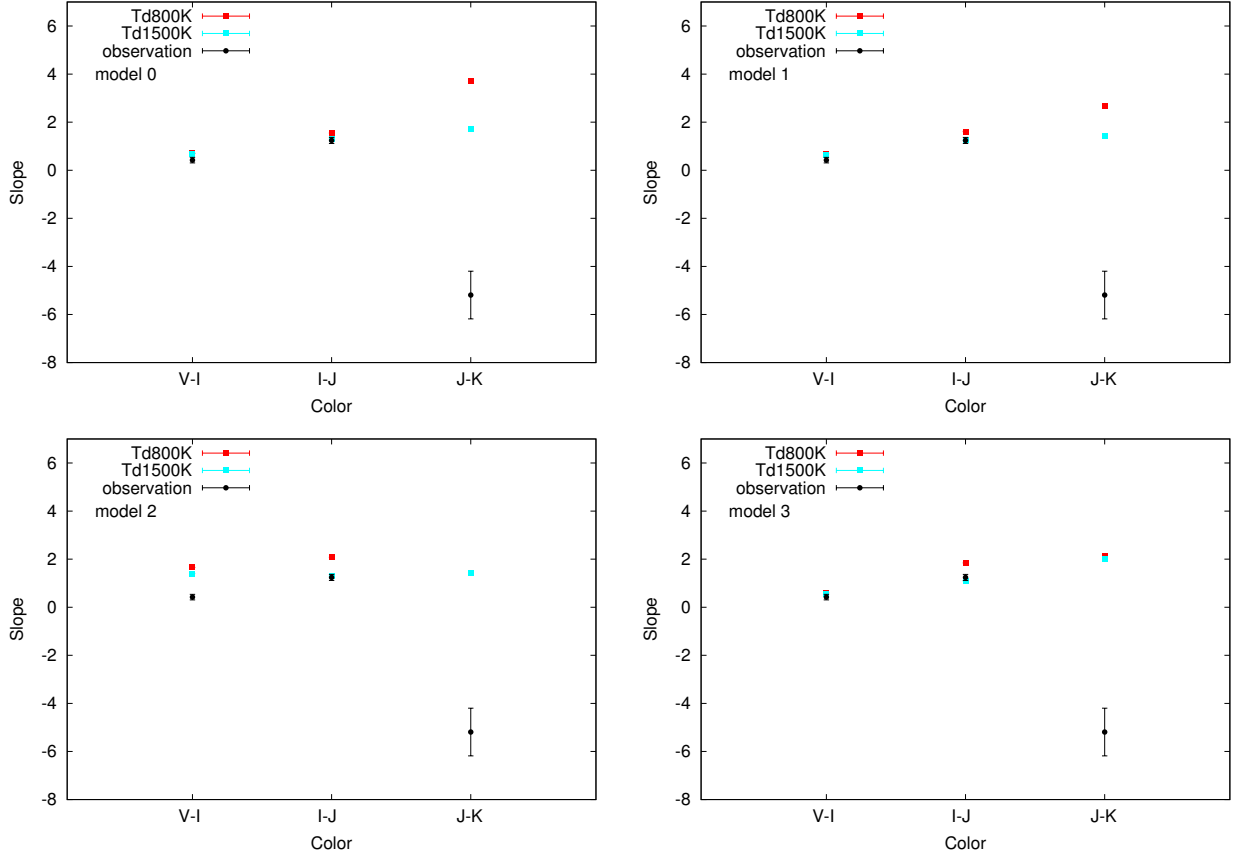


Fig. 28.— Comparisons of the mean observed line slopes in the $(I, V - I)$, $(I, I - J)$, and $(I, J - K_s)$ diagrams for the oxygen-rich stars with dust shell models for the different dust grain types shown in Table 3. The dust grain type adopted for dust shell model is indicated in the top left of a panel. The black dots with bars show the mean value of the fitted observed slopes and its standard deviation while the red and cyan indicate the mean model slopes with dust temperatures $T_d=800$ K and $T_d=1500$ K, respectively.

Table 3: Dust composition

Sp. type	Model name	Composition
O-rich star	model 0	100% ¹ astronomical silicate
	model 1	100% ² warm O-deficient silicate
	model 2	100% ³ FeO
	model 3	100% ⁴ glassy olivine
C-rich star	model 0	50% ⁵ amorphous carbon, 40% ¹ graphite, 10% ⁶ α -SiC
	model 1	100% ¹ graphite
	model 2	100% ⁵ amorphous carbon
	model 3	100% ⁶ α -SiC

Note: ¹Draine & Lee (1984), ²Ossenkopf et al. (1992),
³Henning et al. (1995), ⁴Dorschner et al. (1995), ⁵Hanner
(1988), ⁶Pégouriè (1988)

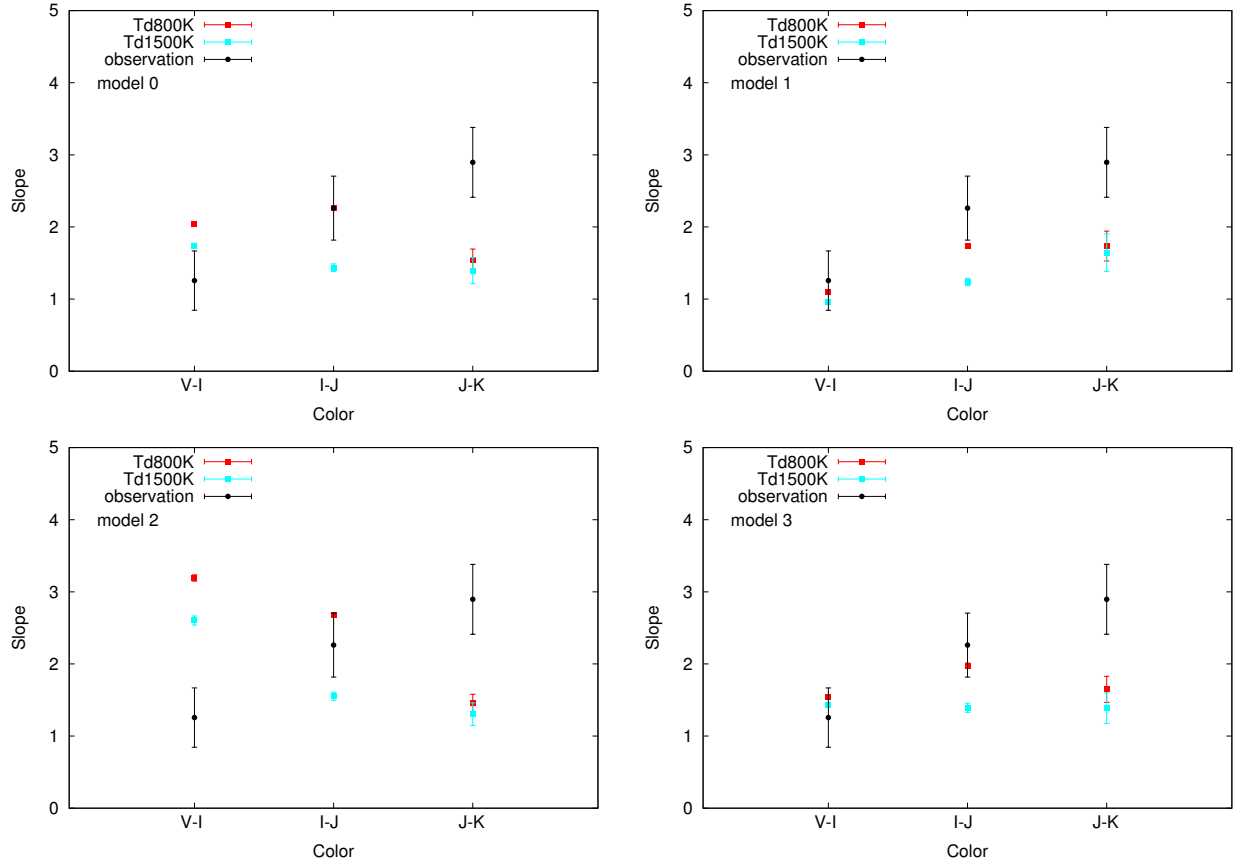


Fig. 29.— The same as Figure 28 but for the carbon stars.

Table 4: Spot temperatures and the spot sizes

Sp. type	Temperature ratio	Spot radius($^{\circ}$)	Model
O-rich star	0.533	35	cool
	0.833	45	warm
	0.913	90	hemisphere
C-rich star	0.533	40	cool
	0.833	50	warm
	0.888	90	hemisphere

Note: Spot radius is defined as the angle when viewed from the stellar centre.

temperatures, we also make models with these two temperature ratios. We use these models to simulate each of the stars in Table 2 and we use the effective temperatures T_{eff} in Table 2 as the temperature of the normal photospheric regions.

The spot sizes for the two temperature cases are fixed by requiring that the amplitude in the I band is similar to the observed largest amplitudes, which are ~ 0.5 mag for the oxygen-rich stars and ~ 0.7 mag for the carbon stars. Table 4 gives the parameters of our spot models. It has been assumed that the inclination of the model rotation axis is 90 deg to the line of sight and the centre of the spot is on the equator of the star.

The spot model also effectively simulates light variations caused by the giant convective cells which were proposed by [Stothers \(2010\)](#) to explain LSPs in AGB stars. In this model, the light variations are caused by the turnover of cooler and hotter giant convective cells at the stellar surface. To simulate this situation, we examine a model where the rotating dark spot covers a full hemisphere of the star (hereinafter, the hemisphere model). To reproduce the observed largest amplitudes in I band, we use the temperature ratios of the spot area to the normal area given by Table 4. As in the case of the other spot models, we use the effective temperatures T_{eff} given in Table 2 for the temperature of the normal photospheric regions in both oxygen-rich and carbon stars.

8.4. Comparison of the spot model with observations

8.4.1. The variation of I with colours

In Figures 30, 31 and 32 we show the I magnitude plotted against the colours $I - J$, $J - K_s$ and $V - I$, respectively, for the observed samples of oxygen-rich and carbon stars. The magnitudes of models at the maximum light, which corresponds to when there is no visible spot, are adjusted in the plots to the magnitudes at the observed maximum light for each star.

As with our comparison of dust shell models with observations, we test the spot models by looking for differences in the slopes in (I, colour) diagrams of model lines and observational variations. Models with different ratios of the spot to normal photospheric temperature show different slopes. The models with higher spot temperature (i.e. larger temperature ratio) show shallower slopes.

For carbon stars, the slope of the line representing the observations generally shows a good agreement with the model lines in each of Figures 30, 31 and 32 (two exceptions are OGLE-SMC-LPV-13557 and OGLE-SMC-LPV-13945 in Figure 32 which show disagreement with their models). According to the figures, the models with hotter spots (temperature ratio 0.833) and the hemisphere models (which also have a temperature ratio of 0.888) fit the models better in each of the $(I, I - J)$, $(I, J - K_s)$ and $(I, V - I)$ diagrams. If sequence D light variations are due to rotating spots, these results suggest that the spot temperatures in carbon stars should be roughly 2500 K.

In distinct contrast to the carbon stars, the oxygen-rich star variations do not agree with model variations in any of the $(I, I - J)$, $(I, J - K_s)$ or $(I, V - I)$ diagrams. Although agreement would not be expected in the $(I, J - K_s)$ plane where the observations are affected by absorptions due to H_2O molecules, the bad disagreement in the $(I, I - J)$ and $(I, V - I)$ diagrams indicates that spot models cannot explain the light and colour variations due to the LSP phenomenon in oxygen-rich stars. Since the LSPs of both oxygen-rich stars and carbon stars should have the same origin, the failure of the spot models to reproduce the observations in oxygen-rich stars means that spots are not a reasonable explanation for LSPs in sequence D stars. This result agrees with the conclusion of [Olivier & Wood \(2003\)](#) that the rotation periods of LSP stars are too long for a spotted star model to explain LSP variations.

8.4.2. *The effect on spot models of the inclination of the rotation axis and the spot latitude*

The models above were made assuming spots on the equator of a rotating star whose rotation axis is perpendicular to the line of sight. Changing the latitude of a spot will reduce its apparent area and hence the amplitude of the light variation it will cause. However, the slope of the locus of colour–magnitude variation should be unchanged since the reduction in apparent area also occurs as a spot on the equator rotates towards the limb of the star (the very minor effect of limb darkening will produce very small differences between the two cases). The same argument applies in the case of a star with a tilted rotation axis. We thus expect the results of the previous section to apply regardless of the inclination of the rotation axis and the latitude of the spots. As a test calculation, we examined the change in the I and $I - J$ magnitudes for a star with the rotation axis tilted at 30, 60 and 90 deg. The results are shown in Figure 33. It can be seen that the slope of the variation is the same in all cases.

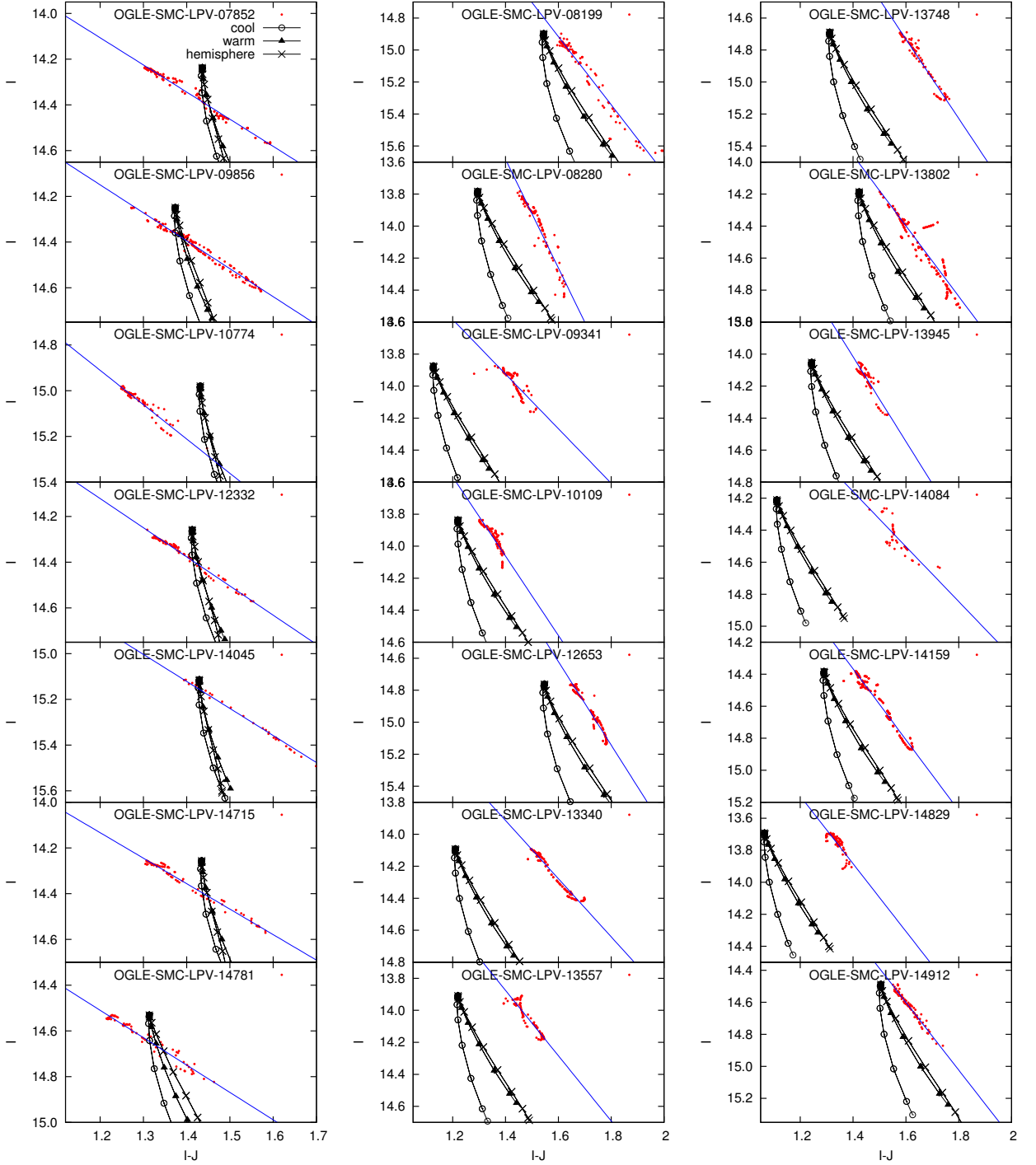


Fig. 30.— Comparisons of observations with dark spot models in the $(I, I - J)$ plane. The 7 panels of the left-hand column show oxygen-rich stars and the 14 panels of middle and right-hand columns show carbon stars. Red points and blue lines represent observations, as in Figure 21. The black lines with open circles and the lines with filled triangles show the magnitude and colour variations for models with cool and warm spot temperatures, respectively, while the lines with crosses are for models with a hemisphere spot.

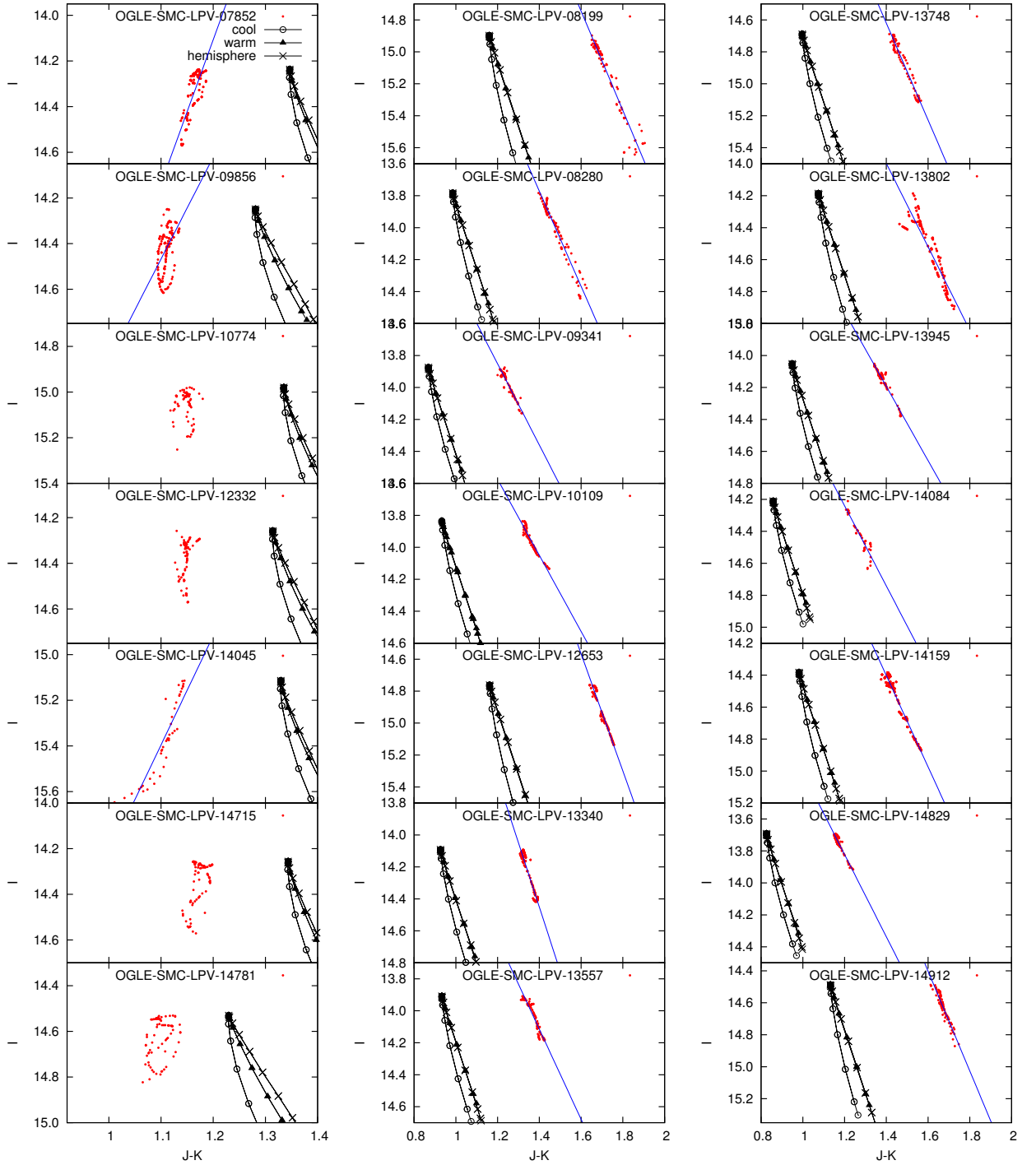


Fig. 31.— The same as Figure 30 but using the $J - K_s$ colour rather than $I - J$.

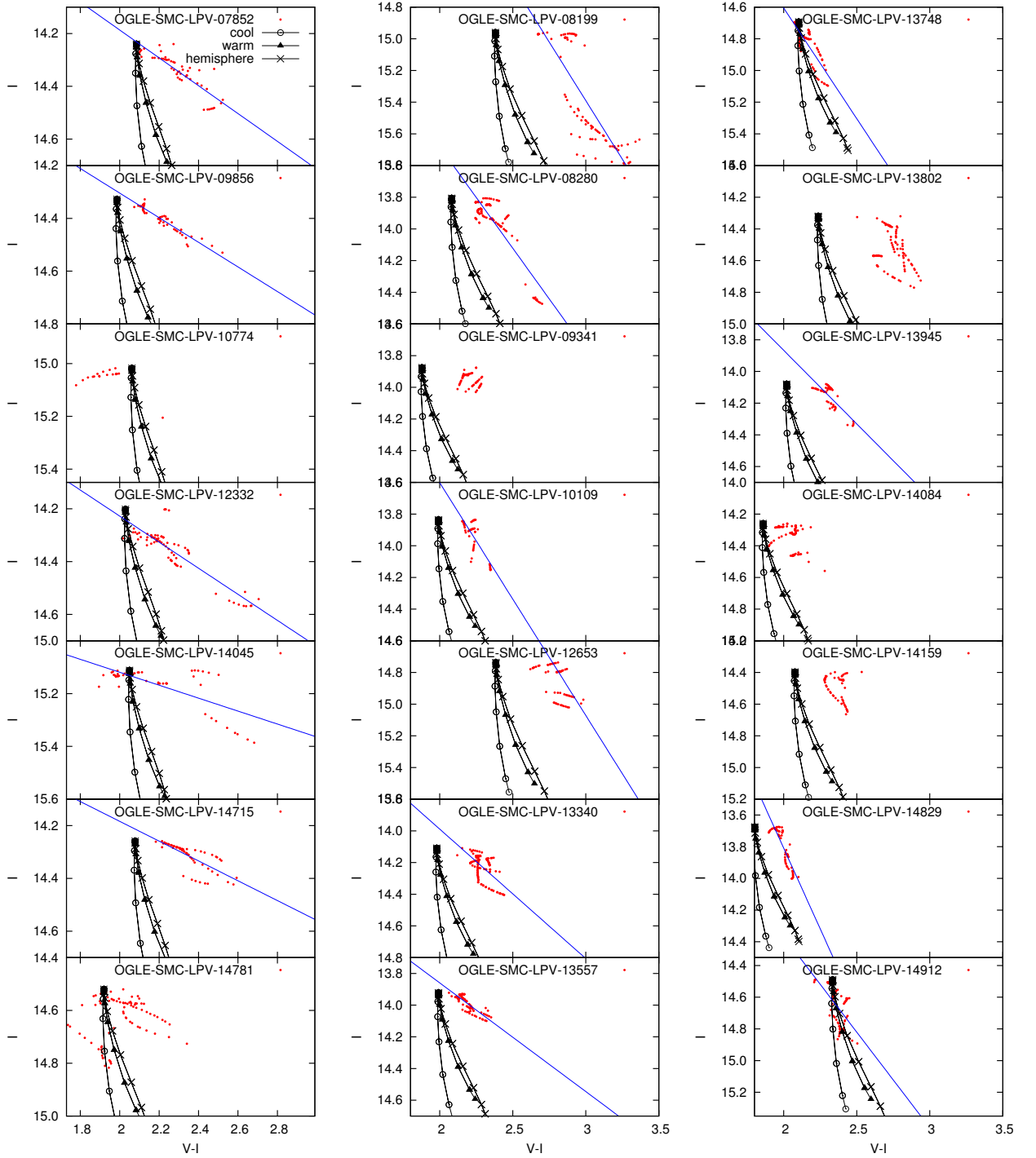


Fig. 32.— The same as Figure 30 but using the $V - I$ colour rather than $I - J$.

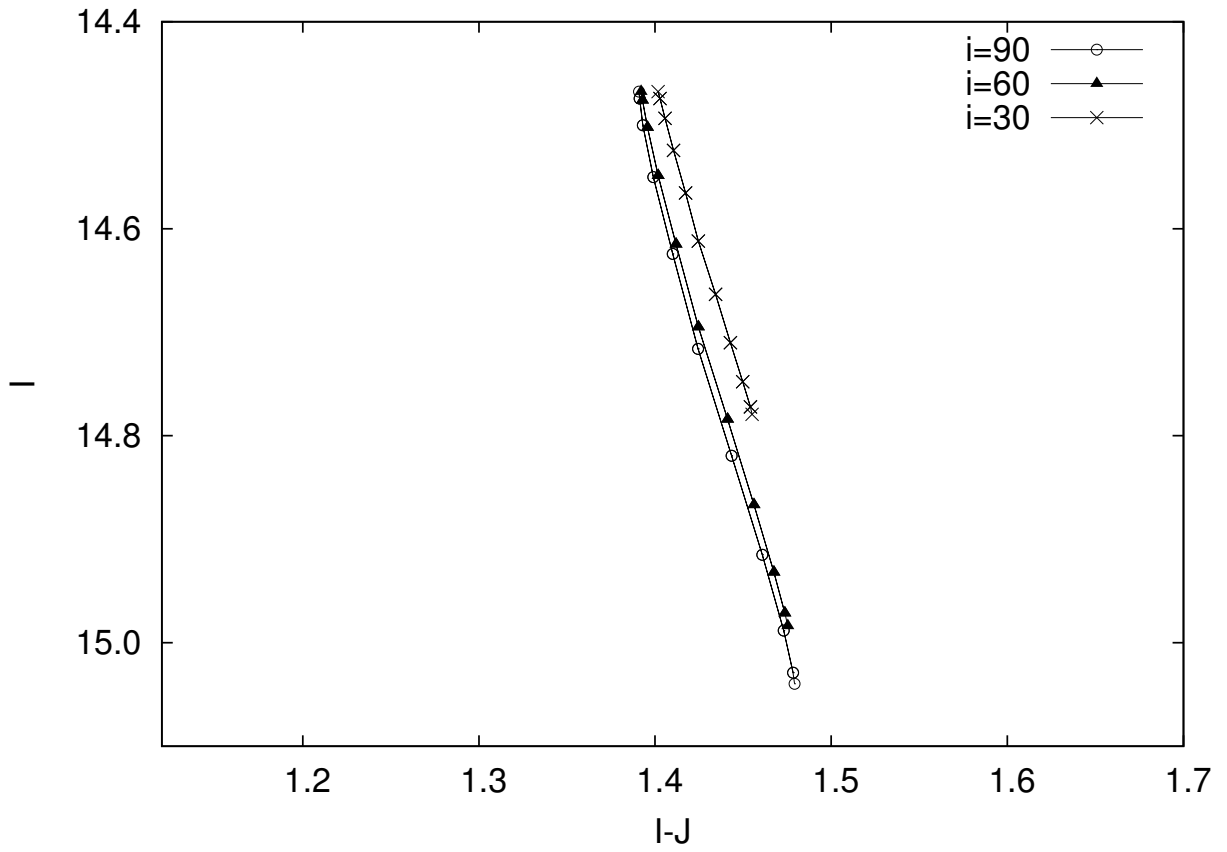


Fig. 33.— The variation of I with $I - J$ in hemisphere spot models for oxygen-rich stars when different inclination angles for the rotation axis are assumed.

Table 5: ΔT_{eff} and $\tau_{V,0}$ for models

Sp. type	$T_{\text{eff},0}(\text{K})$	$\Delta T_{\text{eff}}(\text{K})$	$\tau_{V,0}$	Model
O-rich star	2800	100	1	model0
	2800	50	2	model1
C-rich star	2500	100	0.5	model2
	2500	50	1	model3

8.5. The combined dust model with dark spot

In Section 8.2 we examined the possibility that a dust shell model alone could explain the LSP phenomenon and rejected. Similarly, in Section 8.4 we examined if a rotating spotted star could explain the light and colour variations of the LSPs and rejected. In a dust shell model we implicitly assumed that the luminosity emitted from a central star does not change at all. However it is likely that a mass ejection process which can induce supply of dust into circumstellar space correlates with change of luminosity which red giant emits. Cuntz (1990) argued the possibility of mass ejection in red giant stars which could be induced by propagation of shock waves. The brief scenario of this is that acoustic waves in late-type giant star due to the motion of convection eddies induce mass loss by propagation of shock waves in the stellar atmosphere. If giant convective cell as Stothers (2010) proposed, which could induce the presence of a dark spot in the stellar surface, moves within the convective zone in a red giant star, acoustic waves might be generated and lead to mass ejection which could cause dust formation in the circumstellar space. Hence the light and colour variations are expected to be induced due to both the presence of a spot and dust absorption. Similar light and colour variation is induced by circumstellar dust absorption around a rotating star with dark spots. Here we examine the possibility that a combination of a rotating spotted star and dust absorption at certain phases of the rotation could reproduce the observed light and colour variations in stars with LSPs.

In this combined model, the effective temperature of the central star is assumed to vary sinusoidally to simulate a rotating spotted star and the optical depth of the dust shell is assumed to vary sinusoidally to simulate periodic dust absorption. The following equations are used:

$$T_{\text{eff}}(\phi) = T_{\text{eff},0} + \Delta T_{\text{eff}} \sin(2\pi\phi + \beta) \quad (8.9)$$

$$\tau_V(\phi) = \tau_{V,0} \sin(\pi\phi) \quad (8.10)$$

where ΔT_{eff} and $\tau_{V,0}$ are the amplitudes of variation of the effective temperature and optical depth of a dust shell in V of the dust shell, respectively. $T_{\text{eff},0}$ is the average effective temperature. As a direct consequence of these equations, the central star luminosity is given by

$$L(\phi) = \frac{T_{\text{eff}}^4(\phi)}{T_{\text{eff},0}^4} L_0 \quad (8.11)$$

where L_0 are the average luminosity. The fluxes emitted by the central star in the various photometric bands were obtained assuming the central star was a blackbody. The dust absorption in photometric bands other than V was obtained using DUSTY. The dust compositions used in Section 8.1 for oxygen-rich and carbon-rich stars was adopted and the shell outer radius was set to 1.5 times the inner radius, which roughly corresponds to the models described above with an expansion velocity of 15 km s^{-1} . The inner dust shell temperature was set to 800 K.

In the combined model, ϕ varies from 0 to 1 as the spotted star makes one complete rotation. The phase shift β between the rotation phase and dust absorption phase has been introduced to allow for dust absorption at different possible rotation phases. Since we do not know how dust absorption might be linked to the rotation phase, models were made with different values for β . Note that the dust absorption goes through one maximum as the star makes a full rotation.

Table 5 gives the parameters considered for the models described here. Two values of ΔT_{eff} , 50 and 100 K, were used for both oxygen-rich and carbon-rich stars. The values of $\tau_{V,0}$ were adjusted so that the variations in magnitude caused by dust dominated for the models with $\Delta T_{\text{eff}} = 50 \text{ K}$ while the variations in magnitude caused by T_{eff} variations dominated when $\Delta T_{\text{eff}} = 100 \text{ K}$.

Figure 34 shows the I magnitude plotted against $V - I$, $I - J$ and $J - K_s$ for the various models computed here. In general, the slopes of the variations in the (I, colour) diagrams for the combined models lie between the slopes for pure dust absorption and pure T_{eff} variations (spot model). The combined models do not generally represent an improvement over the pure dust or spot models. In particular, they cannot explain the observation that $J - K_s$ in oxygen-rich stars get bluer as the star dims.

9. Summary

We have examined broad-band observations of samples of oxygen-rich and carbon stars in the SMC which exhibit LSP light variations. The observations are in the $VIJHK_s$ bands and they were obtained by the OGLE project and by the SIRIUS camera of the IRSF 1.4m telescope.

The J and K_s observations of oxygen-rich stars reveal a significant new feature of LSP light variations. As light declines, the $J - K_s$ colour barely changes or sometimes gets bluer. We interpret this as indicating that cool gas containing a significant amount of H_2O is levitated above the photosphere of LSP stars at the beginning of light decline. Absorption of light in the K_s band by H_2O forces the $J - K_s$ colour to remain constant or to get bluer during light decline. The levitation of matter above the photosphere found here, along with the discovery of the development of a warm chromosphere during rising light by Wood et al. (2004), provides strong evidence that the LSP phenomenon is associated with mass ejection from the photosphere of red giant stars.

We examined two possible models for the explanation of the LSP phenomenon by comparing these models with broad-band observations of both oxygen-rich and carbon stars. The first model

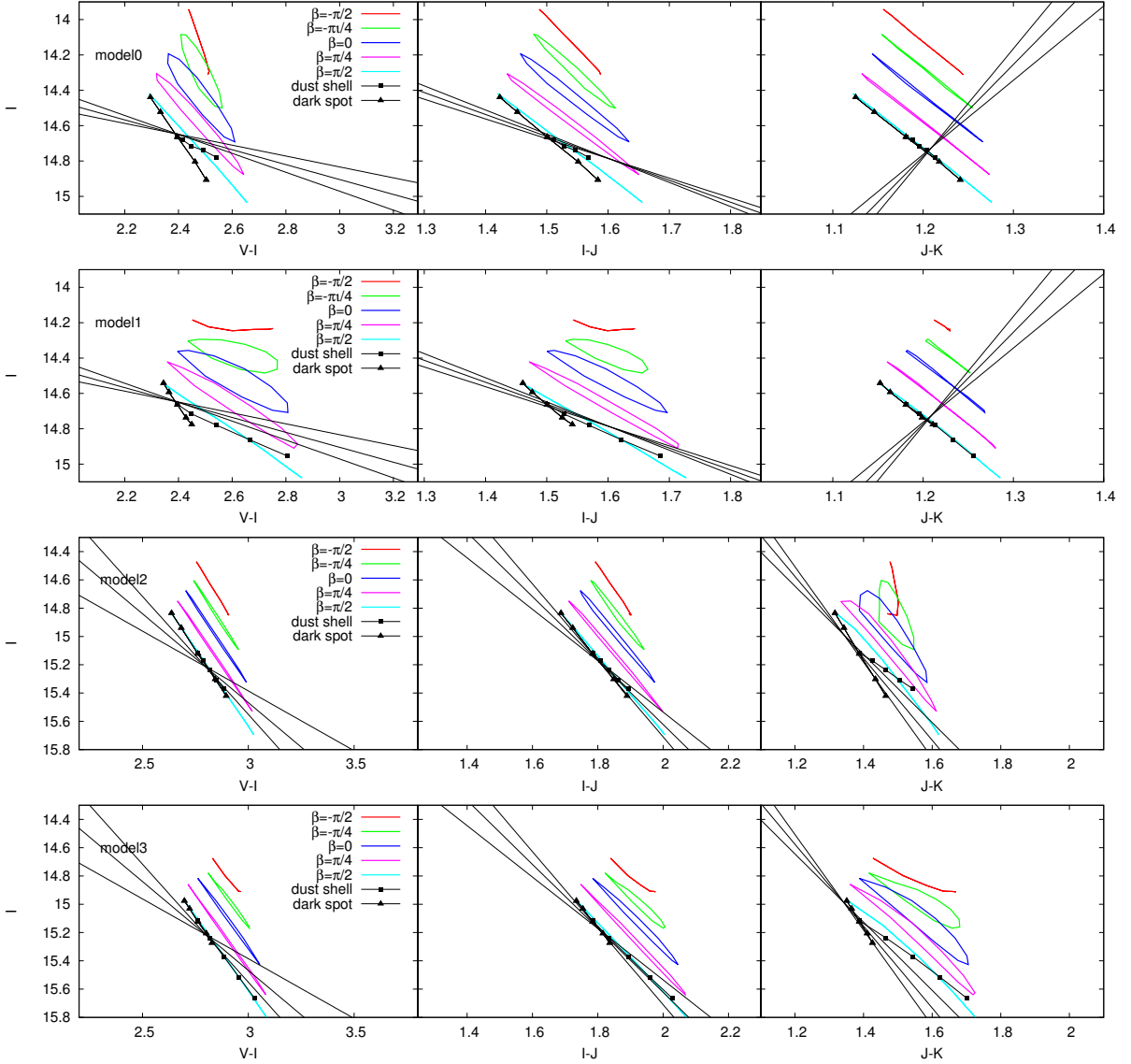


Fig. 34.— The variations of I with $V-I$, $I-J$ and $J-K_s$ for the models listed in Table 5. Models for oxygen-rich stars are shown in the upper two panels and models for carbon-rich stars are shown in the lower two panels. Solid lines with filled squares represent the dust shell model alone while solid lines with filled triangles represent the dark spot model alone. The combined dust and rotating spotted star models are shown as coloured lines with the colour indicating the phase lags β . Note that the coloured lines have been arbitrarily shifted in I to prevent confusing overlap since it is only the slope of the lines that is of interest. The slopes of the three solid black lines in each diagram represent the observed variations. The central line corresponds to the mean value of the observed line slope for stars with a relative error in the slope of less than 0.2 and the outer lines vary from the mean slope by 1σ .

assumes LSP light variations are due to dust absorption by ejected dust shells while the second model assumes a rotating star with a dark spot.

In the dust shell ejection model for LSP stars, it was found that dust absorption by the ejected mass shell could not explain the observed variations in the $(I, J - K_s)$ or $(I, V - I)$ diagrams for either oxygen-rich or carbon stars. In oxygen-rich stars, the models fail to reproduce the variations in the $(I, J - K_s)$ because the models only include variable dust absorption and not the variable H_2O absorption noted above. The failure of the dust shell models to reproduce the observed variations in the $(I, V - I)$ diagram for either oxygen-rich or carbon stars, and the failure to reproduce the observed variations in the $(I, J - K_s)$ diagram for carbon stars, suggests that dust absorption in ejected mass shells is not the cause of LSP light variations.

The LSP model involving a rotating, spotted star was not able to reproduce the observed variations in oxygen-rich stars in either the $(I, I - J)$ or $(I, V - I)$ diagrams (or the $I, J - K_s$ diagram, but here the $J - K_s$ colour is affected by H_2O absorption that is not included in the models). We thus conclude that the rotating, spotted star model is not the explanation for LSP light variations either. This result strengthens the conclusion of [Olivier & Wood \(2003\)](#) that the rotation periods of LSP stars are too long for a spotted star model to explain LSP variations. A simple combined dust and spotted star model was no better at explaining the observed magnitude–colour variations than the dust and spotted star models individually.

Our conclusion is that some process other than dust shell ejection or spot rotation lies behind the light variations seen in stars with LSPs. This unknown process seems to be responsible for the ejection of matter near the beginning of light decline. The ejected matter may be the origin of the excess mid-IR emission due to dust that is seen in stars with LSPs ([Wood & Nicholls 2009](#)).

10. SUMMARY OF THIS THESIS

At least 8 period-luminosity relations (sequences A', A, B, C', C, D, E and F) of the red giant variables are known. The origin of sequences A'-C and F is explained by pulsation in red giants, while the sequence E agrees with eclipse/ellipsoidal binarities of which system generally consists of a red giant and a less massive star than the red giant. The longest-period is the sequence D. The origin of the variability is still unknown. In general, the red giant variables belonging to the sequence D have a primary period corresponding to the stellar pulsation. Thus, the sequence D period is known as long secondary period (LSP).

The pulsating red-giant stars can be separated into two classes by the pulsation properties. One is the long-period group, so called Mira and semi-regular variables. In general, such stars are known as stars in AGB phase and those pulsation periods fall in the sequences C', C and F. Well-accepted explanation is that the sequences C and F correspond to the radial fundamental mode, while the sequence C' is the radial first overtone mode. On the other hand, red giant variables among second group show relatively irregular variabilities with smaller amplitudes and their periods fall in the sequences A', A and B. Such stars are classified into OSARG variables. The OSARGs consist of stars in RGB phase and AGB phase. The stars belonging to the former phase fall in three PL relations of b_1 – b_3 , while the stars of the latter phase forms four PL relations of a_1 – a_4 .

In part I of this thesis, we discussed the properties of pulsation in the RGB stars of OSARGs in the LMC. By comparing pulsation periods and the period ratios of theoretical models with observations obtained with OGLE-III, we have found that the radial first, second and third overtone modes and the non-radial dipole ($l = 1$) p_4 and quadrupole ($l = 2$) p_2 modes reproduce those three ridges. The RGB stars of OSARGs are consistent with stars having initial (i.e. ZAMS) masses of $\sim 0.9 - 1.4 M_\odot$ and current luminosities of $\log L/L_\odot \sim 2.8 - 3.4$. With those stellar parameters, the period corresponding to the scaled optimal frequency ν_{\max} for solar-like oscillations increases with luminosity, and passes through roughly the ridge of b_2 on the period luminosity plane. This indicates that the stochastic excitation causes the pulsation in OSARGs.

Many researchers explored the possible explanation of the origin of the variability associated with LSP. Stellar pulsation and eclipse in a binary system, respectively, have been well-discussed from theoretical and observational aspects. On the other hand, the evidence of the dust formation in circumstellar space of LSP stars was found from the recent near- and mid-IR observation (Wood & Nicholls 2009), indicating that periodic dust formations may cause the variability of LSP.

In part II, we discussed the properties of LSPs in red giants and explored a possible explanation for the light variations. Using OGLE V and I data and long-term JHK_s light curves obtained with the SIRIUS camera mounted on the IRSF 1.4m telescope, we selected a sample of 21 LSP stars (7 oxygen-rich stars and 14 carbon stars) among the SMC. We found that in the oxygen-rich stars the most broad band colours (e.g. $V - I$) get redder at the light declines in its LSP cycle, while the $J - K_s$ colour of those stars barely changes or even gets bluer when the a star dims. The most plausible explanation for the cause of getting bluer in the $J - K_s$ colour would be an

increase of H_2O vapour absorption induced by the development of a dense cool layer above the atmosphere. This scenario is consistent with the results of recent observations which suggest that a chromosphere develops during its LSPs cycle, which implies that the LSP phenomenon is associated with mass ejection from the stellar atmosphere near the beginning of light decline. We explored the possibility that photometric variations in OGLE V and I and the near-IR JHK_s can be interpreted by either dust absorption by ejected matter or dark spots on a rotating stellar surface. We have found, however, that both models can not reproduce the light and colours variations associated with LPSs. A simple combined dust absorption and dark spots model do not show any better improvement at explaining the observation than the dust and spotted star models individually. We conclude that some other mechanism is the cause of the light variations showing LSP.

Acknowledgements

I would like to thank everyone who supported me when I write this thesis. At first, I would like to express my gratitude to two supervisors who I profoundly respect: Emeritus professor. Hideyuki Saio and Emeritus professor. Peter Wood. My first contact with the stellar physics was in the Saio’s class for undergraduate students. His comprehensive and deep knowledge immediately attracted me to the world of the stellar physics. I thank him for his warm supports and always leading me to a correct direction. Emeritus Prof. Peter Wood is my supervisor when I had researched at the Australian National University (ANU). It was my first experience living abroad but I spent a wonderful time thanks to his hospitality and generous support. I would like to be thankful not only for his encouragement and helpful advice on my research, but also for his warm support to help me how to live a better life in Australia. I also would like to thank Lee Umin, who is my supervisor in my doctoral course, for his kind support and useful comments. I would like to thank Yoshifusa Ita. He provided me his new observational data and gave me a lot of valuable comments from observational aspects. I would like to express my gratitude to Makoto Hattori, who gave me the opportunity for researching at ANU as a *Young Researcher* of ‘Young researcher oversea visits program for vitalizing brain circulation’ of the Japan Society for the Promotion of Science. I would like to thank Ms’s Junko Nagasawa, Nozomi Okamoto and Satomi Miyata, who are the staffs of our astronomical-institute’s office. I have been able to proceed my tasks thanks to their supports. Finally, I would like to express my gratitude to all graduated students in the astronomical institute. Especially, I would like to deeply thank Kohei Hayashi, Sho Nakamura and Ken Mawatari, who are my contemporaries, for their friendships and encouragements. This research is partly supported by Brain Circulation Program (R2301) of the Ministry of Education, Science, Culture, and Sports in Japan and also partly supported by the Japan Society for the Promotion of Science through Grant-in-Aid for Scientific Research 26-5091.

REFERENCES

- Alexander D. R., Ferguson J. W., 1994, *ApJ*, 437, 879
- Auer L. H., 1984, in Kalkofen W., ed., *Methods in Radiative Transfer*. Cambridge Univ. Press, Cambridge, p. 237
- Basu S., Grundahl F., Stello D., Kallinger T., Hekker S., Mosser B., García R. A., Mathur S., Brogaard K., Bruntt H., *et al.*, 2011, *ApJ*, 729, L10
- Bedding T. R., Huber D., Stello D., Elsworth Y. P., Hekker S., Kallinger T., Mathur S., Mosser B., *et al.*, 2010, *ApJ*, 713, L176
- Bergeat J., Knapik A., Rutily B. 2002, *A&A*, 390, 987
- Bessell M. S., Wood P. R., 1984, *PASP*, 96, 247
- Bessell M. S., Wood P. R., Evans T. L., 1983, *MNRAS*, 202, 59
- Cassarà L. P., Piovan L., Weiss A., Salaris M., Chiosi C., 2013, *MNRAS*, 436, 2824
- Clayton G. C., 1996, *PASP*, 108, 225
- Clayton G. C., Geballe T. R., Zhang Wanshu., 2013, *AJ*, 146, 23
- Cox J.P., 1980, *Theory of stellar pulsation*, Princeton University Press
- Cox J P., Giuli R T., 1968, *Principles of Stellar Structure*, New York: Gordon & Breach
- Cuntz M., 1990, *ApJ*, 353, 255
- De Beck E., Decin L., de Koter A., Justtanont K., Verhoelst T., Kemper F., Menten K. M., 2010, *A&A*, 523, A18
- Decin L., Hony S., de Koter A., Molenberghs G., Dehaes S., Markwick-Kemper F., 2007, *A&A*, 475, 233
- Derekas A., Kiss L. L., Bedding T. R., Kjeldsen H., Lah P., Szabó G. M., 2006, *ApJ*, 650, L55
- De Ridder J., Barban C., Baudin F., Carrier F., Hatzes A. P., Hekker S., Kallinger T., Weiss W. W., Baglin A., Auvergne M., Samadi R., Barge P., Deleuil M., 2009, *Nature*, 459, 398
- Dorschner J., Begemann B., Henning T., Jaeger C., Mutschke H., 1995, *A&A*, 300, 503
- Draine B. T., Lee H. M., 1984, *ApJ*, 285, 89
- Dupret M.-A., Belkacem K., Samadi R., Montalbán J., Moreira O., Miglio A., Godart M., Ventura P., Ludwig H.-G., Grigahcène A., Goupil M.-J., Noels A., Caffau E., 2009, *A&A*, 506, 57

- Dziembowski W.A., Soszyński, I., 2010, A&A, 524, A88
- Feast M. W., 1975, IAUS, 67, 129
- Feast M. W., 1990, ASPC, 11, 538
- Fox M. W., Wood. P. R., 1982, ApJ, 259, 198F
- Fraser O. J., Hawley S. L., Cook K. H., 2008, AJ, 136, 1242
- Graczyk D., Soszyński I., Poleski R., Pietrzyński G., Udalski A., Szymański M. K., Kubiak M., Wyrzykowski Ł., Ulaczyk K., 2011, AcA, 61, 103
- Groenewegen M. A. T., de Jong T., 1993, A&A, 267, 410
- Hanner M. S., 1988, NASA Conf. Pub, 3004, 22
- Henning Th., Begemann B., Mutschke H., Dorschner J., 1995, A&AS, 112, 143
- Henry L. G., Forbes J. E., Gould N. L., 1964, ApJ, 139, 306
- Henry L. G., Wilets L., Bohm K. H., LeLevier R., Levee R. D., 1959, ApJ, 129, 628
- Hinkle K. H. Lebzelter T., Joyce R. R., Fekel F. C., 2002, AJ, 123, 1002
- Höfner S., Feuchtinger M. U., Dorfi E. A., 1995, A&A, 297, 815
- Houdashelt M. L., Bell R. A., Sweigart A. V., Wing R. F., 2000, AJ, 119, 1424
- Iglesias, C. A., Rogers, F. J., 1996, ApJ, 464, 943
- Ireland M. J., Scholz M., Wood P. R., 2011, MNRAS, 418, 114
- Ita Y., Tanabé T., Matsunaga N., Nakajima Y., Nagashima C., Nagayama T, Kato D., Kurita M., Nagata T., Sato S., Tamura M., Nakaya H., Nakada Y., 2004, MNRAS, 347, 720
- Ita Y., et al., 2015, in preparation.
- Ivezic Z., Elitzur M., 1997, MNRAS, 287, 799
- Ivezić Z., Nenkova M., Elitzur M., 1999, User Manual for DUSTY, University of Kentucky Internal Report, accessible at <http://www.pa.uky.edu/moshe/dusty>
- Johnson H. L., Méndez M. E., 1970, AJ, 75, 785
- Jumper P. H., Fisher R. T., 2013, ApJ, 769, 9
- Keller S. C., Wood P. R., 2006, ApJ, 642, 834
- Kerschbaum F., Lebzelter T., Mekul L., 2010, A&A, 524, A87

- Kiss L. L., Bedding T. R., 2003, MNRAS, 343, L79
- Kjeldsen H., Bedding T.R., 1995, A&A, 293, 87
- Lombaert R., Decin L., de Koter A., Blommaert J. A. D. L., Royer P., De Beck E., de Vries B. L., Khouri T., Min M., 2013, A&A, 554, A142
- Lucy L. B., 1967, Z.Astrophys, 65, 89
- Mondal S., Chandrasekhar T., 2005, AJ, 130, 842
- Mosser B., Dziembowski W. A., Belkacem K., Goupil M. J., Michel E., Samadi R., Soszyński I., Vradar M., Elsworth Y., Hekker S., Mathur S., 2013, A&A, 559, A137
- Nicholls C.P., Wood P.R., 2012, MNRAS, 421, 2616
- Nicholls C.P., Wood P.R., Cioni M.-R.L., 2010, MNRAS, 405, 1770
- Nicholls C. P., Wood P. R., Cioni M.-R. L., Soszyński I., 2009, MNRAS, 399, 2063
- Olivier E. A., Wood P. R., 2003, ApJ, 584, 1035
- Ossenkopf V., Henning Th., Mathis J. S., 1992, A&A, 261, 567
- Paxton, B., Bildsten, L., Dotter, A., Herwig, F. Lesaffre, P., Timmes, F., 2011, ApJS, 192, id.3
- Pégourié B., 1988, A&A, 194, 335
- Potekhin A. Y., Chabrier G., 2010, Contrib. Plasma Phys., 50, 82
- Rayner J. T., Cushing M. C., Vacca W. D., 2009, ApJS, 185, 289
- Reimers D., 1975, Mem. Soc. Roy. Sci. de Liege, 8, 369
- Rogers F. J., Nayfonov A., 2002, ApJ, 576, 1064
- Saio, H., Cox, J. P., 1980, ApJ, 236, 549
- Saio, H., Winget, D. E., Robinson, E. L., 1983, ApJ, 265, 982
- Saumon D., Chabrier G., van Horn H. M., 1995, ApJS, 99, 713
- Soker N., Clayton G. C., 1999, MNRAS, 307, 993
- Soszyński I., 2007, ApJ, 660, 1486
- Soszyński I., Dziembowski W. A., Udalski A., Kubiak M., Szymański M. K., Pietrzyński G., Wyrzykowski Ł., Szewczyk O., Ulaczyk K., 2007, AcA, 57, 201
- Soszyński I., Udalski A., 2014, ApJ, 788, 13

- Soszyński I., Udalski A., Kubiak M., Szymański M., Pietrzyński G., Zebruń K., Szewczyk O., Wyrzykowski L., 2004, *AcA*, 54, 129
- Soszyński I., Udalski A., Kubiak M., Szymański M. K., Pietrzyński G., Zebruń K., Szewczyk O., Wyrzykowski L., Dziembowski W. A., 2004, *AcA*, 54, 347
- Soszyński I., Udalski A., Szymański M. K., Kubiak M., Pietrzyński G., Wyrzykowski L., Ulaczyk K., Poleski R., Kozłowski S., Pietrukowicz P., 2011, *AcA*, 61, 217
- Soszyński I., Udalski A., Szymański M. K., Kubiak M., Pietrzyński G., Wyrzykowski L., Szewczyk O., Ulaczyk K., Poleski R., 2009, *AcA*, 59, 239
- Soszyński I., Udalski A., Szymański M. K., Kubiak M., Pietrzyński G., Wyrzykowski L., Ulaczyk K., Poleski R., Kozłowski S., Pietrukowicz P., Skowron J., 2013, *AcA*, 63, 21
- Soszyński I., Wood P. R., 2013, *ApJ*, 763, 103
- Soszyński I., Wood P. R., Udalski A., 2013, *ApJ*, 779, 167
- Stello D., Compton D. L., Bedding T. R., Christensen-Dalsgaard J., Kiss L. L., Kjeldsen H., Bellamy B., García R. A., Mathur S., 2014, *ApJ*, 788, L10
- Stothers R. B., 2010, *ApJ*, 725, 1170
- Tabur V., Bedding T. R., Kiss L. L., Giles T., Derekas A., Moon T. T., 2010, *MNRAS*, 409, 777
- Takayama M., Saio H., Ita Y., 2013, *MNRAS*, 431, 3189
- Takayama M., Wood P. R., Ita Y., 2015, *MNRAS*, 448, 464
- Timmes F. X., Swesty F. D., 2000, *ApJS*, 126, 501
- Tsuji T., 2000, *ApJ*, 538, 801
- Van Hamme W., Wilson R. E., 2003, *ASPC*, 298, 323
- van Loon J. Th., Cioni M.-R. L., Zijlstra A. A., Loup C., 2005, *A&A*, 438, 273
- Van Winckel H., Lloyd Evans T., Briquet M., De Cat P., Degroote P., De Meester W., De Ridder J., Deroo P., Desmet M., et al., 2009, *A&A*, 505, 1221
- Van Winckel H., Waelkens C., Fernie J. D., Waters L. B. F. M., 1999, *A&A*, 343, 202
- Wagner R. L., 1974, *ApJ*, 191, 173
- Wilson R. E., Devinney E. J., 1971, *ApJ*, 166, 605
- Wilson R. E., 2012, *AJ*, 144, 73

- Winters J. M., Fleischer A. J., Gauger A., Sedlmayr E., 1994, *A&A*, 290, 623
- Wood P. R., Alcock C., Allsman R. A., Alves D., Axelrod T. S., Becker A. C., Bennett D. P., Cook K. H., Drake A. J., Freeman K. C., et al. 1999, *IAU Symp.*, 191, 151
- Wood P. R., Nicholls C. P., 2009, *ApJ*, 707, 573
- Wood P. R., Olivier E. A., Kawaler S. D., 2004, *ApJ*, 604, 800
- Wood P. R., Sebo M., 1996, *MNRAS*, 282, 958
- Wray J. J., Eyer L., Paczyński B., 2004, *MNRAS*, 349, 1059
- Xiong D. R., Deng L., 2007, *MNRAS*, 378, 1270

A. Stellar pulsation

In the first part of this thesis, we calculated pulsation periods according to the method introduced by [Saio, Winget, & Robinson \(1983\)](#) and [Saio & Cox \(1980\)](#). In this appendix, we will briefly discuss the theories of linear non-adiabatic radial and non-radial pulsations. The variables used here generally correspond to those of [Saio, Winget, & Robinson \(1983\)](#) and [Saio & Cox \(1980\)](#).

The basic equations for hydrodynamics for the fluid in the stellar interior are given by

$$\begin{aligned}
 \left(\frac{\partial \rho}{\partial t} \right) + \nabla \cdot (\rho \mathbf{v}) &= 0, \\
 \rho \frac{d\mathbf{v}}{dt} &= \rho \left(\frac{\partial \mathbf{v}}{\partial t} \right) + \rho (\mathbf{v} \cdot \nabla) \mathbf{v} = -\nabla P - \rho \nabla \Phi, \\
 \nabla^2 \Phi &= 4\pi r^2 G \rho, \\
 \rho T \left(\frac{\partial S}{\partial t} \right) &= \rho (\epsilon_n - \epsilon_\nu) - \nabla \cdot \mathbf{F},
 \end{aligned} \tag{A1}$$

where P , ρ , T and S are the pressure, the gas density, the temperature and the entropy, respectively. \mathbf{v} represents the vector of the velocity of the fluid. Φ and G are the gravitational potential and the gravitational constant. \mathbf{F} is the vector of the energy flux. ϵ_n and ϵ_ν are the nuclear energy generation rate and the neutrino cooling rate per unit mass, respectively. q is the heat per unit mass. Applying linear perturbations and assuming the temporal variations of perturbed quantities to be proportional to $e^{i\sigma t}$, where σ is the angular frequency of pulsation, we obtain the first-order differential equations assuming the linear perturbations.

A.1. Radial pulsation

The basic equations for linear non-adiabatic radial pulsation have been well discussed. We use the Lagrangian perturbations described at $\delta r/r$, $\delta P/P$, $\delta T/T$ and $\delta L/L$. The luminosity $L(r)$ is given by $L(r) = L_{\text{rad}} + L_{\text{conv}}$, where ‘rad’ and ‘conv’ mean radiation and convection, respectively. Since the pulsation periods (i.e. approximately same as the dynamical time scale) would be enough shorter than the thermal time (i.e. convection time scale), we assume for simplicity that the convection flux perturbation δL_{conv} can become 0. Then we obtain following four first-order

differential equations

$$\begin{aligned}
-r\sigma^2 \frac{\delta r}{r} &= \left(4\frac{\delta r}{r} + \frac{\delta P}{P}\right) \frac{GM_r}{r^2} - 4\pi r^2 P \frac{d}{dM_r} \left(\frac{\delta P}{P}\right), \\
i\sigma C_P T \left[\frac{\delta T}{T} - \nabla_{ad} \frac{\delta P}{P}\right] &= -L \frac{d}{dM_r} \frac{\delta L_r}{L}, \\
\frac{\delta \rho}{\rho} &= -3\frac{\delta r}{r} - 4\pi r^3 \rho \frac{d}{dM_r} \left(\frac{\delta r}{r}\right), \\
\frac{\delta L}{L} &= \frac{L_{\text{rad}}}{L} \left[4\frac{\delta r}{r} - K + \frac{1}{(dT/dM_r)} \frac{d}{dM_r} \left(\frac{\delta T}{T}\right)\right], \tag{A2}
\end{aligned}$$

where

$$\begin{aligned}
\frac{\delta T}{T} &= \left(\frac{\partial \ln T}{\partial \ln P}\right)_S \left(\frac{\delta P}{P}\right) + \left(\frac{\partial \ln T}{\partial S}\right)_P \delta S = \nabla_{ad} \frac{\delta P}{P} + \frac{\delta S}{C_P}, \quad \nabla_{ad} \equiv \left(\frac{\partial \ln T}{\partial \ln P}\right)_S, \\
C_P &\equiv T \left(\frac{\partial S}{\partial T}\right)_P, \quad \frac{\delta \rho}{\rho} = \left(\frac{\partial \ln \rho}{\partial \ln T}\right)_P \left(\frac{\delta T}{T}\right) + \left(\frac{\partial \ln \rho}{\partial \ln P}\right)_T \left(\frac{\delta P}{P}\right), \\
K &\equiv \left(\frac{\partial \ln \kappa}{\partial \ln T}\right)_\rho \left(\frac{\delta T}{T}\right) + \left(\frac{\partial \ln \kappa}{\partial \ln \rho}\right)_T \left(\frac{\delta \rho}{\rho}\right), \quad L_{\text{rad}} = -\frac{64\pi^2 a c r^4 T^4}{3\kappa} \frac{d \ln T}{dM_r}, \\
\Gamma_1 &\equiv \left(\frac{d \ln P}{d \ln \rho}\right)_{ad}, \quad \Gamma_3 - 1 \equiv \left(\frac{d \ln T}{d \ln \rho}\right)_{ad}. \tag{A3}
\end{aligned}$$

κ is the mean opacity. a , c and G represent the radiation constant, the speed of light and the gravitational constant, respectively. σ is the pulsation frequency, although it consists of a real part and an imaginary part in the case of non-adiabatic pulsation calculation. The dimensionless frequency ω is defined as $\omega \equiv \sigma / \sqrt{\frac{GM}{R^3}}$, where M is the stellar mass, and R is the stellar radius.

Bottom of the envelope, the amplitude of pulsation diminishes. Thus, at the inner boundary we used following conditions

$$\frac{\delta r}{r} = 0, \quad \frac{\delta L}{L} = 0. \tag{A4}$$

On the other hand, the pressure vanishes at the outer boundary of the star. At the outer boundary, we assume that the luminosity L is given by the Stefan-Boltzmann law $L \propto R^2 T_{\text{eff}}^4$, where T_{eff} is the effective temperature. Then we obtained following conditions at the outer boundary of the star

$$\frac{\delta P}{P} = 0, \quad \frac{\delta L}{L} = 2\frac{\delta r}{r} + 4\frac{\delta T}{T}. \tag{A5}$$

A.2. Non-radial pulsation

Using the Eddington approximation, the radiative flux is described by

$$\mathbf{F}_{\text{rad}} = -\frac{4\pi}{3\kappa\rho}\nabla\mathbf{J}, \quad (\text{A6})$$

where \mathbf{J} is the mean intensity. We assume the local thermodynamic equilibrium, then we obtain \mathbf{J} :

$$\mathbf{J} = \frac{ac}{4\pi}T^4. \quad (\text{A7})$$

The perturbations for the non-adiabatic non-radial pulsation are usually represented by the Eulerian (δ) and Lagrangian (δ) perturbations with a spherical harmonic $Y_{lm}(\theta, \phi)$ given by

$$\begin{aligned} F'(r, \theta, \phi, t) &= F'(r)Y_{lm}(\theta, \phi)e^{i\sigma t}, \\ \delta F(r, \theta, \phi, t) &= \delta F(r)Y_{lm}(\theta, \phi)e^{i\sigma t}. \end{aligned} \quad (\text{A8})$$

The relation between the two kind of perturbations are expressed by

$$\delta F = F' + \xi_r \frac{dF}{dr}, \quad (\text{A9})$$

where ξ_r is the the Lagrangian perturbation in radius, δr .

For describing linear non-adiabatic non-radial pulsation equations, we use the six variables defined as

$$\begin{aligned} y_1 &\equiv \frac{\delta r}{r}, \quad y_2 \equiv \frac{1}{gr} \left(\frac{P'}{\rho} + \Phi' \right), \quad y_3 \equiv \frac{1}{gr} \Phi', \\ y_4 &\equiv \frac{1}{g} \frac{d\Phi'}{dr}, \quad y_5 \equiv \frac{\delta S}{C_P}, \quad y_6 \equiv \frac{L_{\text{rad}}}{L}, \end{aligned} \quad (\text{A10})$$

where S is the entropy per unit mass and C_P is the specific heat at constant pressure per unit mass.

By linearizing the basic equations represented by Equation A2 and Equation A6, we obtain

the six differential basic equations for linear non-adiabatic non-radial pulsation

$$\begin{aligned}
r \frac{dy_1}{dr} &= \left(\frac{V}{\Gamma_1} - 3 \right) y_1 + \left(\frac{l(l+1)}{C_1 \omega^2} - \frac{V}{\Gamma_1} \right) y_2 + \frac{V}{\Gamma_1} y_3 + \tilde{\chi} y_5, \\
r \frac{dy_2}{dr} &= (C_1 \omega^2 + rA) y_1 + (1 - U - rA) y_2 + rA y_3 + \tilde{\chi} y_5, \\
r \frac{dy_3}{dr} &= (1 - U) y_3 + y_4, \\
r \frac{dy_4}{dr} &= -rAU y_1 + \frac{UV}{\Gamma_1} y_2 + \left(l(l+1) - \frac{UV}{\Gamma_1} \right) y_3 - U y_4 - \tilde{\chi} U y_5, \\
\frac{r}{V \nabla} \frac{dy_5}{dr} &= (B_1 + \alpha(U - C_1 \omega^2) + 4(1 - \alpha)) y_1 - \left(B_1 + (1 - \alpha) \frac{l(l+1)}{C_1 \omega^2} \right) y_2 \\
&\quad + B_1 y_3 + \alpha y_4 + (-\kappa_T + \kappa_\rho \tilde{\chi} + 4) y_5 - y_6, \\
r \frac{dy_6}{dr} &= (B_2 - l(l+1)(1 - \alpha)) y_1 + \left(l(l+1) \left(\frac{\eta}{C_1 \omega^2} - \alpha \right) + B_2 \right) y_2 \\
&\quad + (l(l+1)\alpha - B_2) y_3 + \left(-\frac{l(l+1)}{V \nabla} + B_3 - i\omega B_4 \right) y_5 - \eta y_6,
\end{aligned} \tag{A11}$$

where

$$\begin{aligned}
U &\equiv \frac{4\pi r^3 \rho}{M_r}, \quad V \equiv \frac{\rho g r}{P}, \quad g \equiv \frac{GM_r}{r^2}, \quad \tilde{\chi} \equiv \left(\frac{\partial \ln P}{\partial \ln T} \right)_\rho \bigg/ \left(\frac{\partial \ln P}{\partial \ln \rho} \right)_T, \\
A &\equiv \frac{1}{\rho} \frac{d\rho}{dr} - \frac{1}{\Gamma_1 P} \frac{dP}{dr}, \quad \nabla \equiv \frac{d \ln T}{d \ln P}, \quad \alpha \equiv \frac{\nabla_{ad}}{\nabla}, \quad C_1 \equiv \left(\frac{r}{R} \right)^3 \left(\frac{M}{M_r} \right), \\
\kappa_T &\equiv \left(\frac{\partial \ln \kappa}{\partial \ln T} \right)_\rho, \quad \kappa_\rho \equiv \left(\frac{\partial \ln \kappa}{\partial \ln \rho} \right)_T, \quad B_1 \equiv V \left(\nabla_{ad} \kappa_T + \frac{\kappa_\rho}{\Gamma_1} - 4 \nabla_{ad} \right) + \alpha \left(V + \frac{d \ln \nabla_{ad}}{d \ln r} \right), \\
B_2 &\equiv -\eta \frac{V}{\Gamma_1}, \quad B_3 \equiv \eta \tilde{\chi}, \quad B_4 \equiv \frac{4\pi r^3 \rho T C_P}{L_{rad}} \left(\frac{GM}{R^3} \right)^{1/2}, \quad \eta \equiv \frac{d \ln L_{rad}}{d \ln r}
\end{aligned} \tag{A12}$$

Note we assumed no perturbation of the convective flux, $\delta(\nabla \cdot \mathbf{F}) = 0$.

At the center of the star, g should become 0. Therefore, the gas density and the pressure (and hence the temperature) should be constant. Under the requirements, we use the conditions in the inner boundary given by,

$$\frac{C_1 \omega^2}{l} y_1 - y_2 = 0, \quad l y_3 - y_4 = 0. \tag{A13}$$

The perturbation of the gravitational potential Φ' should become 0 when r becomes 0. Therefore, we obtain $y_{1\sim 4} \propto r^{l-2}$. Then, we obtain the last one condition in the inner boundary

$$y_5 \propto r^l. \tag{A14}$$

As mentioned in Section A.1, the pressure should become 0 in the outer boundary (i.e. the stellar surface). In addition, the perturbation of the gravitational potential $|\Phi'/\Phi|$ should be a

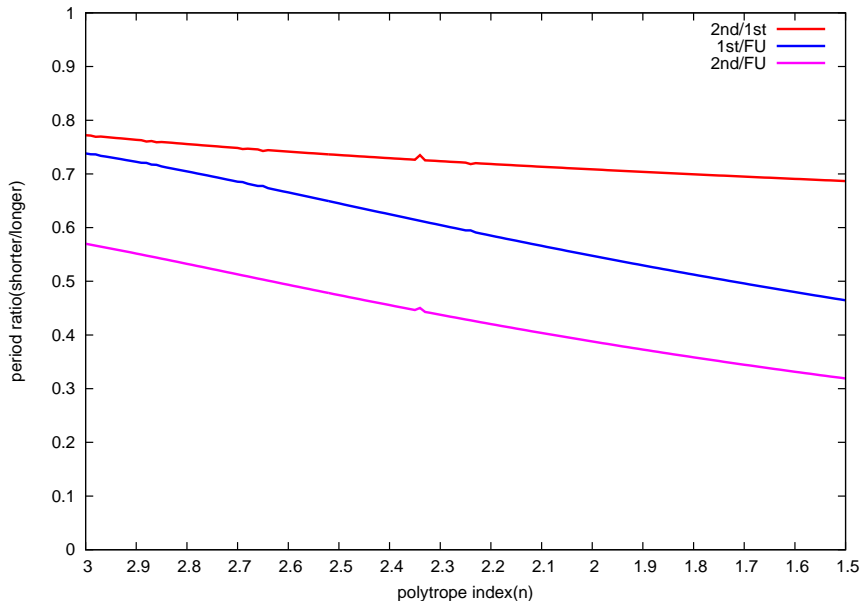


Fig. 35.— Period ratios of the radial fundamental - the second overtone mode in the adiabatic pulsations for the polytropes. The different polytropic indexes represent the different stellar structures.

small value compared with unity to satisfy the assumption of linear perturbation. Thus, we obtain the outer boundary conditions,

$$y_1 - y_2 + y_3 = 0, \quad (l+1)y_3 + y_4 = 0. \quad (\text{A15})$$

Note that to obtain the equations above, we used the relations of $U \rightarrow 0$ and $V \gg 1$. Assuming no radiation coming into inward through the outer boundary, we chose the following condition

$$\mathbf{F} = 2\pi\mathbf{J}, \quad (\text{A16})$$

then we obtain the linearized equation of this equation as the outer boundary condition by

$$\left(\frac{1}{2} - \nabla_{ad}V\right)y_1 + V\nabla_{ad}(y_2 - y_3) + y_5 - \frac{1}{4}y_6 = 0. \quad (\text{A17})$$

A.3. Period ratio

In the two sections above, we obtained the four first-order differential equations for the non-adiabatic radial oscillation, and the six first-order differential equations for the non-adiabatic non-radial oscillation. Giving suitable boundary conditions (e.g. those of mentioned above), we can solve those differential equations. However, since the number of the given boundary conditions has

exceeded the allowable number, the dimensionless frequency ω (and hence the pulsation frequency σ) has been permitted to have a value at only the appropriate number to satisfy the given boundary conditions. Thus, ω corresponds to so called ‘eigenvalue’ for the differential equations. Considering non-adiabatic oscillation, the eigenvalues are generally complex numbers. In general, plural values are permitted as the eigenvalues for the stellar structure and the boundary conditions. For example, in adiabatic radial pulsation (i.e. $P = \rho^{\Gamma_1}$ (and hence $\delta P/P = \Gamma_1 \delta \rho/\rho$) is always satisfied), the pulsation mode corresponding to the smallest eigenvalue is called ‘fundamental mode’, while the modes corresponding to the second and third smallest eigenvalues are ‘first overtone mode’ and ‘second overtone mode’, respectively. The eigenvalue ω depends on the stellar structure. Since the period ratio between different modes is expressed as

$$\frac{P_1}{P_2} = \frac{1/\sigma_1}{1/\sigma_2} = \frac{\omega_2}{\omega_1} \sqrt{\frac{GM}{R^3}} = \frac{\omega_2}{\omega_1}, \quad (\text{A18})$$

The ratio depends on the stellar structure. Figure 35 shows the period ratios of the first three modes of the adiabatic radial pulsation for the polytropes. If the energy in the envelope is carried by pure radiation, the structure of the envelope corresponds to polytrope index of ~ 3 . When the envelope structure is consistent with the adiabatic temperature gradient (i.e. similar to the case of the fully convective envelope), the envelope structure corresponds to polytrope index of 1.5. In a given stellar structure, the different period ratios represent the different combinations of the two pulsation modes consisting of the period ratios. This indicates that the period ratios are useful for the purpose of the mode determinations.

B. MESA code

Modules for Experiments in Stellar Astrophysics (MESA; Paxton et al. 2011) code is an open source 1D stellar evolution code based on the Henyey relaxation method (e.g., Henyey et al. 1959, 1964). We discuss the basic method to solve the stellar evolution problems and introduce the MESA code briefly.

Assuming spherical symmetry for a star excluding stellar rotation nor magnetic field, and considering the gravitational contraction or expansion, the spacial structure along radial direction of a star and its temporal evolution are generally described by the following basic equations:

$$\frac{dv}{dt} = -4\pi r^2 \left(\frac{\partial P}{\partial M_r} \right) - \frac{GM_r}{r^2}, \quad (\text{B1})$$

$$T \left(\frac{\partial S}{\partial t} \right) = (\epsilon_n - \epsilon_\nu) - \left(\frac{\partial L_r}{\partial M_r} \right), \quad (\text{B2})$$

$$\left(\frac{\partial r}{\partial M_r} \right) = \frac{1}{4\pi r^2 \rho}, \quad (\text{B3})$$

$$\frac{dT}{dM_r} = \frac{T}{P} \left(\frac{\partial P}{\partial M_r} \right) \left(\frac{d \ln T}{d \ln P} \right), \quad (\text{B4})$$

where ϵ_n and ϵ_ν are the nuclear energy generation rate per unit mass and the thermal neutrino-loss (i.e. the neutrino cooling) rate per unit mass, respectively. In general, dv/dt is assumed to be 0 except for the cases of a rapid collapse or expansion such as the gravitational collapse before super nova. To treat convection, the standard mixing length theory formulated by e.g. [Cox & Giuli \(1968\)](#) is generally assumed. When a star is contracting or expanding, the gravitational energy changes. The rate of change of gravitational energy per unit mass due to contraction or expansion (ϵ_g) is given by

$$\epsilon_g = -T \frac{\partial S}{\partial t}. \quad (\text{B5})$$

Therefore, the energy conservation is described, from Equation [B2](#), following as

$$\epsilon_n - \epsilon_\nu + \epsilon_g = \frac{dL_r}{dM_r}. \quad (\text{B6})$$

If the hydrostatic equilibrium condition is satisfied temporally at any Lagrangian point M_r , Equation [B1](#) becomes

$$\frac{dP}{dM_r} = -\frac{GM_r}{4\pi r^4}. \quad (\text{B7})$$

Thus, the stellar structure along radial direction are described by Equations [B3](#), [B4](#), [B6](#) and [B7](#). The differential equations to solve the stellar structure at a given time t_i , however, are not closed by themselves because the number of the unknown variables (and hence they are the solutions of those equations) exceeds the permissible number. To close the equations, we need an equation of state (EOS) for the gas. In the MESA code, the EOSs are given by the MESA EOS $\rho - T$ tables based on the OPAL EOS tables ([Rogers & Nayfonov 2002](#)) and the SCVH tables ([Saumon et al. 1995](#)). When either ρ or T is in the outside of the range of the MESA EOS tables, the HELM ([Timmes & Swesty 2000](#)) and the PC ([Potekhin & Chabrier 2010](#)) are used. With the equation of states and the opacities: the OPAL opacity tables ([Iglesias & Rogers 1996](#)) are basically employed in the MESA code, the stellar structure at a given time t_i can be calculated numerically by the Henyey relaxation method, which describes the basic equations mentioned above by the form of the difference equations and solves r , L_r , P and T by the multidimensional Newton-Raphson solver.

Evolution of the stellar structure from t_i to t_{i+1} is determined by the change of the chemical composition distribution along radial direction in the stellar interior due to the nuclear synthesis and the mixing of the elements by turbulent convection, described as

$$\left(\frac{\partial X_i}{\partial t} \right)_{M_r} = \left(\frac{\partial X_i}{\partial t} \right)_n + \frac{\partial}{\partial M_r} \left((4\pi r \rho)^2 D \frac{\partial X_i}{\partial M_r} \right), \quad (\text{B8})$$

where X_i is the abundance of the element i and D is the diffusion coefficient of the mixing by turbulent convection. The first term of the RHS indicates the nuclear synthesis of the element i . With the new distribution of the chemical composition at time t_{i+1} , the stellar structure at t_{i+1} can be solved. This is a brief introduction of the basic method to solve the stellar evolution problems.

C. Radiative transfer problem in a spherically symmetric dust shell

The DUSTY code is based on the method proposed by Ivezić & Elitzur (1997). They solved radiation transfer problem in a spherical dust shell surrounding a star. In this appendix, we discuss their method briefly. We basically used the same symbols used in Ivezić & Elitzur (1997).

C.1. The equation of radiative transfer

A familiar expression of the radiative transfer equation in stationary state is

$$\frac{dI_\lambda}{dl} = \kappa_\lambda(S_\lambda - I_\lambda), \quad (\text{C1})$$

where κ_λ is the total extinction coefficient at wavelength λ , given by $\kappa_\lambda = \kappa_{a\lambda} + \kappa_{s\lambda}$, of which $\kappa_{a\lambda}$ and $\kappa_{s\lambda}$ are the absorption and the scattering coefficients, respectively. The optical depth along the path satisfies $d\tau_\lambda = \kappa_\lambda dl$. Thus, the total optical depth along the path is $\tau_\lambda^T = \int \kappa_\lambda dl$. We define the dimensionless distance

$$y \equiv l/l_1, \quad (\text{C2})$$

where l_1 is the arbitrary length-scale. Then, we obtain the equation of radiative transfer

$$\frac{dI_\lambda(y)}{dy} = \tau_\lambda^T \eta(y)(S_\lambda(y) - I_\lambda(y)), \quad (\text{C3})$$

where $\eta_\lambda(y)$ is the dimensionless extinction coefficient at the position y ,

$$\eta(y) = \frac{1}{\tau_\lambda^T} \frac{d\tau_\lambda(y)}{dy} = \frac{\kappa_\lambda(y)}{\int \kappa_\lambda(y) dy}. \quad (\text{C4})$$

If the dust properties are unvarying with the position along the path, η indicates the normalized density profile of the absorbers $\eta(y) = n_a / \int n_a(y) dy$. For simplification, we assume that dust grains consist of a single type with the temperature T . We do not consider line emissions and photoionization, therefore the source function becomes

$$S_\lambda = (1 - \varpi_\lambda) B_\lambda(T) + \varpi_\lambda \int I_\lambda g(\Omega', \Omega) \frac{d\Omega'}{4\pi}, \quad (\text{C5})$$

where $B_\lambda(T)$ is the Planck function corresponding to temperature T , and $g(\Omega', \Omega)$ is the angular phase function for coherent scattering from direction Ω' to Ω . ϖ_λ represents the extinction coefficient ratio of the scattering to the overall

$$\varpi_\lambda \equiv \frac{\kappa_{s\lambda}}{\kappa_\lambda}. \quad (\text{C6})$$

We assume for simplicity $g(\Omega', \Omega) = 0$, meant the case of isotropic scattering. The radiative equilibrium condition is

$$\frac{d}{dl} \int d\Omega \int I_\lambda d\lambda = \int d\Omega \int \kappa_\lambda (S_\lambda - I_\lambda) d\lambda = 0, \quad (\text{C7})$$

or

$$\int d\Omega \int \kappa_\lambda S_\lambda d\lambda = 4\pi \int \kappa_\lambda J_\lambda d\lambda, \quad (\text{C8})$$

where J_λ is the mean intensity, given by $J_\lambda = \int I_\lambda \frac{d\Omega}{4\pi}$. From Equations C5 and C8, we obtain the radiative equilibrium condition expressed by $B_\lambda(T)$ and J_λ

$$\int q_{a\lambda} B_\lambda(T) = \int q_{a\lambda} J_\lambda d\lambda, \quad (\text{C9})$$

where $q_{a\lambda}$ is the absorption coefficient at λ normalized by that at arbitrary wavelength λ_0

$$q_{a\lambda} \equiv \frac{\kappa_{a\lambda}}{\kappa_{a\lambda_0}} = q_\lambda \frac{1 - \varpi}{1 - \varpi_0}, \quad (\text{C10})$$

and

$$q_\lambda \equiv \frac{\kappa_\lambda}{\kappa_{\lambda_0}}. \quad (\text{C11})$$

From the expression of q_λ , the relation between q_λ and τ_λ is

$$\tau_\lambda = q_\lambda \tau_{\lambda_0}. \quad (\text{C12})$$

C.2. Spherically symmetric dust shell

In this subsection, we discuss the radiative transfer problem in a dust shell. Here we assume spherical symmetry as the geometrical shape of the dust shell, surrounding a spherical star having radius of r_e . We consider the case of that the radiative source is only the central star. We denote the normalized radius of the star $\theta_{e1} = r_e/r_1$, where r_1 corresponds to the shell inner radius. The external flux at r_1 is, therefore, given by

$$F_{e\lambda} = \int \mu I_{e\lambda} d\Omega \approx \pi \theta_{e1}^2 I_{e\lambda}. \quad (\text{C13})$$

From the energy conservation, the bolometric external flux satisfies

$$F_{e1} = \int F_{e\lambda}(r_1) d\lambda = \frac{L_e}{4\pi r_1^2}. \quad (\text{C14})$$

Here L_e is the bolometric luminosity. We denote the normalized internal flux (i.e. the flux distribution)

$$f_{e\lambda} = \frac{F_{e\lambda}}{F_{e1}}. \quad (\text{C15})$$

Normalizing the radial distance as $y = r/r_1$, we obtain the spatial distribution of the normalized extinction coefficient

$$\eta(y) = \frac{\kappa_\lambda(y)}{\int_1^\infty \kappa_\lambda(y) dy}. \quad (\text{C16})$$

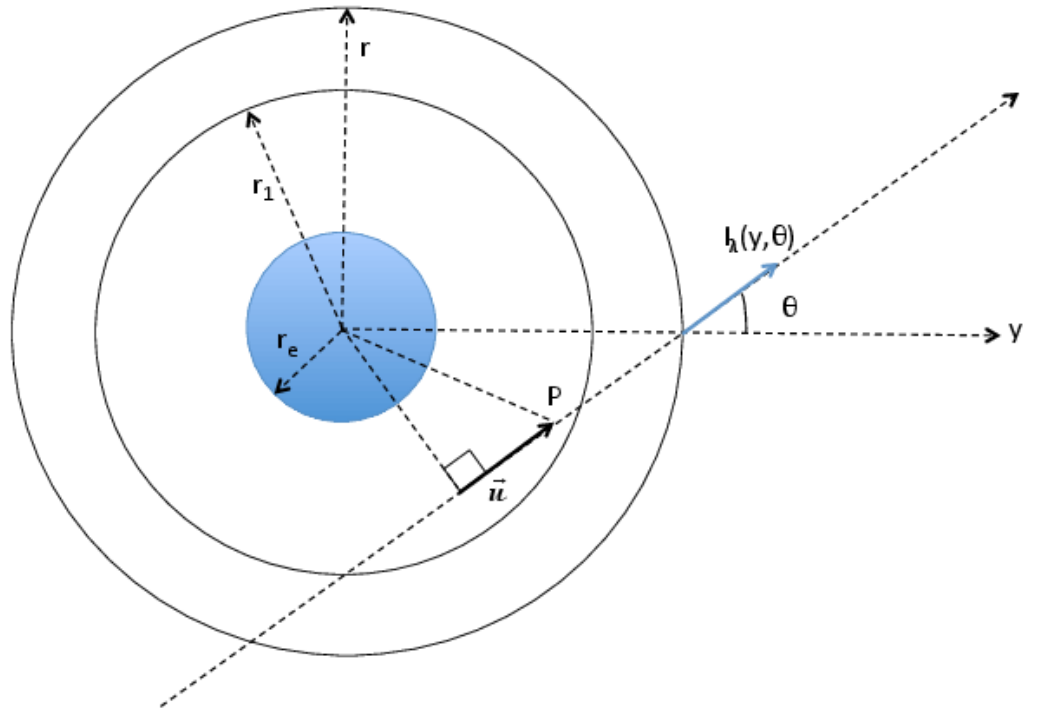


Fig. 36.— Schematic diagram of the geometrical arrangement of the central star and the dust shell.

Note again, if the dust properties unvarying with the radial distance, η gives the density profile of the absorbers (i.e. the dust) along the radial direction. Figure 36 shows the schematic diagram expressing the geometrical arrangement of the central star and the dust shell. The vector \mathbf{u} makes an angle θ with the radius vector. At the point P, η is described by $\eta_P = \eta(\sqrt{u^2 + y^2 \sin^2 \theta})$. Thus, at any point y , the optical depth from the origin of \mathbf{u} along the path pointing out the same direction of \mathbf{u} is

$$\tau_\lambda(y, \theta) = \tau_\lambda^T \int_0^{y \cos \theta} \eta \left(\sqrt{u^2 + y^2 \sin^2 \theta} \right) du. \quad (\text{C17})$$

The intensity $I_\lambda(y, \theta)$ at point y , corresponding to that of Figure 36, can be obtained from the radiative transfer equation;

$$I_\lambda(y, \theta) = I_{e\lambda} e^{-\tau_\lambda(y)} \Theta \left(\frac{\theta_{e1}}{y} - \theta \right) + I_{d\lambda}(y, \theta), \quad (\text{C18})$$

where

$$\Theta(x) \equiv \begin{cases} 1, & (x > 0) \\ 0, & (\text{otherwise}) \end{cases} \quad (\text{C19})$$

The intensity of the diffuse radiation $I_{d\lambda}(y, \theta)$ is now obtained from the source function;

$$I_{d\lambda}(y, \theta) = \int S_\lambda(y', \theta) \exp(\tau_\lambda(y', \theta) - \tau_\lambda(y, \theta)) d\tau_\lambda(y', \theta). \quad (\text{C20})$$

Using Equations C13–C15, and C18, we obtain the mean intensity

$$J_\lambda(y) = \frac{F_{e1}}{4\pi y^2} f_{e\lambda} e^{\tau_\lambda(y)} + J_{d\lambda}(y). \quad (\text{C21})$$

We assume the dust shell with the temperature of T_1 at the bottom (i.e. $T(r_1) = T_1$). The ratio

$$b_\lambda(T_1) = \frac{\pi}{\sigma T_1^4} B_\lambda(T_1), \quad (\text{C22})$$

is the normalized Planck function. From the radiative equilibrium condition (Equation C9) and Equation C22, we obtain the relation between the shell bottom temperature T_1 and the temperature at any point y , T ;

$$q_{aP}(T) T^4 = q_{aP}(T_1) T_1^4 \frac{\int q_{a\lambda} J_\lambda(y) d\lambda}{\int q_{a\lambda} J_\lambda(1) d\lambda}, \quad (\text{C23})$$

where

$$q_{aP}(T) = \int q_{a\lambda} b_\lambda(T) d\lambda \quad (\text{C24})$$

is the Planck mean of the absorption efficiency. The characteristic flux of the emission from dust at r_1 is σT_1^4 . Therefore, the flux ratio

$$\Psi = \frac{4\sigma T_1^4}{F_{e1}} = \frac{q_{ae}}{q_{aP}(T_1)} \frac{1}{1 - \epsilon} = \frac{4\pi}{q_{aP}(T_1)F_{e1}} \int q_{a\lambda} J_\lambda(1) d\lambda, \quad (\text{C25})$$

where

$$q_{ae} = \int q_{a\lambda} f_{e\lambda} d\lambda, \quad (\text{C26})$$

and

$$\epsilon = \frac{\int q_{a\lambda} J_{d\lambda}(1) d\lambda}{\int q_{a\lambda} B_\lambda(T_1) d\lambda} \quad (\text{C27})$$

is also the characteristic parameter of the model. The right-hand term of the equation indicates that Ψ is an explicit function of J_λ . Assuming isotropic scattering (i.e. the scattering term of Equation C5 $g(\Omega', \Omega) = 1$), described by the integral term, becomes $\varpi_\lambda \int I_\lambda g(\Omega', \Omega) \frac{d\Omega'}{4\pi} = \varpi_\lambda J_\lambda$. From Equation C21, thus, the diffuse radiation term $J_{d\lambda}$ is also an explicit function of the mean intensity J_λ . This indicates that the mean intensity J_λ is a self-consistency equation for J_λ itself. Then, Equation C21 becomes

$$\begin{aligned} J_\lambda(y) = & \frac{F_{e1}}{4\pi y^2} f_{e\lambda} e^{-\tau_\lambda(y)} \\ & + \frac{1}{2} \int d\mu \int \left[\varpi_\lambda J_\lambda(y', \mu) + \frac{F_{e1}}{4\pi} \Psi (1 - \varpi_\lambda) b_\lambda(T') \right] \\ & \times e^{\tau_\lambda(y', \mu) - \tau_\lambda(y, \mu)} d\tau_\lambda(y', \mu), \end{aligned} \quad (\text{C28})$$

where $\mu \equiv \cos \theta$, and $b_\lambda(T')$ is the normalized Planck function at $T' = T(y')$. F_{e1} is given by the flux ratio Ψ and the shell bottom temperature T_1 (see Equation C25). Therefore, once a spatial temperature distribution $T(y)$ and a flux ratio Ψ are given, we obtain the spatial distribution of the mean intensity $J_\lambda(y)$ at any point y in radial direction.

To close the integral equations of $J_\lambda(y)$, the DUSTY code solves the temperature profile described by

$$4\pi J_\lambda(y) = F_{e1} \left[\frac{1}{y^2} + 3\tau_{\lambda 0} \int_y^\infty q_F(y') \eta(y') \frac{dy'}{y'^2} \right], \quad (\text{C29})$$

and

$$4\pi J_\lambda(y) = 4\sigma T^4 + \frac{F_1}{y^2} \int f_{e\lambda} e^{-\tau_\lambda(y)} \left[1 - \frac{q_{a\lambda}}{q_{aP}(T)} \right] d\lambda, \quad (\text{C30})$$

where

$$q_F = \int q_\lambda f_\lambda(y) d\lambda. \quad (\text{C31})$$

Note that Equation C29 is consistent with the radiative pressure equation proposed by Auer (1984), and Equation C30 is obtained from the radiative equilibrium condition Equation C9. The flux F_λ is derived from the diffuse component $F_{d\lambda}$, however the diffuse component $F_{d\lambda}$ is derived from F_λ itself. We now assume the diffuse component as to be $F_{d\lambda} \propto B_\lambda(T)$, where $B_\lambda(T)$ is the Planck function at temperature T . Then,

$$q_F = \int q_\lambda f_{e\lambda}(y) e^{-\tau_\lambda(y)} d\lambda + q_P(T) \left(1 - \int f_{e\lambda} e^{-\tau_\lambda(y)} d\lambda \right), \quad (\text{C32})$$

where

$$q_P(T) = \int q_\lambda b_\lambda(T) d\lambda. \quad (\text{C33})$$

With Equation C29 and C30, the flux ratio Ψ becomes

$$\Psi \left(\frac{T}{T_1} \right)^4 = \frac{1}{y^2} \left[1 - \int f_{e\lambda} e^{-\tau_\lambda(y)} \left(1 - \frac{q_{a\lambda}}{q_{aP}(T)} \right) d\lambda \right] + 3\tau_{\lambda 0} \int_y^\infty q_F(y') \eta(y') \frac{dy'}{y'^2}, \quad (\text{C34})$$

when $y = 1$, then

$$\Psi = \frac{q_{ae}}{q_{aP}(T_1)} + 3\tau_{\lambda 0} \int_1^\infty q_F(y') \eta(y') \frac{dy'}{y'^2}. \quad (\text{C35})$$

We give $f_{e\lambda}$ by the spectrum which the central star emits and give η by the spatial density profile along radial direction in the dust shell. Then we obtain Ψ when a specific temperature distribution $T(y)$ is given. However the mean intensity J is needed to satisfy the shell outer boundary condition, for example $J = 0$ at $y \rightarrow \infty$ when the dust shell extends to infinity, or $4\pi J(y_{\text{out}}) = \gamma F_{e1}/y_{\text{out}}^2$, where $\gamma \sim 1.5$. This indicates that the determination of a plausible value of Ψ requires iteration through the computation. Therefore, Ψ can behave as an eigenvalue of the radiative transfer problem.

D. Light from a spotted star

The Wilson-Devinney code (WD code; Wilson & Devinney 1971) we used for examining the light curve of the dark spot model argued in the Part II solves the entire flux from a spotted star. This code is originally designed to solve problems of binary systems or triplet systems consisting of spotted stars. However specifying an extremely longer distance as the separation between the two stars and assuming a negligibly fainter companion comparing with the luminosity of the primary star, the solution can be approximately consistent with the solution of the single rotating spotted star problem. The entire flux from the stellar surface is obtained by integration of the local fluxes emitted from quadrilateral surface elements whose boundaries are consistent with meridians and latitude lines. The computational algorithm (so called ‘VFA algorithm’) to deal with the fluxes coming from the elements where are around the boundary between the spot area and the normal

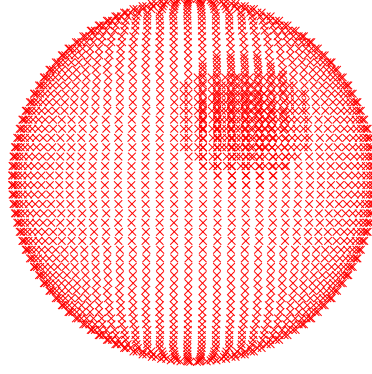


Fig. 37.— Theoretical configuration of a spotted star with spot radius of 15° . The spot centre is located in longitude of 70° .

area is developed by [Wilson \(2012\)](#). The number of surface element are specified by the number N of equivalent separations of the hemisphere along longitude direction. The length of a side along latitude direction of the element located in the longitude of θ ($0 - \pi$) is approximately $R \sin \theta$, where R is the stellar radius. The spot radius is expressed by angular radius on the stellar surface, while the spot location is specified by spherical coordinate (θ_s, ϕ_s) . Figure 37 shows the theoretical configuration of an example of a spotted star.